THE EUROPEAN
PHYSICAL JOURNAL C

Operation and performance of the MEG II detector

MEG II Collaboration

K. Afanaciev[1], A. M. Baldini[2a], S. Ban[3], V. Baranov[1], H. Benmansour[2a,2b], M. Biasotti[4a], G. Boca[5a,5b], P. W. Cattaneo[5a], G. Cavoto[6a,6b], F. Cei[2a,2b], M. Chiappini[2a,2b], G. Chiarello[7a,18], A. Corvaglia[7a], F. Cuna[7a,7b,19], G. Dal Maso[8,9], A. De Bari[5a], M. De Gerone[4a], L. Ferrari Barusso[4a,4b], M. Francesconi[10], L. Galli[2a], G. Gallucci[4a], F. Gatti[4a,4b], L. Gerritzen[3], F. Grancagnolo[7a], E. G. Grandoni[2a,2b], M. Grassi[2a], D. N. Grigoriev[11,12,13], M. Hildebrandt[8], K. Ieki[3], F. Ignatov[14], F. Ikeda[3], T. Iwamoto[3], S. Karpov[11,13], P.-R. Kettle[8], N. Khomutov[1], S. Kobayashi[3], A. Kolesnikov[1], N. Kravchuk[1], V. Krylov[1], N. Kuchinskiy[1,a], W. Kyle[15], T. Libeiro[15], V. Malyshev[1], A. Matsushita[3], M. Meucci[6a,6b], S. Mihara[16], W. Molzon[15], Toshinori Mori[3], F. Morsani[2a], M. Nakao[3], D. Nicolò[2a,2b], H. Nishiguchi[16], A. Ochi[17], S. Ogawa[3], R. Onda[3], W. Ootani[3], A. Oya[3], D. Palo[15], M. Panareo[7a,7b], A. Papa[2a,2b,8], V. Pettinacci[6a], A. Popov[11,13], F. Raffaelli[2a], F. Renga[6a], S. Ritt[8], M. Rossella[5a], A. Rozhdestvensky[1], P. Schwendimann[8], K. Shimada[3], G. Signorelli[2a], A. Stoykov[8], M. Takahashi[17], G. F. Tassielli[7a,7b,20], K. Toyoda[3], Y. Uchiyama[3,17], M. Usami[3], A. Venturini[2a,2b], B. Vitali[2a,6b], C. Voena[6a,6b], K. Yamamoto[3], K. Yanai[3], T. Yonemoto[3], K. Yoshida[3], Yu. V. Yudin[11,13]

[1] Joint Institute for Nuclear Research, 141980 Dubna, Russia
[2] (a)INFN Sezione di Pisa, Pisa, Italy; (b)Dipartimento di Fisica dell'Università, Largo B. Pontecorvo 3, 56127 Pisa, Italy
[3] ICEPP, The University of Tokyo, 7-3-1 Hongo, Bunkyo-ku, Tokyo 113-0033, Japan
[4] (a)INFN Sezione di Genova, Genoa, Italy; (b)Dipartimento di Fisica dell'Università, Via Dodecaneso 33, 16146 Genoa, Italy
[5] (a)INFN Sezione di Pavia, Pavia, Italy; (b)Dipartimento di Fisica dell'Università, Via Bassi 6, 27100 Pavia, Italy
[6] (a)INFN Sezione di Roma, Rome, Italy; (b)Dipartimento di Fisica dell'Università "Sapienza", Piazzale A. Moro, 00185 Rome, Italy
[7] (a)INFN Sezione di Lecce, Lecce, Italy; (b)Dipartimento di Matematica e Fisica dell'Università del Salento, Via per Arnesano, 73100 Lecce, Italy
[8] Paul Scherrer Institut PSI, 5232 Villigen, Switzerland
[9] Institute for Particle Physics and Astrophysics, ETH Zürich, Otto-Stern-Weg 5, 8093 Zurich, Switzerland
[10] INFN Sezione di Napoli, Via Cintia, 80126 Naples, Italy
[11] Budker Institute of Nuclear Physics of Siberian Branch of Russian Academy of Sciences, 630090 Novosibirsk, Russia
[12] Novosibirsk State Technical University, 630092 Novosibirsk, Russia
[13] Novosibirsk State University, 630090 Novosibirsk, Russia
[14] Oliver Lodge Laboratory, University of Liverpool, Liverpool L69 7ZE, UK
[15] University of California, Irvine, CA 92697, USA
[16] KEK, High Energy Accelerator Research Organization, 1-1 Oho, Tsukuba, Ibaraki 305-0801, Japan
[17] Kobe University, 1-1 Rokkodai-cho, Nada-ku, Kobe, Hyogo 657-8501, Japan
[18] Present address: Department of Engineering, University of Palermo, Viale delle Scienze, Building 9, 90128 Palermo, Italy
[19] Present address: INFN Sezione di Bari, Via Giovanni Amendola, 173, 70126 Bari, Italy
[20] Present address: Dipartimento di Medicina e Chirurgia, Università LUM "Giuseppe Degennaro", 70010 Casamassima, Bari, Italy

V. Baranov: Deceased

[a] e-mail: paolo.cattaneo@pv.infn.it (corresponding author)

Abstract The MEG II experiment, located at the Paul Scherrer Institut (PSI) in Switzerland, is the successor to the MEG experiment, which completed data taking in 2013. MEG II started fully operational data taking in 2021, with the goal of improving the sensitivity of the $\mu^+ \rightarrow e^+\gamma$ decay down to $\sim 6 \times 10^{-14}$ almost an order of magnitude better than the current limit. In this paper, we describe the operation and performance of the experiment and give a new estimate of its sensitivity versus data acquisition time.

Contents

Springer

1 Introduction

The MEG II detector is the upgrade, with significant improvements and additions, to the MEG detector [1], which by 2013 had recorded data establishing the best limit to date for the SM violating decay $\mu^+ \to e^+\gamma$ [2]. The goal of the upgraded experiment is to improve the sensitivity of this decay by about one order of magnitude. The physical rationale for this upgrade and the design criteria for the MEG II subdetectors are outlined in [3].

The signal is a γ-ray and a positron back-to-back with energy $E_\gamma \sim E_{e^+} \sim m_\mu c^2/2 = 52.83$ MeV emanating at the same time from a common vertex. The main background results from the accidental time coincidence of high-momentum positrons from Michel decay $\mu^+ \to e^+\nu\bar{\nu}$ and high-energy γ-rays from radiative muon decay (RMD) $\mu^+ \to e^+\nu\bar{\nu}\gamma$, positron Bremsstrahlung and positron annihilation in flight $e^+e^- \to \gamma\gamma$. An additional smaller background is RMDs with high-momentum positrons and high-energy γ-rays.

A schematic view of the detector highlighting the main components can be found in Fig. 1. The detector is located at the πE5 beamline in the high-intensity proton accelerator facility at the Paul Scherrer Institut (PSI) in Switzerland, allowing the world's most intense continuous positive muon beam to be stopped in a thin target and to measure the decay products. The positron spectrometer relies on the COnstant Bending RAdius (COBRA) superconducting magnet generating a gradient magnetic field ranging from 1.27 T in the centre to 0.50 T at either end of the magnet cryostat to measure positron momenta by the Cylindrical Drift CHamber (CDCH). Positron time is measured by the pixelated Timing Counter (pTC), and the Radiative Decay Counter (RDC) helps reject background. Finally, the Liquid Xenon (LXe) detector uses on the scintillation process to measure the energy, position and timing of the incident γ-ray.

We use a cylindrical coordinate system (r, ϕ, z) with the origin at the centre of COBRA. The z-axis is aligned along
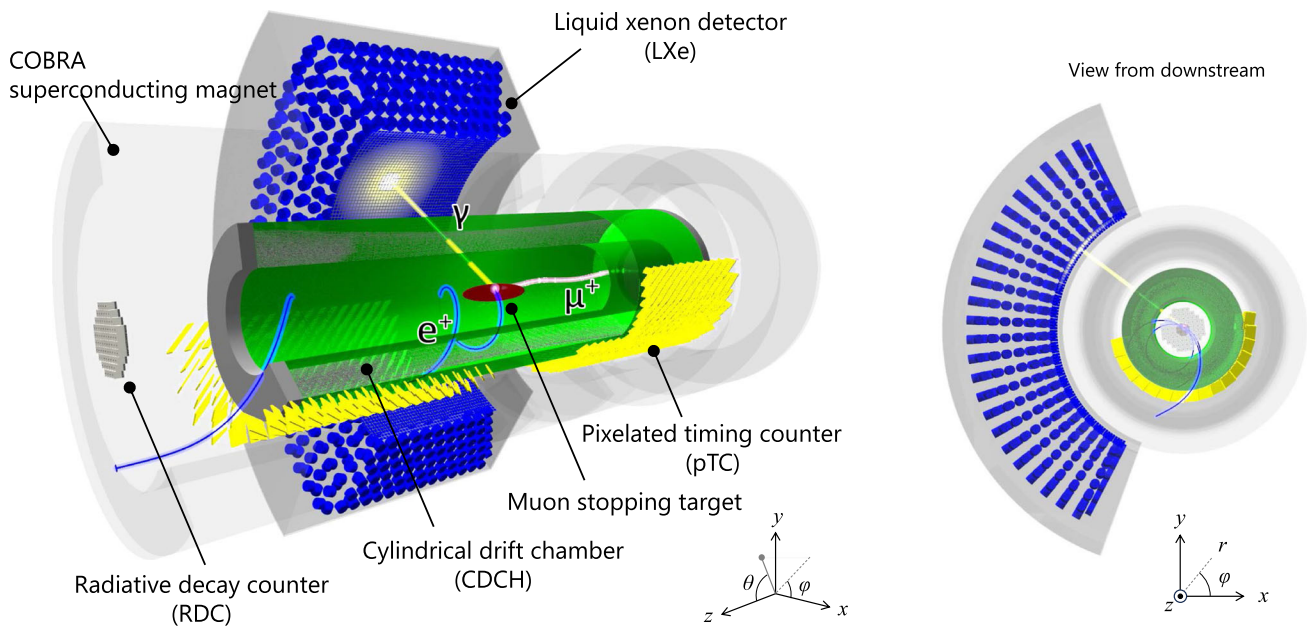
Fig. 1 A sketch of the MEG II detector with a simulated $\mu^+ \rightarrow e^+\gamma$ event

the COBRA axis in the direction of the incident muon beam. The azimuthal angle $\phi = 0$ is opposite the centre of the LXe detector, and corresponds to the x-axis of the associated Cartesian coordinate system, while the y-axis points upward. Positrons follow trajectories with decreasing ϕ coordinate. The polar angle θ with respect to the z-axis is also used. The region with $z < 0$ is called upstream, while the region with $z > 0$ is called downstream.

The geometrical acceptance of the experiment is defined by the size of the LXe fiducial volume, which is approximately equal to $\phi_\gamma \in \left(\frac{2}{3}\pi, \frac{4}{3}\pi\right)$ and $|\cos\theta_\gamma| < 0.35$, giving an overall acceptance of $\sim 11\%$. The efficiencies given below refer to this geometrical acceptance.

After the years 2017 to 2020 during which the engineering runs required to commission the detector component were performed, data acquisition with the detector fully operational began in 2021 with the $\mu^+ \rightarrow e^+\gamma$ trigger activated.

In this paper, we give only a brief summary of the designs of the subdetectors, describing only the differences between the design and the actual realisation, and we describe the operation and performance of the detector and compare the measured resolutions with the design [3]. Finally, the expected sensitivity for the coming years is presented.

2 Beam

Pions and muons are produced by impinging protons, accelerated up to 590 MeV by the PSI ring cyclotron, onto the production target TgE at an angle of 8° with respect to the beam direction. This configuration, in operation since the second half of 2020, has proved to be less sensitive to variation of the secondary beam intensities as a function of the proton beam position. For a comprehensive and historical description of the PSI facility, see [4,5].

The πE5 area is served by a low-energy secondary beamline capable of delivering pions and muons in the 10 to 120 MeV/c momentum range. It has a 165° angle of view with respect to the proton beam on TgE. Figure 2 shows the beamline layout from TgE up the MEG II detector. The AHSW41 dipole, which is part of the proton beamline, captures the pions and muons in the backward direction and defines the momentum accepted by the πE5 beamline. The collected charged particles are deflected by 47.5° and coupled into a straight section consisting of quadrupoles (QSF4*) and sextupoles (HSC4*). Along this section three slit systems (FS41–42–43) are used to reduce the beam intensity delivered to the experimental area and (FS41–43) to cut the momentum distribution. This is possible because the dipoles introduce dispersion into the lattice and because the beams are not monochromatic and there is a correlation between the horizontal transverse coordinate of the beam and the momentum distribution.

In the MEG II experiment, where surface μ^+ (28 MeV/c) are selected and stopped in the muon stopping target (see Sect. 3), FS41 is used to reduce the beam intensity which also reduces the width of the momentum distribution and results in less straggling at the target and a higher stopping efficiency.

After QSF48, the dipole magnet AST41 produces a symmetric deflection of the beam, again at 47.5°, to either the Z-channel or the U-channel. When the Z-channel mode is
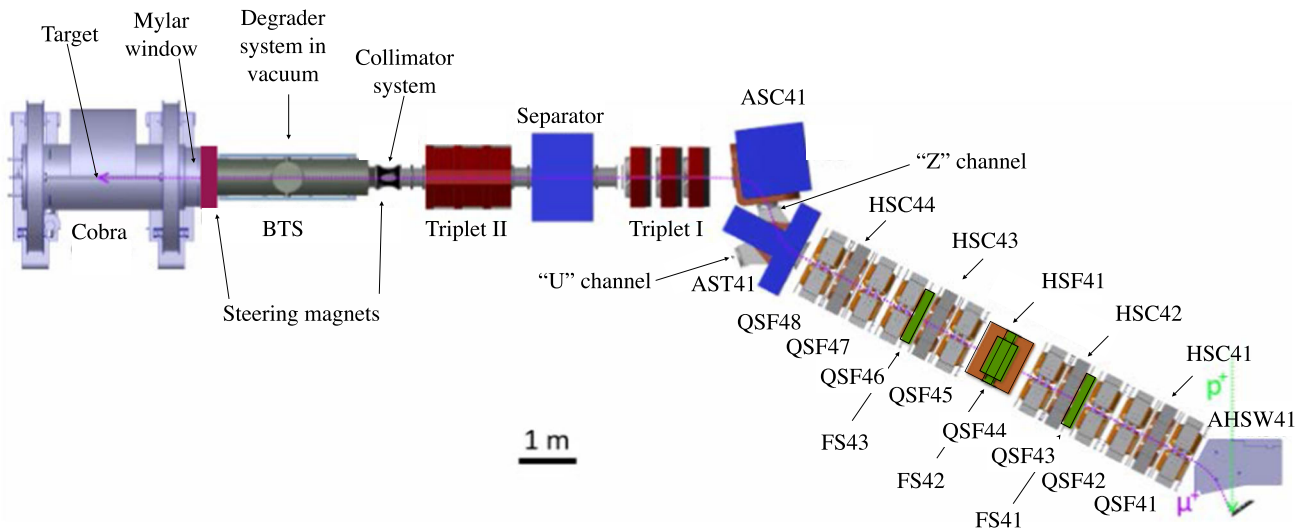
Fig. 2 πE5 beamline section connected to Z-channel. The elements up to Triplet II are shared between the MEG II and the Mu3e [6] experiments

selected, the beam is transmitted through a second dipole ASC41, which generates a 75° deflection and then delivers the beam into the experimental area.

The beam is coupled into a Wien filter via Triplet I, a quadrupole triplet, to separate the muon beam from the main contaminants: pions and positrons. The separation is achieved vertically at the downstream collimator system. The task of Triplet I is to shape the beam so that it has a horizontal waist, while being vertically parallel to enhance the separation.

The beam is then focused by Triplet II at a collimator, dumping the contaminating beams. For beam tuning campaigns in πE5, the first measurement point is immediately downstream of the collimator.

Triplet II couples the beam into the Beam Transport Solenoid (BTS). There, a 300 μm thick Mylar® moderator is positioned at the focus to minimise the effects of multiple scattering. A 190 μm thick Mylar window separates the vacuum in the beamline from the helium atmospheric volume containing the muon-stopping target at the centre of the COBRA magnet.

The field shape of the COBRA magnet was optimised to reduce the dependence of the bending radius on the emission angle of charged particles coming from the centre of the experiment and to avoid multiple turn trajectories through the tracking system, which severely affected the MEGA experiment [7]. A detailed description of the final part of the beamline, the BTS, COBRA and the magnetic field map, its calculation and measurement, can be found in [1].

Beam tuning at different intensities was performed to meet different requirements, including specific calibration data sets at low beam intensity (down to 10^6 particles/s). Figure 3 shows a typical beam profile measured at the centre of the COBRA magnet, where the stopping target is
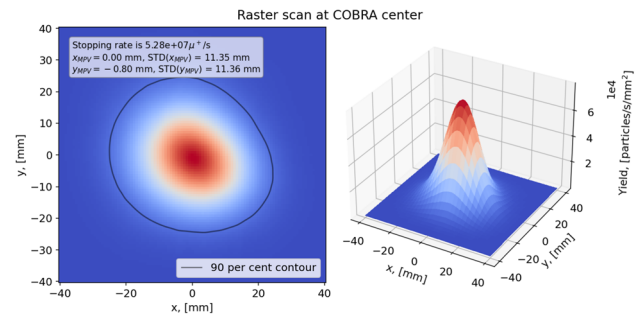
Fig. 3 Beam profile at COBRA centre for a stopped muon rate $R_\mu = 5.3 \times 10^7 \, \text{s}^{-1}$ at $I_p = 2.2 \, \text{mA}$

located. The beam is centred at $x_b = (0.0 \pm 0.5)$ mm, $y_b = (-0.8 \pm 0.5)$ mm with a standard deviation of the two coordinates equal to $\sigma_x = (11.35 \pm 0.50)$ mm and $\sigma_y = (11.36 \pm 0.50)$ mm. In this figure, the slits were tuned to obtain a stopped muon rate $R_\mu = 5.3 \times 10^7 \, \text{s}^{-1}$ at the primary proton beam current $I_p = 2.2 \, \text{mA}$.[1] Beam settings with similar profiles were achieved in the range of stopped muon rates $R_\mu = (2 - 5) \times 10^7 \, \text{s}^{-1}$.

During the 2021–2022 physics runs, different R_μ were used, starting with a lower value, to study the detector stability and rate capability, to tune the data acquisition and trigger systems, and to optimise the reconstruction algorithms, as explained in the next sections. Table 1 summarises the used R_μ, normalised to the typical I_p for each year. The listed numbers include the MEG II target-stopping efficiency estimated by simulation to be 89%. A 5% systematic uncertainty is attached to each measurement of R_μ, due to uncertainties

---

[1] This is the nominal value of the facility. In 2021–2022, the actual current was lower; see Table 1.

on the beam measurement setup and variations of the proton beam position on TgE.

The measurement reported here has been performed using an avalanche photodiode detector (SPL4419 Hamamatsu). It has a 1.5 mm active area radius, with 130 μm depletion layer. The depletion layer is the sensitive part of the detector, allowing for a clear separation between the energy deposit by the muons (stopping particles) and positrons (minimum ionising particles) mainly from stopped muon decay. A scan on the plane perpendicular to the incident beam direction is performed in steps of 2 mm. Details about the beam monitoring detectors used and developed for the MEG II experiment can be found in [3].
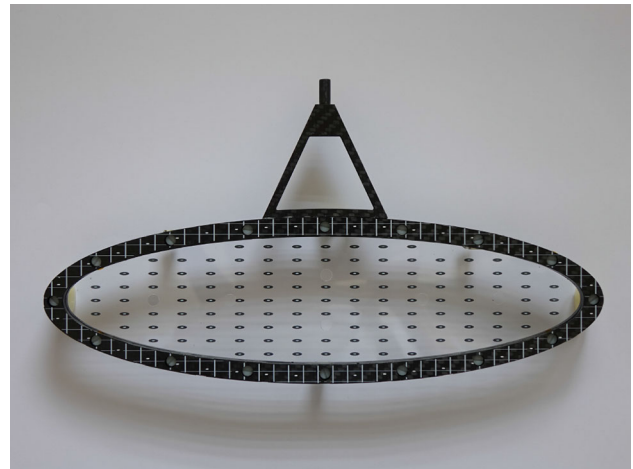
3 Target

The role of the target is to stop the μ^+ beam over a limited axial region at the centre of the COBRA magnet satisfying a number of contradictory requirements. The target must intercept the largest possible fraction of the beam, yet with a minimal amount of material to reduce the interaction of particles from muon decay. The target parameters are the results of extensive calculations and simulations as well as of the experience gained in MEG. Most relevant, the position and planarity of the target must be precisely known to limit the systematic errors in μ^+ decay vertex position.

3.1 Concept and design

The design of the MEG II target has been optimised, on the basis of measurements and simulations. Different combinations of material/target thickness/degrader thickness have been considered [8]. A scintillator material (BC400) was selected for the target, which has the advantage, over non-scintillating materials, to allow non-destructive beam intensity and profile measurements with dedicated equipment. After some experimental investigation, the current effort is to exploit the feasibility of this technique within the strict constraints dictated by the MEG II experiment.

In order to identify a $\mu^+ \rightarrow e^+\gamma$ event, it is necessary to measure the angles of the e^+ trajectory (ϕ_{e+}, θ_{e+}) at the point where the μ^+ decays by back-propagating the trajectory measured by the spectrometer up to the target surface. The MEG II spectrometer provides a precision of $\sim$ 7 mrad. A precise knowledge of the target position is then required: with a radius of curvature $\sim$ 13 cm for the e^+ trajectory in $\mu^+ \rightarrow e^+\gamma$ events, a displacement of the target by 500 μm along its normal direction implies a systematic deviation of $\sim$ 4 mrad in ϕ_{e+} for $\phi_{e+} = 0$, and a larger effect for non-zero ϕ_{e+}.

Moreover, deformations of the target planarity, which were observed during the MEG data taking, produce a similar

Fig. 4 The MEG II target with the dot pattern on the foil and on the frame. The six holes are located along the ellipse axes

effect. The uncertainty on the target position and deformation was the dominant systematic error in the MEG result [2], causing a 5% variation of the upper limit on the branching ratio while other contributions were below 1%.

3.2 The target mechanics

The MEG II target is an elliptical foil (length of 270 mm and height of 66 mm) with (174 ± 20) μm average thickness (the error is the maximum deviation not the Gaussian σ). The direction normal to the target foil lies on the horizontal plane (x, z) and forms an angle of $(75.0 \pm 0.1)°$ with respect to the beam axis (z-axis). The nominal position and the error (maximum not Gaussian) are evaluated on the basis of the mounting procedure and fixation to the adaptation mechanism, but are not used in the analysis. The target inclination as well as its position are estimated with the methods described in the following.

The target foil is supported by two hollow carbon fibre frames. A pattern of white dots, superimposed on a black background, is printed on both the frame and the foil. The dots are elliptical with a height and a width of 0.51 mm and 1.52 mm on the target and 0.42 mm and 1.27 mm on the frame such that the dots appear circular when imaged at an oblique angle with respect to the target's surface. Six holes are bored into the target, that are (barely) visible along the ellipse axis on Fig. 4: four along the major axis, two along the minor one located symmetrically with respect to the centre. Starting from the dot at the center, they are located at the place of the (missing) third dots along the short axis, at the place of the (missing) seventh points and between the fourth and fifth dots along the long axis.

The holes and the dots are instrumental in measuring the relative alignment between the target and the tracking detectors as discussed in Sect. 4.5.2.

Table 1 Stopped muon rates R_μ for the runs 2021–2022 normalised to the typical I_p for each year

Year	Typical I_p (mA)	R_μ (10^7 s^{-1})		
2021	1.965	3.12	4.01	5.21
2022	1.765	2.80	4.07	5.02

3.3 The photo camera system for position measurement

The target position at the beginning of a MEG II data-taking run is precisely determined, with improved accuracy with respect to MEG, thanks to reflectors installed on the target frame for a optical survey using a laser.

Target position monitoring over long data taking periods was also possible by reconstructing the position of several fiducial holes made in the target itself. A map of the reconstructed muon decay vertices on the target clearly showed the position of such holes. If the target position assumed in the trajectory reconstruction procedure is not exact, the holes artificially appear at different positions for different e^+ angles. This method allowed one to reconstruct deviations of the target position from the nominal one. It was also effective to identify and correct the deformation of the target planarity. On the other hand, it required a large amount of data, so that it could only be used to monitor the average target position over a few months of data taking, while the target was frequently moved far from its working position (at least every week) to perform the calibration of the LXe detector through a pneumatic system, which did not ensure micrometric repeatability or reproducibility of the target positioning.

The improved resolutions of the MEG II positron spectrometer imposed the development of an additional method for more frequent monitoring of the target relative position over the data taking period to ensure that the systematic errors due to target position and deformation remain limited. The method is based on a photogrammetric survey of a pattern of dots printed on the target itself.

The dots are imaged with two digital CMOS photo cameras placed outside the beam halo, hosted in two independent supports. Two LEDs are placed on one of these support to provide illumination during the acquisition of the target pictures. The supports are fixed to the target insertion system at a distance of ∼ 1000 mm from the centre of the MEG II reference system, in correspondence to the CDCH (see Sect. 4) endplate. The transverse distance from the z-axis is ∼ 120 mm, at $\theta = 6.3°$.

One camera (IDS, mod. UI-3282SE)[2] has a Sony IMX264 sensor having 2456×2054 pixels each of $3.5\,\mu$m size, for a total sensor size of (8.473×7.086) mm^2 and a TUSS optical system, mod. LVK7518, with a focal length of 75 mm and a maximum aperture of $f/1.8$. The USB3 protocol is used for communications with front-end computers, since it has been proven to be immune to the magnetic field [9].

The second camera (RVT-1001700S)[3] is a radiation tolerant camera from Spectral Instruments equipped with 4×10^6 pixels each of $5.5\,\mu$m size, and a 50 mm lens. This camera connects directly to a server communicating via fibre optic [10].

3.4 The photogrammetric method

The photogrammetric method is based on frequent and regular measurements (pictures) taken during the run. The photo cameras image the pattern of dots, and the position of dots on the picture can be determined with standard image processing algorithms. If the target moves between two successive camera shoots, or if it deforms over time, the position of these patterns in the pictures will change. The displacement of the target can be then determined with respect to a reference position, measured at the time of the optical survey.

Two approaches are used to determine the target position, orientation and deformation, starting from the different sets of pictures taken from the two photo cameras. The target position and orientation are described by the coordinates of the target centre in the MEG II reference system and by the Euler angles, respectively. The deformation is taken into account differently by the two approaches.

In the first approach, a χ^2 goodness of fit is performed, in which the χ^2 is computed from the measured and the expected dot positions, where the latter depend on the target position and deformation and on the parameters of the optical system. The deformation is parameterised with Zernike polynomials; target position and deformation are floating parameters in the fit, while the parameters of the optical system are measured from pictures taken just after the optical survey, when the target parameters are known. There are seven optical parameters: the position of the optical centre (three parameters), the independent components of the unit vector of the optical axis (two parameters), the orientation of the sensor around the optical axis (one parameter), and the distance of the sensor from the centre of the optical system (one parameter).

The method has been validated on a bench-top test, by installing the photo camera, a LED, and a target mock-up on an optical table in a configuration similar to that in the exper-

---

[2] http://www.1stvision.com/cameras/models/IDS-Imaging/UI-3282SE-M/C.

[3] http://specinstcameras.com/wp-content/uploads/2021/07/RVT100-Brochure.pdf.
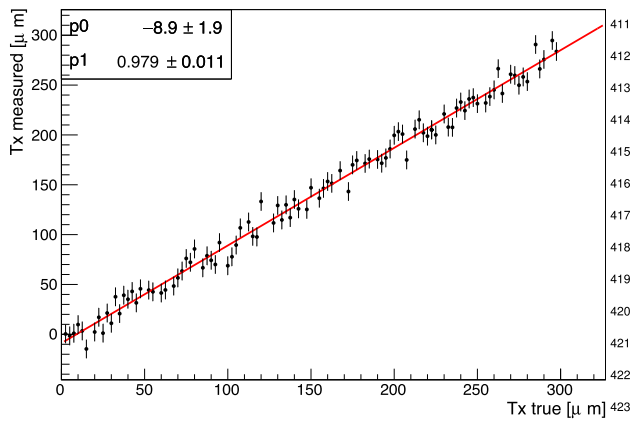
Fig. 5 Difference between the measured shift of the x-coordinate of the target centre obtained with the photogrammetric method as a function of the true shift, for a position scan in the x-direction

Fig. 6 2D residuals at the camera image plane scaled to the object plane assuming the 3D CT-scan shape. The axes are the dot indices

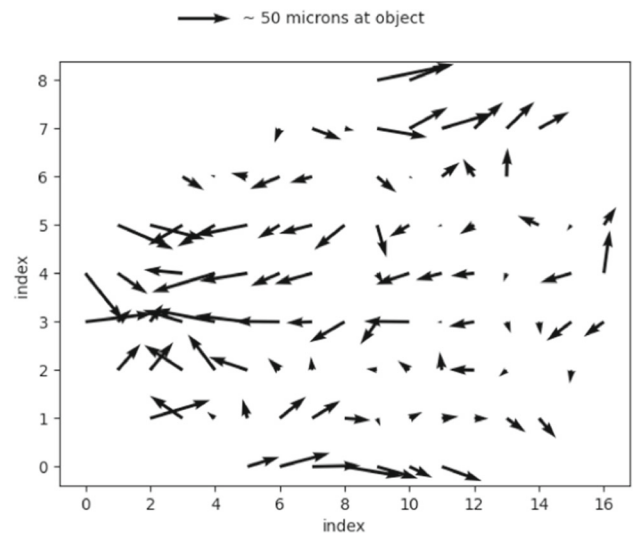iment. The target was mounted on a linear stage with 2.5 μm position accuracy. Figure 5 shows the difference between the measured shift in the x-coordinate of the target centre, obtained with the photogrammetric method, as a function of the true shift, for a position scan performed along the x-direction (normal to the target plane). A linear fit has been performed to the distribution. The resulting uncertainty in the x-coordinate of the target centre T_x is $\sigma_{T_x} = 12$ μm. Given that the direction transverse to the target plane in the experiment is almost coincident with the x-axis, we can conclude that we fully satisfy the precision requirements < 500 μm. The angular coefficient p1 is consistent with 1 and the difference of the intercept p0 with 0 is negligible compared with the required precision.

The second approach minimises a χ^2 at the camera's image plane between the measured, imaged dot coordinates $\left(X'_{\text{CCD}}, Y'_{\text{CCD}}\right)$ and estimated 3D dot coordinates in the camera coordinate system $\left(\vec{X}_{\text{CAM}}\right)$ for each image. Here, $X_{\text{CAM}}, Y_{\text{CAM}}$ are parallel with the camera's CCD and Z_{CAM} is parallel with the camera's optical axis. Images are taken every ∼ 10 min to track the position, orientation, and shape of the target in the camera coordinate system. The analysis relies on a single position and orientation of the target with respect to the CDCH to map the coordinates in the camera coordinate system to the standard MEG II coordinate system. This is taken either from an optical survey or the hole analysis. Here, the relative 3D dot coordinates in a local target coordinate system were taken from a CT-scan of the target. This CT-scan contains $O(10\,\text{M})$ data points including the 3D target deformation (< 1 mm). Given the measured distances between the dots on the foil and the camera's optical focal length, the technique is self-calibrating.

We rely on the following optical equations to project the 3D coordinates in the camera coordinate system onto the image plane where f is the camera's focal length :

$$X_{\text{CCD}} = \frac{X_{\text{CAM}} \cdot f}{Z_{\text{CAM}} - f}, \quad Y_{\text{CCD}} = \frac{Y_{\text{CAM}} \cdot f}{Z_{\text{CAM}} - f}. \tag{1}$$

The χ^2 contains a rigid body transformation $R\left(\vec{X}_{\text{T}}, \vec{\theta}_{\text{T}}\right)$ with a translation and three Euler angles:

$$\chi^2 = \sum_i^N \left[R\left(\vec{X}_{\text{T}}, \vec{\theta}_{\text{T}}\right) \cdot X_{i,\text{CCD}} - X'_{i,\text{CCD}} \right]^2$$
$$+ \left[R\left(\vec{X}_{\text{T}}, \vec{\theta}_{\text{T}}\right) \cdot Y_{i,\text{CCD}} - Y'_{i,\text{CCD}} \right]^2. \tag{2}$$

The residuals dot-by-dot at the image plane scaled to the object are shown in Fig. 6. Without any additional shape parameters, the fit results in residuals < 50 μm at the object. These are due to additional deformations between the time of the CT-scan and that of the image, errors in the measured dot coordinates on the image plane, and errors in the projection equations. The residuals can be further suppressed by including elliptical Bessel function parameters (i.e. "drumhead modes") into the fit, but the rigid body transformation was sufficient for the full 2021 data set given the 3D CT-scan.

The two methods have been compared on pictures taken during the 2021 run, and found to yield consistent results within 100 μm in the direction normal to the target plane, which is the most sensitive to the angular resolutions.

3.5 The target hole method

The hole analysis is performed after correcting the temporal variation of the target position traced by the photogrammetric

method to determine the target position relative to the CDCH. The method and the results are described in Sect. 4.5.3.

4 Cylindrical drift chamber

The positron momentum and position vectors are measured with CDCH. In this section we review the main advantages of CDCH over the MEG drift chamber system, its construction, commissioning, reconstruction, alignment and performance.
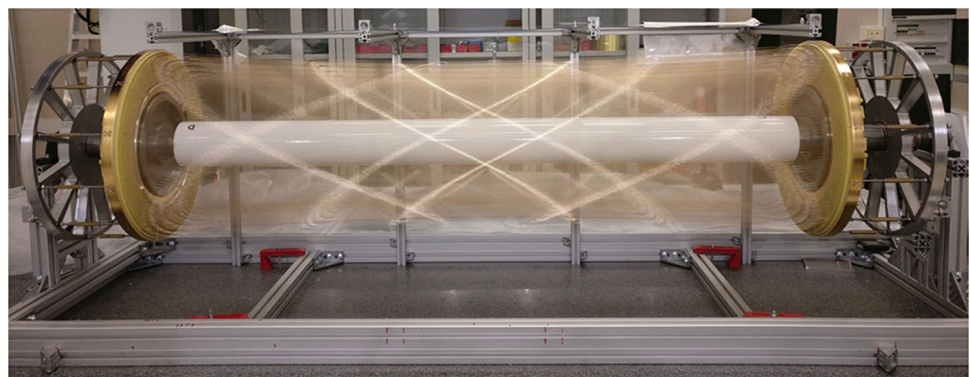
4.1 Concept and design

The MEG drift chamber system consisted of sixteen individual radially aligned chambers. With this detector configuration, relevant efficiency loss and resolution degradation were caused by the material of the chamber's mechanical support, electronic cards and cables, which were frequently crossed by the positron trajectories. The CDCH, extensively discussed in [3,11], overcomes these limitations by replacing the segmented structure of the MEG chambers with a single volume one.

The CDCH, shown in Fig. 7, is a 1.93 m long low-mass cylindrical volume, filled with a helium–isobutane gas mixture (the exact composition is specified in Sect. 4.3) and equipped with nine concentric layers of 192 gold-plated tungsten sense wires each, 1728 in total, arranged in a stereo configuration with two views and $\sim$ 10 000 silver-plated aluminium cathode and guard wires. The sense wires collect the signals from the drift electrons, while the cathode and guard wires form nearly square drift cells and define the electric field within and at the boundaries of the sensitive volume; the cell dimensions range from 5.8 mm to 7.5 mm at center and from 6.7 mm to 8.7 mm at the end-plates. The sense wires within the experimental acceptance, about 1200, are read out by the data acquisition system.

A zoom on the endplate region to magnify the wire stereo geometry is shown in Fig. 8.

Fig. 8 Zoom on the stereo wire geometry, radial perspective

4.2 Construction

Construction of the CDCH, which began in late 2016 and was completed in spring 2018, was performed modularly by soldering wires in groups of sixteen onto printed circuit boards (PCBs), which were then mounted between radial spokes at the ends of the chamber. The mechanical structure of the detector achieves its final form by integrating a carbon fibre component securely fastened to both end-plates, effectively enclosing the sensitive volume.

The chamber was delivered to PSI for the commissioning phase in summer 2018 and integrated into the MEG II detector in winter 2018. After installation, the CDCH was operated at PSI with engineering runs in 2019 and 2020 and with physics data taking runs in 2021 and 2022.

4.2.1 DAQ and services

High voltage (HV) is supplied with a commercial system by ISEG Spezialelektronik GmbH, made of mod. EHS F230 and EHS F430 boards in a WIENER crate with MPOD controller, for a total of 144 channels. HV channels are split between two cables by custom-built distribution boards, and eight wires are powered through each cable.

Ionisation signals are read at both ends of the chamber wires by 216 front-end (FE) boards with a bandwidth of $\sim$ 400 MHz, which are connected to the wire PCBs. The signals are digitised at 1.2 GSPS by the WaveDREAM boards of the integrated trigger and DAQ system WaveDAQ, described in Sect. 8. The low voltage (LV, 5 V) is supplied to the FE

Fig. 7 Picture of the open CDCH equipped with all the wires

boards via a dedicated distribution system through the Wave-DREAM boards. As the FE boards have a total power consumption of ≈ 350 W, they have to be cooled with water and glycol by a cooling system built into the board holders and purged with dry air to avoid condensation of water vapour.

The gas is supplied by a dedicated gas system [12] that mixes helium with isobutane and oxygen in the required proportions. Isopropyl alcohol is added by passing a fraction of the helium flow through a thermostated, alcohol-filled bubbler.

4.3 Final geometry and operation

The final geometry of the CDCH differs in some details from the original design. The chamber was designed to have ten layers of sense wires, but during the wiring phase there were delays in establishing the environmental conditions and procedures needed to eliminate the risk of wire breakage. Then, the outermost layer was not installed to fit into the schedule of the CDCH operation. We used Monte Carlo (MC) simulations to verify that the degradation of tracking efficiency and performance due to the missing layer is $< 1\%$.

First, using Garfield++ simulations [13], the HV operating point was set in the range 1400 to 1480 V, with the innermost layer at the highest voltage, to achieve a gas gain of $\sim 5 \times 10^5$. This configuration gives a reasonable sensitivity to individual ionisation clusters, as confirmed by the distance of closest approach (DOCA) measurements presented in Sect. 4.4. The HV can be set individually for each cell at 10 V steps to account for difference in size of cell due to their radial position within the chamber. The mechanical tension of the wires, which is required to ensure electrostatic stability and to avoid short circuits between the anode and cathode wires, was also calculated using Garfield++ simulations. Several tests were carried out, both on a full-size prototype and on the CDCH itself. The required tension value was determined by stretching the wires by $+5.2$ mm with respect to the nominal length (65% of the elastic limit), based on calculations.

The gas mixture was also optimised in 2019 and 2020 to avoid corona discharges and current spikes and to restore normal operation after a sustained short circuit between an anode and a cathode wire. The original He–isobutane gas mixture (90 : 10) was modified by the addition of oxygen and isopropyl alcohol (1.5%). The addition of oxygen is a particularly delicate operation due to its electronegativity, as it can capture drift electrons. The oxygen level was initially set to 2% to dampen anomalous currents of ~ 400 μA and then gradually reduced to a stable value of 0.5% after normal current levels were restored.

In Fig. 9 we show typical currents on six HV channels during normal MEG II beam operation; each HV channel powers 16 sense wires.
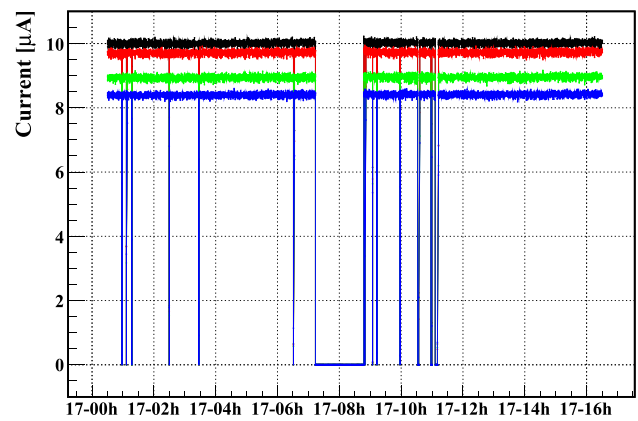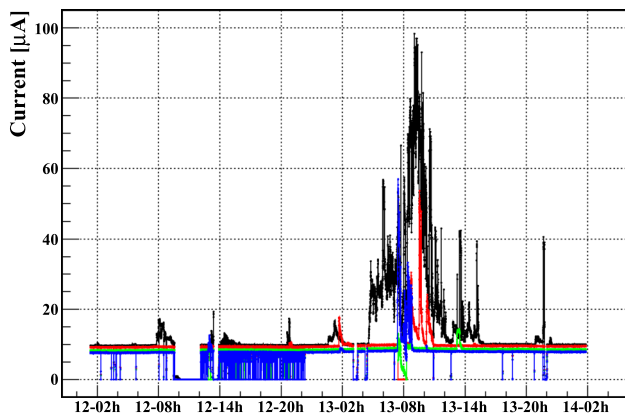

Fig. 9 Typical currents drawn by six CDCH HV channels when the μ^+ beam is on. Currents fall abruptly to zero when the beam goes off

4.3.1 Issues and problems

The main problem encountered during the construction and commissioning of CDCH was the breakage of 107 cathode wires. The wire breaks were investigated in detail by microscopic inspections, chromatography, SEM/EDX analyses and immersion tests in water, and were proved to be due to galvanic corrosion of the aluminium core, caused by air humidity penetrating through small cracks in the silver coating. A phenomenological model [14] was developed to predict the number of breaks as a function of the time the wire is exposed to the ambient moisture and the elongation of the wire. The problem was solved by keeping the CDCH in a controlled dry atmosphere during maintenance and operation. When these precautions were taken, the rate of wire breakage dropped to 0 so far.

The impact of ~ 100 missing cathodes ($< 1\%$ of the total) was assessed by using MC simulations and found to be negligible. Nevertheless, the presence of broken wire fragments within the CDCH is dangerous as they can cause short circuits affecting several sectors of the chamber. All fragments were carefully removed with a dedicated tool, but one of them caused the strong short circuit cited in Sect. 4.3, which increased the chamber current up to ~ 400 μA. A dedicated optimisation procedure for the gas mixture was necessary to restore normal current values.

During the standard data taking it is very important to keep the isopropyl alcohol level stable, to avoid current spikes, by continuously bubbling it within the chamber; an example of the current spikes occurring in case of a shortage of isopropyl alcohol is shown in Fig. 10. An additional problem is the noise caused by occasional short circuits on FE boards. Because the FE boards are densely mounted on the back of the chamber end plates, small movements of a board can cause short circuits between the capacitors on the board and the aluminium support structure of the board itself; such

Fig. 10 Currents in four sectors of layer 1. Spikes are due to shortage of isopropyl alcohol

Fig. 11 Example of typical waveforms in a drift cell crossed by a e^+ track after the noise reduction applied. The top plot is read by the upstream electronics, the bottom by the downstream

short circuits cause oscillations in the amplifier circuits that can affect the behaviour of large parts of the chamber. These oscillations can only be stopped by switching off the LV of the boards, but since the LV is distributed in groups of eight channels, a single noisy channel will cause eight channels to fail. This problem was solved by inserting suitable insulating plastic blocks to ensure the proper separation between the board elements and the metallic parts of the support structure.

### 4.4 Reconstruction algorithms

The purpose of the CDCH analysis is to identify and reconstruct the positron tracks using the information on the sense wires provided by the ionisation clusters. The CDCH operates in a high-rate environment; the hit rate per cell can be > 1 MHz at the innermost wires for $R_\mu = 5 \times 10^7\,\mathrm{s}^{-1}$, corresponding to a cell occupancy of 25% in the time window of maximum drift time. Moreover, the geometrical characteristics, with only nine layers and small stereo angles, makes the track finding complicated.

A more detailed description on the reconstruction algorithms is available elsewhere [15].

4.4.1 Waveform processing and hit reconstruction

The first step is to identify the signals induced by drift electrons in the waveforms of the cells traversed by positrons; such signals are called "hits". Figure 11 shows typical waveforms due to a hit, which consists of several temporally separated pulses from different ionisation clusters that are stretched by the slow drift time of the electrons. For good hit reconstruction efficient signal-to-noise discrimination and pile-up identification are required. Two waveform processing algorithms have been developed to detect hits.

A coherent low frequency noise was observed mainly over adjacent 16 wires. Therefore, the first algorithm starts with
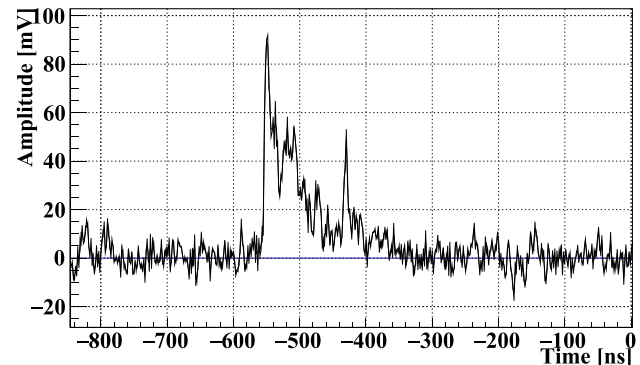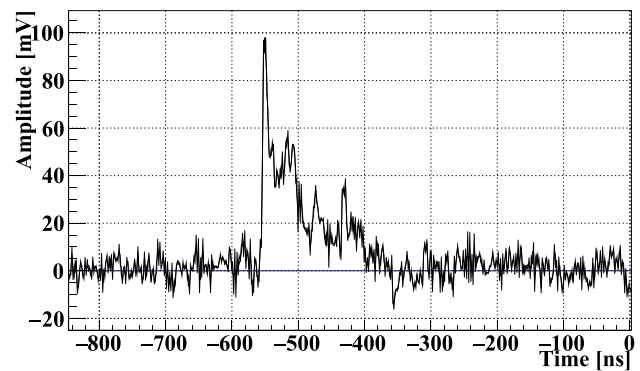
coherent noise subtraction using the averaged waveform for adjacent channels excluding the region with signal pulses. This reduces the noise level (FWHM) from 23 mV at 13 mV. Significant incoherent high frequency noise is observed for > 200 MHz, while the signal power in this frequency range is negligible. Therefore, we apply high-frequency cut-off at 225 MHz using a discrete Fourier transform technique. These noise reduction algorithms have been optimised by maximising the number of hits per track and the tracking efficiency, and minimising the chi-square of track fitting.

Hit detection is based on a fixed voltage threshold for two adjacent sampling points and a fixed threshold for the integration over 20 ns from the two initial points. After the hit is detected, the thresholds are lowered to look for a low-amplitude cluster pulse before the detected pulse.

The second method uses a deep-learning algorithm based on a convolutional neural network (CNN). The network model accepts waveforms from eight neighbouring cells as input to learn the pattern of the coherent noise as well as that of the signal and outputs the probability of the first cluster arrival time of a hit at each sampling point. It was trained with samples of simulated waveform data, where hits are added randomly at the expected rate for $R_\mu = 3 \times 10^7\,\mathrm{s}^{-1}$, overlaid with real noise data taken without beam.

Combining the results by the two methods results in a higher hit efficiency but also a higher fake hit rate than the first method. To make the best use of the results of the two methods, the following reconstruction is repeated twice, with only the hits found with the first method and with the hits found with the two methods after combining them. The results are combined after the reconstruction is completed. If the reconstruction is successful with both methods, the higher quality tracks are selected. This approach improves the final tracking efficiency (see Sect. 4.6.2), by a factor of 1.26 compared to applying only the first method, but at the cost of 4 times the computational time for the track finding process described in Sect. 4.4.2 due to the higher number of hits.

The difference in the arrival times (α) and the ratio of the amplitudes (β) between the signals measured on the two ends of a wire provides information about the z-coordinate of the hit along the wire. Therefore, once a hit is detected in at least one of the two waveforms from a wire, these values are computed by minimising the following chi-square function,

$$\chi^2(\alpha, \beta) = \sum_k \frac{\left[v_i(t_k) - \beta \cdot v_j(t_k - \alpha)\right]^2}{\sigma_i^2 + \sigma_j^2}, \tag{3}$$

where i and j are indices for the wire ends (0: upstream end, 1: downstream end, and $i \neq j$), $v_i(t_k)$ is the waveform voltage at the k-th sampling point on the end where the hit is detected while $v_j(t_k - \alpha)$ is the voltage at the time $(t_k - \alpha)$ on the other end of the wire,[4] and $\sigma_{i(j)}$ is the RMS noise on the waveform. The index k runs for the points in the range $[-20\,\text{ns}, 10\,\text{ns}]$ around the detected signal timing. The resolution of the z-coordinate is several centimetres. Although this is moderate, it helps to ensure that the track finding process is efficient and robust against pile-up. The z-coordinate resolution is improved by exploiting the stereo configuration of the wires in the tracking stage.

Another piece of information provided by the digitised waveforms is the arrival time of the ionisation clusters on the sense wires. Since multiple clusters are frequently generated on one waveform, the time of the first cluster must be identified to correctly reconstruct the drift circle. This is measured from the summed waveform of the two ends after adjusting the relative timing of the two. The arrival time of cluster is the sum of the common track time (T_0) and the drift time of the cluster, where T_0 is measured by pTC measurement (see Sect. 5). The drift time of the first cluster is converted to the DOCA using the time-distance relationship (TXY tables) described in Sect. 4.4.2.

---

[4] The voltage between points is calculated with a linear interpolation.

4.4.2 Track finding and fitting

After identification and reconstruction, the hits are fed into a pattern recognition algorithm (track finder), followed by a track-fitter algorithm, both based on Kalman filters. The former combines hits belonging to the same positron track into a track candidate with a preliminary estimate of the positron's kinematics. The latter reconstructs the complete trajectory of the positron and provides the best estimate of the kinematics at the target: the positron energy E_{e+}, the emission angles (θ_{e+}, ϕ_{e+}) and the coordinates of the intersection of the track with the target, (x_{e+}, y_{e+}, z_{e+}).

The track-finding algorithm is based on a track following method that starts from hit pairs in outer layers, where occupancy is lower. All compatible combinations of two pairs in different layers form a set of track seeds. Each seed is propagated backward to the adjacent layers, with checking the consistency between the track and hits and updating the track parameters using the Kalman filter algorithm, until the innermost layer, and then propagated forward with attempting to find additional compatible hits to form full single turn track candidates. A track candidate is required to have at least seven hits.

The track fitter uses an extension of the Kalman filter, namely the deterministic annealing filter (DAF) [16] with iterative weighting and annealing process, implemented in the GENFIT package [17,18] with a proper treatment of the material effect. The left/right ambiguity is also resolved by DAF. The fitter first fits individual track candidates from the track finder and then merge the fitted segments to form full multi-turn tracks inside CDCH. Then, the tracks are propagated forward to the pTC and backward to the target. Once the track matches a pTC cluster, the track is re-fitted with updated DOCA using the best estimated T_0, with a correction of the time of flight from each hit to the pTC, and the best method of DOCA estimation discussed bellow. During this re-fitting, missing hits that the track finder was unable to associate to the track are searched for. Frequently, hits in the final half turn are missed by the track finder but can be added in this process, resulting in improved momentum resolution.

The deviation of the target from planarity is modelled by a triangle mesh in the fitter. The track is first propagated to a virtual plane, a few mm in front of the real target, and then to the nearest triangle of the mesh, where the positron's kinematics at the emission is reconstructed. The target crossing point (x_{e+}, y_{e+}, z_{e+}) is used as a candidate of muon decay point to correlate the track direction with the first interaction point of the γ-ray observed in the LXe detector. The length of the trajectory from the target to the matched pTC counter is converted to the time of flight and subtracted from the pTC hit time to determine the positron emission time at the target t_{e+}.

During the tracking process, the DOCA of each hit is iteratively refined. The DOCA value is estimated at the beginning using angle-averaged TXY tables extracted using Garfield++ simulations, which determine the drift velocity and lines taking into account the electric and magnetic fields, the ionisation pattern, the diffusion process, etc. The Garfield++ simulations are performed in two-dimensions in (r, ϕ) sampling at slices at fixed z-coordinates for each layer and then are interpolated to take into account the longitudinal change in cell size and shape as well as the effect of the magnetic field. Once the track is reconstructed, the DOCA is recalculated taking into account the cell crossing angle of the track. This DOCA estimation is biassed by the low cluster density; the small number of clusters within the cell overestimates the hit distance from the wire.

Another DOCA estimate less prone to intrinsic biases is obtained by neural network approaches [19]. The networks take as input various hit properties (wire and plane number, charge, timing, hit coordinates, track angle, T_0 etc.) and waveforms (for the CNN model) and train on the fitted track DOCA (made using the Garfield++ TXY tables) as an estimator of the true DOCA to create a "data-driven" TXY table. This TXY optimally accounts for ionisation statistics biases, removes errors from the simulated TXY, and uses information from all ionisation clusters.

The distribution of DOCA residuals for the conventional and two neural network based approaches, a dense neural network (DNN) and a CNN, are compared in Fig. 12. The best

result is obtained with the CNN that processes the waveforms from all ionisation clusters. The main improvement from the neural network is the suppression of the positive right tail presumably from the suppression of the ionisation statistics bias. This improves the positron kinematics by $\sim 10\%$ as shown in Sect. 4.6.1. Therefore, the DOCA is finally updated with the CNN method in the re-fit process.

4.5 Alignment

4.5.1 Wire alignment

The global position of CDCH was measured in both 2021 and 2022 with an optical survey. The information on the relative wire-by-wire alignment was extracted from several measurements during the construction of the chamber. However, after the complete reconstruction of the track, the distributions of the difference between the nominal position of the wires and the wire position calculated by the tracking algorithm using the measured DOCA show systematic deviations of the order of $\sim 100\,\mu$m, which worsen the tracking resolutions. The deviations were resolved by implementing a track-based alignment.

Two types of tracks can be used to improve relative alignment: Michel positrons and cosmic rays. The former have the advantage of being collected and reconstructed during normal data taking, but also the disadvantage of requiring a more complex reconstruction and being more affected by possible uncertainties in the knowledge of the magnetic field. The latter have the advantage of being straight tracks, but the disadvantage of requiring dedicated data taking periods and a different coverage of the tracking volume. Currently, alignment to cosmic rays is being investigated; in the following we only present the alignment based on Michel positrons.

The alignment procedure is an iterative adjustment of the wire coordinates driven by the mean residual. The residual r is fitted, wire by wire, as a function of the longitudinal position along the wire (z-coordinate) with a parabolic shape:

$$r(z) = p_0 + p_1 z + p_2 \left[\left(\frac{2z}{L} \right)^2 - 1 \right]. \tag{4}$$

The parameter p_0 corresponds to a global wire displacement, the linear term results from the inclination of the wire to the chamber axis and the quadratic term takes into account the wire sagitta, due to the electrostatic and gravitational forces acting on the wire. p_2 is the (absolute) maximum value of the sagitta, which can reach $\sim 100\,\mu$m.

The number of events required for high quality alignment of a single wire depends strongly on the position of the wire in the chamber due to the trigger criteria to select $\mu^+ \to e^+\gamma$ candidate events. Furthermore, the alignment algorithm is

Fig. 12 The distribution of the DOCA residuals (hit DOCA − track DOCA) estimated with the conventional (NML) and the two (DNN and CNN) neural network based approaches. The curves are fitted double Gaussian functions with a core sigma of 114 μm (119 μm) and a tail sigma of 236 μm (259 μm) with a core fraction of 0.59 (0.70) for the neural network (conventional) approaches

almost insensitive to alignment errors when the track direction is parallel to the misalignment vector. This is because the DOCA estimate does not change when the wire position is shifted along the track direction. Therefore, chamber sectors crossed by a large variety of angles are aligned more efficiently than those crossed with a small scatter of angles.

The alignment procedure was based on 17 million hits, with an average 40 hits per track. We required > 5000 hits for each wire to be aligned; 152 wires were excluded from this alignment and the survey results are used. They are at the edges of each layer or with electronic problems. With larger data statistics, the alignment for the edge region can be improved. One way to increase the statistics for the region is to use tracks outside the time window that do not cross the pTC but cross more frequently the CDCH regions outside or at the boundaries of the MEG II geometric and trigger acceptance. These tracks are collected accidentally when another event that meets the trigger conditions opens the WaveDREAM time window.

Figure 13 shows the final mean residuals in the x- (top plot) and y-coordinates (bottom plot) compared to the same residuals obtained using the survey-based alignment. The spreads of the Gaussian cores of the two distributions are $\sigma_x^{\text{sur}} = 22\,\mu\text{m}$ and $\sigma_y^{\text{sur}} = 35\,\mu\text{m}$ when the survey-based alignment is used and decrease to $\sigma_{x,y}^{\text{trk}} < 5\,\mu\text{m}$ for both coordinates after the alignment procedure.

The fit parameters p_0 (global displacement) and p_2 (sagitta) are strongly correlated, as expected. The remaining sagitta is $\sigma_{p_2} \sim 13\,\mu\text{m}$ and the wires with the largest sagittas are concentrated in the peripheral chamber sectors, crossed by fewer tracks than central sectors. The distributions of the displacements of the wire centres with respect to those in the survey have $\sigma_x \sim 100\,\mu\text{m}$, $\sigma_y \sim 80\,\mu\text{m}$ and $\sigma_z \sim 30\,\mu\text{m}$. The distributions of the differences of the wire angles Θ and Φ with respect to the survey have $\sigma_\Theta \sim 0.1\,\text{mrad}$ and $\sigma_\Phi \sim 1.1\,\text{mrad}$, respectively. For the Φ angle the mean value is 1.05 mrad, which means that the alignment requires a global azimuthal rotation, while the required polar rotation is minimal, i.e. $< 0.1\,\text{mrad}$.

The remaining error in wire-alignment is estimated to be between $2\,\mu\text{m}$ at the centre and $15\,\mu\text{m}$ at the end plates. Some correlations between the wire centre translation or the wire rotation and the wire number layer-by-layer have been observed and are currently being investigated.

The effects of the alignment procedure on the resolutions of the kinematic variables are evaluated using the double-turn method; see Sect. 4.6.1 for the details. The distributions of z_{e^+} and ϕ_{e^+} are shown in Fig. 14. The advantage of the alignment procedure is highlighted by the strong reduction of the systematic biases and by the narrowing of the distributions.
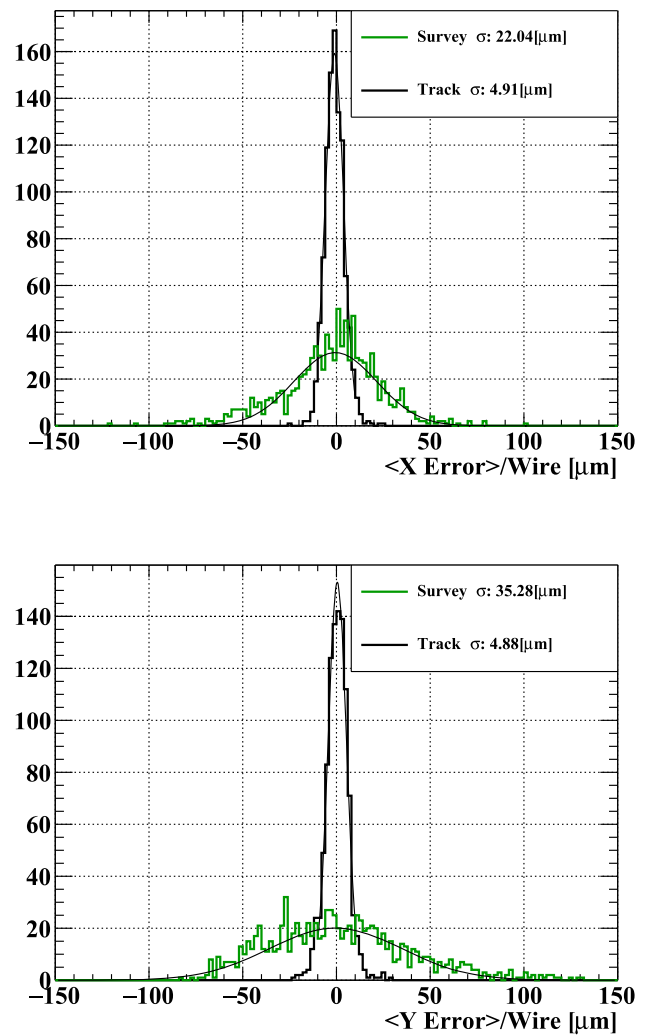
Fig. 13 The mean residuals in the x- (top plot) and in the y-coordinates (bottom plot). The black curves are obtained after 14 alignment iterations, the green curves using the alignment based on the survey. The curves are the results of Gaussian fits

4.5.2 Relative alignment between magnetic field and CDCH

Due to the gradient magnetic field, misalignment between the CDCH and the magnet results in a non-uniformity of the energy scale with respect to the positron emission angle. In the track reconstruction, we use a 3D map of the magnetic field calculated using a finite element method based on the measured coil dimensions and taking into account the thermal shrinkage of the coil. The angular dependence is minimised by shifting the calculated magnetic field by $(100\,\mu\text{m}, 700\,\mu\text{m}, 300\,\mu\text{m})$ from the nominal position, with an estimated alignment accuracy of $100-200\,\mu\text{m}$. After the shift, there is no more bias as shown in Fig. 15, and the scatter of the order of $\sim 10\,\text{keV}$ is negligible compared to the energy resolution.
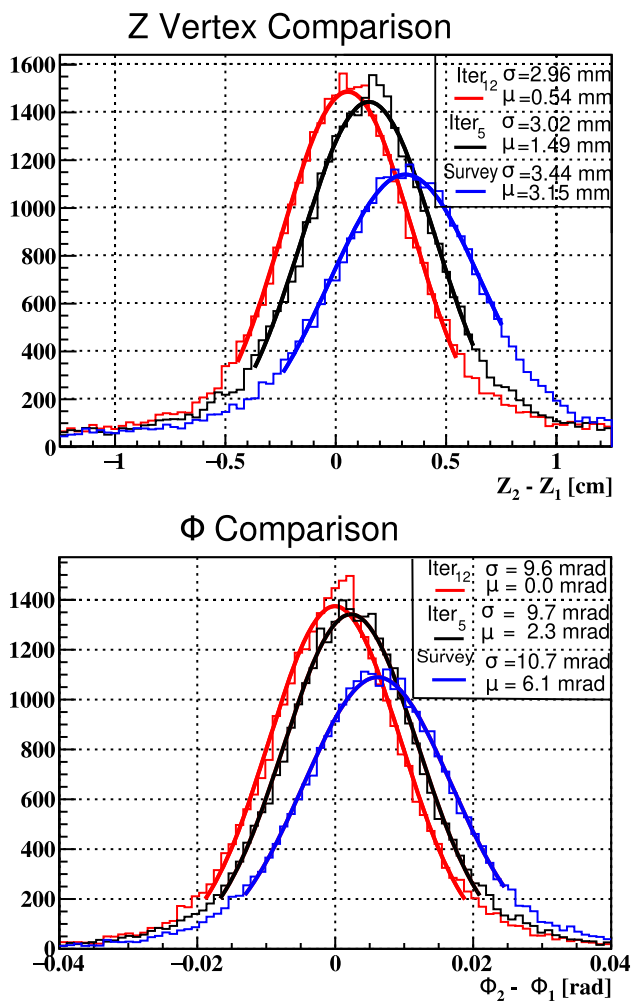
Fig. 14 The double-turn analysis results for z_{e+} and ϕ_{e+}. The blue curves are obtained using the survey-based alignment, the black and the red curves using the alignment algorithm results after 5 and 12 steps, respectively
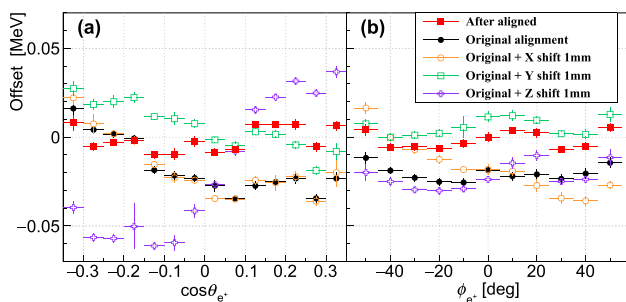
Fig. 15 The angular dependence of the positron energy scale versus the angular kinematic variables before and after alignment. The offset on the y-axis is the difference of the measured value with the expected value of the Michel edge. The three superimposed plots show the effects of shifting the magnetic field by 1 mm in x, y, and z

The misalignment in the positive x direction results in a decreasing energy scale versus ϕ_{e+} and $\cos\theta_{e+}$. The misalignment in the positive y direction results also in an
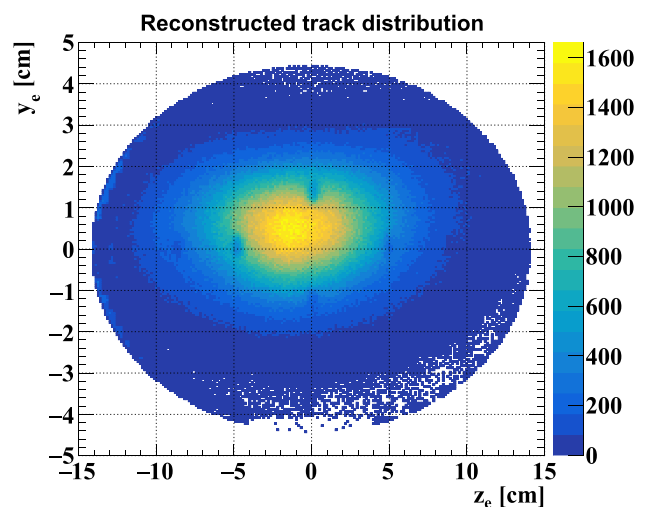
decreasing energy scale versus $\cos\theta_{e+}$. The misalignment in the positive z direction results in an increasing energy scale versus $\cos\theta_{e+}$.

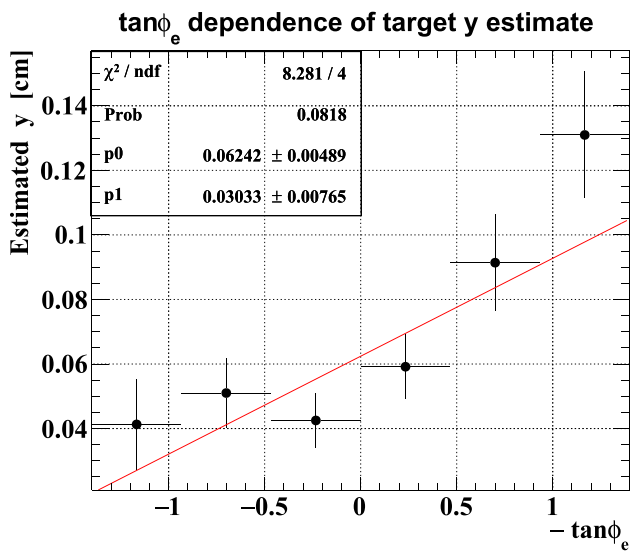### 4.5.3 Relative alignment between target and CDCH

The precise alignment of the muon stopping target with respect to the spectrometer is crucial in determining the positron emission angle and position as discussed in detail in Sect. 3. We use the holes on the target to align the target with respect to the CDCH. The six holes are visible (as shortage of events) in the reconstructed track distribution in Fig. 16, from which the y- and z-coordinates of the holes (thus those of the target) can be easily estimated. With reference to Fig. 4 the hole centres are located approximately at ± 1 cm along the short axis and ± 5 cm and ± 8.5 cm along the long axis.

The x-alignment exploits the dependence of the estimated y-position on ϕ_{e+}, as shown in Fig. 17. Combined with the photogrammetric method using the photo-camera system, which corrects for temporal variation in the target positions, the hole analysis yields the hole-by-hole residual misalignment.

The precision of the hole-by-hole position estimation is limited both by the statistical uncertainty of the positron tracks and by the systematic uncertainties of the method. The statistical uncertainty is $100-200\,\mu$m in each coordinate. All the systematic uncertainties originate from the non-uniform vertex position distribution due to the beam profile, which biases the (y, z) distribution produced by the holes to be closer to the beam centre. This effect is corrected in the hole position estimation, but the uncertainties in the correction factor dominates the hole-by-hole systematic uncertainties of $(50\,\mu\text{m}, 100\,\mu\text{m}, 200\,\mu\text{m})$.

Fig. 16 Distribution of the reconstructed positron origin (y_{e+}, z_{e+}) on the target

Fig. 17 Estimated hole y position as a function of ϕ_{e^+}. The slope parameter in the fit gives the residual x misalignment while the offset parameter gives the y offset of the target

4.5.4 Relative alignment between LXe detector and CDCH

The alignment procedure described in Sect. 4.5.1 is insensitive to a global misalignment between CDCH and other subdetectors. Among them, the LXe detector is especially important since it provides information about the γ-ray direction.

Events that result with hits in both the CDCH and the LXe detector are used to compare information from both. The appropriate event category is the cosmic rays, which can release energy in the LXe detector and then (or vice versa, depending on the trajectory) pass through the CDCH, producing hits on multiple wires. The cosmic ray events are collected with a specific triggering scheme and with the magnetic field turned off, to obtain straight tracks that are easier to reconstruct and fit. The idea is to select cosmic ray tracks that cross the LXe detector inner face almost perpendicularly and to determine the coordinates of this crossing point using the LXe detector and the CDCH information independently.

On the CDCH side, a method based on the Legendre transform [20,21] is used for finding and fitting the cosmic ray tracks. The fitted tracks are then extrapolated to the inner face of the LXe detector.
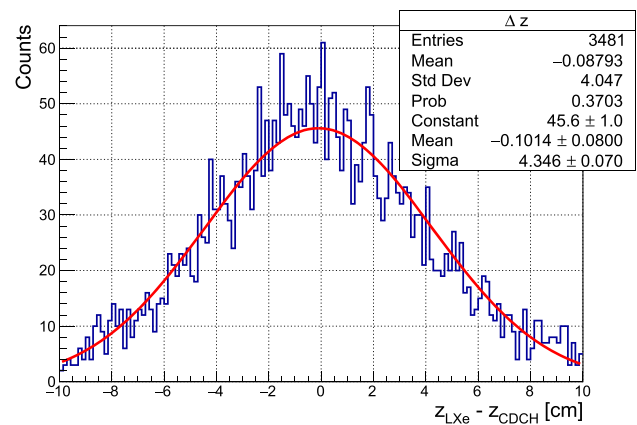
Fig. 18 Difference in the reconstructed z-coordinate on the entrance face of the LXe detector for cosmic rays performed by using the LXe detector and CDCH information independently. The red curve is a Gaussian fit

On the LXe detector side, the usual position reconstruction algorithm (see Sect. 6.4) is applied. The selection of cosmic ray tracks almost perpendicular to the detector entrance face is motivated by the fact that the continuous stream of energy release by such cosmic rays is seen from the photosensors on the inner face as a point-like energy deposit, whose position is more reliably reconstructed.

Figure 18 shows the LXe–CDCH difference in the reconstructed z-coordinate $\Delta z = z_{LXe} - z_{CDCH}$. The distribution has a Gaussian shape, centred at $\Delta z = (-1.0 \pm 0.8)$ mm. This result shows that a small global shift can be applied to better align the two detectors even if it is compatible with zero.

We do not observe any significant deviation in the difference in ϕ within its uncertainty, which is more subject to systematic errors in the measurement because of non-uniform distribution of the cosmic rays with respect to ϕ.

The relative alignment between the LXe detector and the CDCH, combined with the relative alignment between the CDCH, the magnetic field and the target, is sufficient to determine the relative positron–photon angle, which is independent of the absolute position of the detectors.

For practical reasons, we need to define an absolute alignment. Reference marks on the COBRA cryostat are used to define the absolute MEG II reference frame. The position of the CDCH in this reference frame is determined by an optical survey with an estimated resolution of a few hundred micrometres, while the absolute position of the LXe detector is measured with uncertainties of $\sim 600\,\mu$m as discussed in Sect. 6.4. On this basis, we decided to use the CDCH position as a reference and apply global shifts to the LXe detector, the magnetic field and the target, according to the results of the data analysis for the relative alignments. The shifts of the magnetic field and target, reported in Sects. 4.5.2 and 4.5.3, are quite similar in size and direction, which could

The global target geometry, both the rotational and translational parameters, is finally fitted to the residuals of the holes, yielding a translation of $(73\,\mu m, 799\,\mu m, 437\,\mu m)$ and a rotation of 10 mrad mainly along the minor axis of the target from the results of the photogrammetric method. The accuracy, including systematic uncertainties, is $100\,\mu m$ for the translation in each axis and 1.4 mrad (6 mrad) for the rotation along the minor (major) axis.

indicate a bias in the CDCH survey. The shift in the z direction is also confirmed by the relative alignment between the CDCH and the LXe detector, but with a large uncertainty. For these reasons, the shift to be applied to the LXe detector was determined by combining all available information on a possible bias in the CDCH survey. We obtained $(90\,\mu m, 800\,\mu m, 630\,\mu m)$, with a systematic uncertainty of 1 mm assigned in all directions.

4.6 Performance

In this section, we discuss the performance of the CDCH in terms of resolution and tracking efficiency. A more extensive discussion is given in a dedicated paper [15]. We recall that the main motivation for building the CDCH was the unsatisfactory performance of the MEG drift chamber system in terms of angular and energy resolutions and tracking efficiency due to its segmented structure.

4.6.1 Resolutions

One technique for evaluating the resolutions of the kinematic variables is the "double-turn" method, which was already used in the MEG experiment[2]. In the MEG II experiment, $\sim 15\%$ of the positron tracks cross the chamber volume five times, passing through 9×5 sense wire layers. In these tracks, one can identify two separate track segments ("turns"), the first of which corresponds to two chamber crossings and the second to three chamber crossings. Both track segments are independently fitted and propagated to a plane parallel to the target between the two turns and the distributions of the
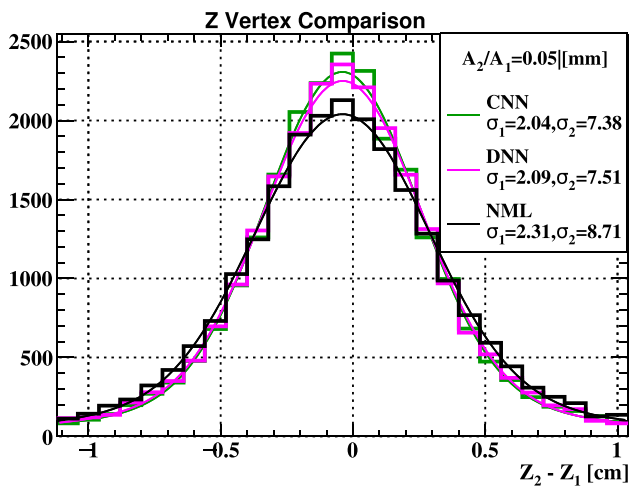
Fig. 19 The distribution of the double-turn difference for z_{e+} obtained using the conventional (NML) and neural network (DNN and CNN) approaches to DOCA reconstruction fit with a double Gaussian. $A_{1,2}$ are the amplitudes of the two Gaussians, the ratio is fixed to 0.05; $\sigma_{1,2}$ are their standard deviations in mm

Table 2 Effective resolutions (core σs) for experimental data obtained by combining the double-turn results on data with the MC correction factors. The design values are in Table 6

$\sigma_{y_{e+}}$ (mm)	$\sigma_{z_{e+}}$ (mm)	$\sigma_{\phi_{e+}}$ (mrad)	$\sigma_{\theta_{e+}}$ (mrad)
0.74	2.0	4.1	7.2

differences between the kinematic variables reconstructed by the two segments are compared.

Figure 19 shows the double-turn distributions for z_{e+}; the shapes of the y_{e+}, ϕ_{e+} and θ_{e+} distributions are similar. The three distributions of Fig. 19 are based on the conventional and the neural network based DOCA reconstructions described in Sect. 4.4.2. The neural network approaches improve the width of the distribution by $1-11\%$.

These distributions do not directly represent the effective resolutions of the CDCH, but a combination in quadrature of the resolutions of the first and second turn. The following corrections are required to convert the double-turn results into reliable estimates of the real resolutions. One is to correct for the bias in the double-turn evaluation due to difference in magnetic filed and properties between the two turns and with Michel positrons. Another is to correct for the difference between Michel positrons and the signal positrons due to the different numbers of hits. Both correction factors were evaluated via MC simulations. Good similarity was obtained between the double-turn results on data and those on the Michel MC simulation, showing that we have a solid knowledge of the response of the CDCH. In addition, we can correct for the correlation effect between the variables for the detection of $\mu^+ \to e^+\gamma$ events as discussed in Sect. 10. The correlation parameters are also evaluated with the double turn analysis. The effective resolutions after the corrections are summarized in Table 2.

The energy resolution for experimental data is measured by fitting the theoretical Michel spectrum multiplied by an efficiency function that takes into account the high-energy selection of the spectrum by the spectrometer acceptance and then convoluted with the resolution function formed by the sum of three Gaussian functions to the measured Michel positron spectrum. The result is shown in Fig. 20 in both logarithmic (a) and linear (b) scales. The σ of the core Gaussian function, which accounts for $\sim 67\%$ of the integral of the resolution curve, is $\sigma_{E_{e+}} = 91\,keV$, better by 40 keV of the value quoted in the MEG II proposal. The corresponding value for the MEG experiment was $\sigma_{E_{e+}} = 320\,keV$.

4.6.2 Efficiency

Figure 21 shows the CDCH tracking efficiency for signal positrons $\varepsilon_{e+,CDCH}$ versus R_μ. The efficiency is defined as the ratio of the number of reconstructed positrons in the signal
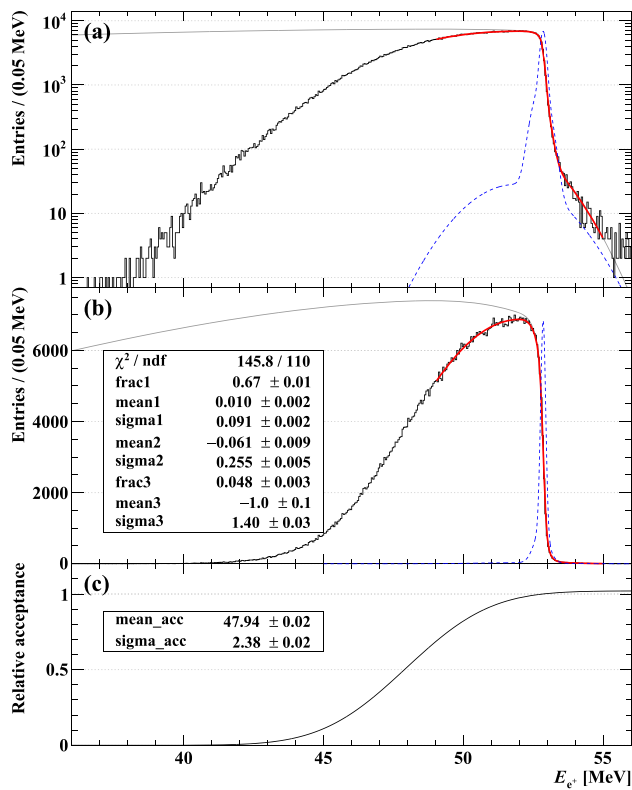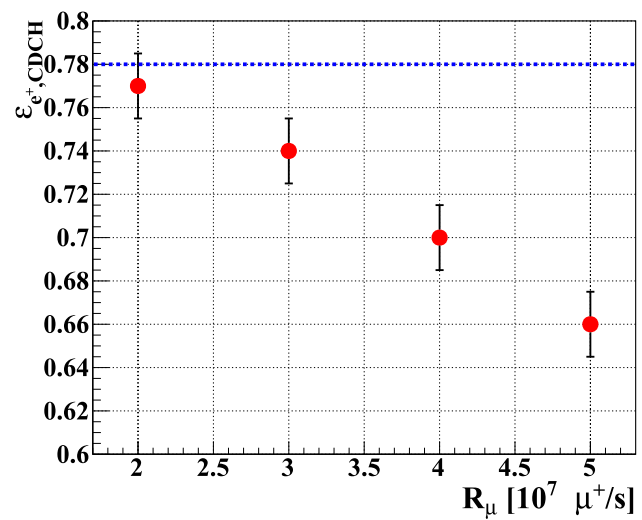
Fig. 20 Fit of the Michel positron spectrum in logarithmic (**a**) and linear (**b**) scales. The black histogram is the experimental distribution, the blue curve is the sum of three Gaussian functions describing the resolution around the signal region and the red curve is the fitted function, obtained from the theoretical spectrum multiplied by the acceptance curve shown in **c** and then convoluted with the resolution function. **c** The acceptance curve of the spectrometer modelled with an error function

Fig. 21 CDCH tracking efficiency as a function of R_μ for signal positrons. The blue dotted line is the design value

than with the MEG drift chamber. The MEG experiment used $R_\mu = 3 \times 10^7 \, \text{s}^{-1}$, with a positron efficiency of $\varepsilon_{e^+} \sim 30\%$. At the same R_μ, the positron efficiency is $\varepsilon_{e^+} = \varepsilon_{e^+,\text{pTC}} \times \varepsilon_{e^+,\text{CDCH}} \sim 67\%$.
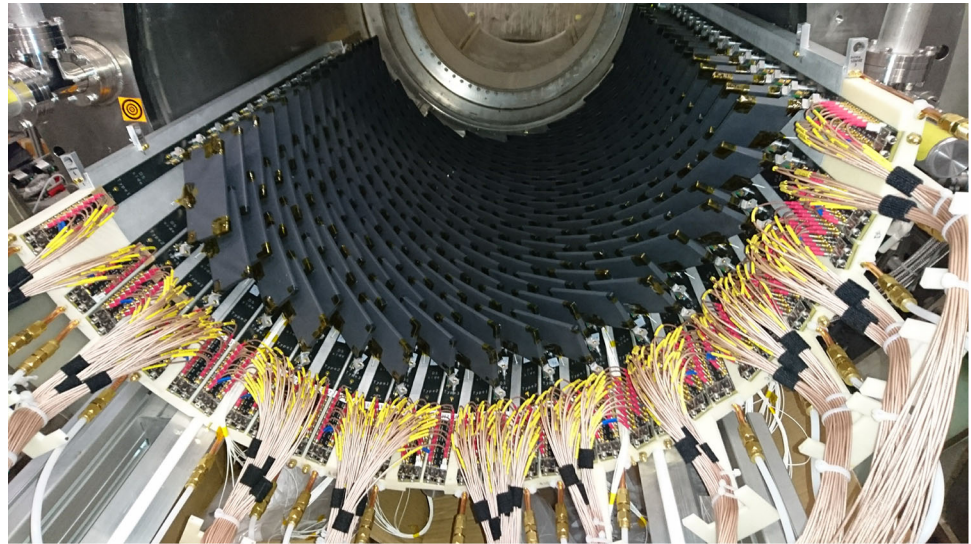
4.7 Back-up chamber

The detailed analysis of the problems of wire breakage stimulated a long R&D effort to explore possible alternatives to the silver-coated aluminium wires, which were found to be fragile and easily damaged by ambient humidity, with the aim of designing and building a new chamber (CDCH2) without the above problems. Several possible types of wire were explored, with different coating materials (gold and nickel), without coating etc. They were studied from multiple aspects: sensitivity to corrosion processes, mechanical strength, soldering technique on PCBs, etc. We developed a system for measuring wire tension [22], based on the resonant frequency method, as well as with wiring and assembly stations [23]. The final choice was a wire made of pure aluminium with a diameter of 50 μm, which is almost insensitive to corrosion and can be efficiently and solidly fixed on PCBs by a combination of soldering and gluing with suitable chemical products. The CDCH2 is scheduled for completion by the end of 2023 and delivery to PSI in spring 2024. At that time, the collaboration will decide whether and when to replace the current chamber.

5 Pixelated timing counter

Measuring the time coincidence between a e^+ and a γ-ray with the highest resolution is crucial for reconstructing

energy region to the number of emitted positrons in the direction opposite to the LXe acceptance region and detected by the pTC. Since the efficiency depends on the positron energy, it is measured for energies just below the signal energy and its value is extrapolated to the signal energy. The sample used for the calculation is taken through a minimum bias trigger that requires only one hit on the pTC. It is expected that the efficiency decreases with R_μ, because as R_μ increases, the probability of pile-up also increases, making the track-finder algorithm less effective at identifying hits belonging to individual tracks. Nevertheless, the reduction in efficiency from the lowest value of $R_\mu = 2 \times 10^7 \, \text{s}^{-1}$ to the highest $R_\mu = 5 \times 10^7 \, \text{s}^{-1}$ is moderate < 15%. The blue dotted line represents the design value, which is almost reached at the smallest value of R_μ and is not far from being reached also at the highest. As a reference we measure $\varepsilon_{e^+,\text{CDCH}} \sim 74\%$ at $R_\mu = 3 \times 10^7 \, \text{s}^{-1}$.

The CDCH is highly transparent towards pTC and allows a high signal detection efficiency for pTC, $\varepsilon_{e^+,\text{pTC}} = (91 \pm 2)\%$ (discussed in Sect. 5.5), which is twice higher

**Fig. 22** The downstream pixelated Timing Counter

$\mu^+ \rightarrow e^+\gamma$ like events in a high R_μ environment. The pTC was developed to measure the e^+ impact time, from which the emission time at the target plane t_{e^+} can be derived by correcting for the track length reconstructed by CDCH. It also plays an active role in the trigger algorithms by providing information for event selection based on time coincidence and directional matching with the γ-ray measurement with the LXe detector.

5.1 Concept and design

The detector consists of two semi-cylindrical sectors arranged mirror-symmetrically upstream and downstream of the target, within the volume between CDCH and the inner wall of the COBRA magnet. Figure 22 shows an illustration of the downstream sector. The support structure consists of a 20 mm thick semi-cylindrical aluminium shell. Plastic scintillator counters are mounted on 16 back-planes running in the z-direction along the structure. To ensure temperature-stable operation, water flows from a cooling system through copper pipes embedded in the structure.

The pTC extends in the z–ϕ plane $23 < |z| < 117$ cm and $-166° < \phi < 5°$ to cover the angular acceptance of $\mu^+ \rightarrow e^+\gamma$ positron candidates with a back-to-back γ-ray reaching the fiducial volume of the LXe detector.

Each sector is segmented into 256 plastic scintillator tiles (Bicron BC422® [24]), coupled to an array of silicon photomultipliers (SiPMs) glued on two opposite sides as shown in Fig. 23. Each array consists of six SiPMs connected in series. Near-ultraviolet sensitive AdvanSiD SiPMs with an active area of (3×3) mm^2 and a pixel pitch of 50 μm (ASD-NUV-SiPM3S-P) are used. Their spectral response matches well with the 370 nm peak emission of BC422. Each tile is wrapped with a highly efficient 35 μm thick polymeric reflector (VIKUITI 3M Mirror Film®) to increase light reflectance
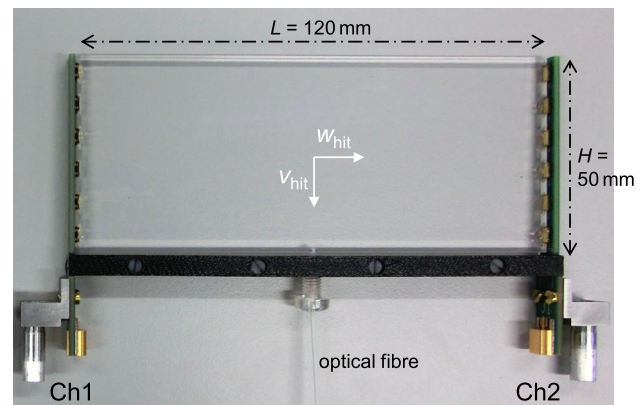
Fig. 23 A naked counter with $H = 50$ mm. The coordinates $(v_{\text{hit}}, w_{\text{hit}})$ are the counter local coordinates used in reconstruction in Sect. 5.3

at the surface, and finally wrapped again with a 30 μm thick black TEDLAR® film.

The counter sizes (length L, height H and thickness T) and locations were optimised using MC simulations. The best trade-off between single-counter performance, number of hits for a signal positron (hit multiplicity), detector efficiency and number of channels was found with $L \times H \times T = (120 \times 40 \times 5)$ mm^3 and $(120 \times 50 \times 5)$ mm^3 tile sizes (the two different H are used in different regions to maximise hit multiplicity while keeping the highest efficiency). The counters are arranged at a fixed radius (the top of each counter at $r = 29.7$ cm) in a 16×16 matrix arranged in the z–ϕ plane. The longitudinal and angular distances between adjacent counters are 5.5 cm and 10.5°, respectively. Each line at fixed z is offset by half a counter from the previous one; in addition, the counters are tilted by 45° so that they are nearly perpendicular to the signal positron trajectories. This configuration was chosen to maximise the average hit multiplicity for a signal-like positron. The idea behind the detector design

Fig. 24 Map of counter hit rates measured at $R_\mu = 5 \times 10^7 \, s^{-1}$ in 2022 run. Each circle indicates a counter and the colour shows the hit rate
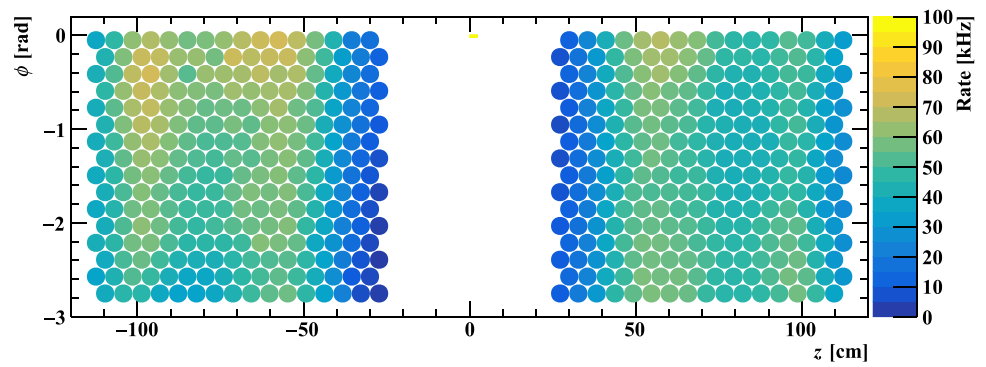
is to take advantage of both the good single-counter resolution (below 100 ps measured in laboratory tests [25]) and the combination of multiple hit information. The mean hit multiplicity per signal event reconstructed from MC, $\langle N_{hit} \rangle \sim 9$, leads to the expectation of a total time resolution down to $\sigma_{t_{e^+},pTC} \sim 40 \, ps$.

Most counters (except those at low $|z|$, due to mechanical constraints) are connected to a laser source via optical fibres. The signals generated by sending synchronous light pulses with the laser to the counters are used to check detector stability and to calibrate the inter-counter time offsets as described in Sect. 5.4.

5.2 Operation

The R&D for the pTC single counter began in 2013 [26]. The full detector was developed and finally commissioned in 2017 [25], when it was tested in the MEG II spectrometer under experimental conditions. Since then, it has always been operational during the MEG II engineering runs, which were conducted once a year.

During standard operation of the pTC, the circulating water is maintained at the fixed temperature of 9 °C, resulting in an effective SiPMs' temperature range of 11.0 to 14.5 °C, depending on their position. The detector volume is constantly purged with dry air to maintain low humidity and prevent a dew point from being reached.

The breakdown voltage for each SiPM array was extrapolated from I–V curves recorded at fixed temperature (30 °C). Data collection at different temperatures allowed extraction of the coefficient of breakdown voltage as a function of temperature, resulting in 24 mV °C^{-1}/SiPM. The optimal operating voltage for each SiPM array was then first determined in laboratory tests by measuring time resolution as a function of overvoltage, and then optimised at the beginning of each run to maximise the signal-to-noise ratio under experimental conditions. A typical value for an array of six-SiPM is $\sim 164 \, V$, i.e., an overvoltage of 3.2 V/SiPM.

Since the engineering run in 2017, the detector has been running very stably. Only a tiny number of channels (one in 2021, four in 2022) proved dead (i.e., they have no signal).

The malfunctioning and dead counters have been replaced with spare ones during the maintenance period. The distribution of pTC hit rate shown in Fig. 24 can be used as a diagnostic and monitoring tool for beam and background. For example, the asymmetry between upstream and downstream is due to the polarisation of the muon beam and the muon decays off-target. The distribution of the hit rate agrees well with that of MC; no unexpected background is observed. Due to the finely segmented configuration, the hit rate of each counter is $< 75 \, kHz$ despite of the total pTC hit rate of $\sim 3 \, MHz$ at $R_\mu = 5 \times 10^7 \, s^{-1}$.

5.2.1 Issues and problems

During the first years of operation, some problems related to the detachment of SiPMs from the scintillator surface occurred, probably caused by mechanical stress on the SiPM board and loose adhesion of the optical resin to polished surfaces. For this reason, a small subset (a few dozen) of the counters were removed from the detector and glued back on, after applying manually some small scratches to the scintillator surfaces glued to the SiPMs, to ensure better adhesion.

An increase in the dark currents of the SiPMs was observed, likely due to radiation damage in the Si bulk. The e^+ fluence in 2021–2022 runs is $\sim 1.5 \times 10^{10} \, cm^{-2}$ at the highest hit rate region. The behaviour of the dark current as a function of the total muons stopped on target during the last two years is shown for some channels in Fig. 25. The dark current increment varies between channels due to position-dependent e^+ hit rates and different operating overvoltages. On average, the increment rate is $9 \, nA/(10^{12}\mu^+)$ and $13 nA/(10^{12}\mu^+)$ in 2021 and 2022, respectively, which correspond to $\sim 40-50 \, nA \, d^{-1}$.

This effect has been studied in detail [27] and a clear correlation between the increase in dark current and the degradation in time resolution has been demonstrated. Based on these studies, we expect a degradation of the overall time resolution of $\sim 13\%$ after three years of MEG II running. Although this does not affect the detector performance, we decided to refurbish the detector, by replacing ~ 100 counters.
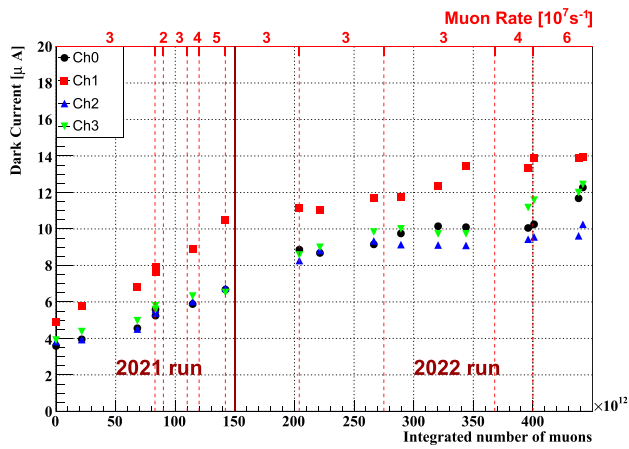
Fig. 25 The dark currents of some channels compared to the integrated number of stopped muons on target. The vertical dashed lines define the periods with the muon rates shown above

5.3 Reconstruction algorithms

The e^+ impact time t_{hit} and the position along the long side of the scintillator w_{hit} for each counter are reconstructed from the timing of the SiPM signals ($t_{Ch1(2)}$ for channel 1 (2) of the counter):

$$t_{hit} = \frac{t_{Ch1} + t_{Ch2}}{2} - \frac{O_{Ch1} + O_{Ch2}}{2} - \frac{L}{2v_{eff}}, \tag{5}$$

$$w_{hit} = v_{eff} \left(\frac{t_{Ch1} - t_{Ch2}}{2} - \frac{O_{Ch1} - O_{Ch2}}{2} \right), \tag{6}$$

where $L = 120\,\mathrm{mm}$ is the length of the scintillator, $O_{Ch1(2)}$ is the time offset for the channel, and v_{eff} is the effective speed of light in the scintillator; $O_{Ch1(2)}$ and v_{eff} are counter-dependent parameters discussed in Sect. 5.4. The signal pulse shape after a shaping amplifier[5] has a rise time of ≈ 1.4 ns and a full width at half maximum of ≈ 2.8 ns. The $t_{Ch1(2)}$ is extracted from the pulse using the digital-constant-fraction method, which calculates the crossing time of the signal at a given fraction of the total amplitude. In the offline analysis, different fractions were tested and the fraction with the best time resolution was determined separately for each channel (usually 25%). The local hit coordinate is transformed into the global coordinates using the counter geometry (position and rotation).

A positron usually leaves hits in multiple counters. The series of hits are grouped by a clustering algorithm using the hit timing and position information. The same e^+ can hit counters after exiting the pTC region and travelling another half a turn. These hits are grouped into a different cluster.

---

[5] The shaping is based on a pole-zero cancellation circuit mounted on the WaveDREAM board.

The highly granular counter configuration allows estimation of the e^+ trajectory from the hit pattern of each cluster. A look-up table that relates the hit pattern to the radial hit coordinate (v_{hit}) was created based on the MC simulation and used to infer v_{hit} for each hit belonging to the cluster. The cluster timing and position information is passed to the track-finding algorithm to provide the track time T_0 and seed the tracks in CDCH.

The cluster information is next fed into a DAF to fit the trajectory inside the cluster. Two track fitting procedures are applied to each cluster. One is the pTC self-tracking, which uses solely the pTC cluster information and is used for calibration and performance evaluation. The other uses the track reconstructed with CDCH and combines it with the pTC hits. First, a matching test is made between the CDCH tracks and the pTC clusters, and then, the track is extended to the end of the last pTC hit in the cluster for each matched combination. If multiple clusters matched with a single CDCH track, the first one along the trajectory is adopted. During the annealing process of DAF, temporally or spatially inconsistent hits are removed. This filtering process eliminates not only the contamination of hits by different particles but also hits by the same e^+ with small turns after the main passage, which are the main cause of the tail in the pTC timing response.

Figure 26 illustrates the clustering and tracking processes with an example event observed in 2021 at $R_\mu = 5 \times 10^7\,\mathrm{s}^{-1}$.

The timing information in a cluster is combined into the impact time of the first counter:

$$t_{e^+},\mathrm{pTC} = \sum_{i=1}^{N_{hit}} \left(t_{hit,i} - f_{1,i} \right) / N_{hit}, \tag{7}$$

where N_{hit} is the number of hits in the cluster, $t_{hit,i}$ is the reconstructed hit time of the i-th hit and $f_{1,i}$ is the time of flight from the first hit to the i-th hit calculated from the length of the fitted track. Finally, the time of the e^+ emission at the target is calculated as,

$$t_{e^+} = t_{e^+},\mathrm{pTC} - f_{0,1}, \tag{8}$$

where $f_{0,1}$ is the time of flight from the target to the first hit calculated from the track length (see Sect. 4.4.2).

5.4 Calibration and alignment

The measured signal timing on each channel contains its own time offset ($O_{Ch1(2)}$) due to different lengths of the readout chain, the variety of scintillator and SiPM responses and differently optimised parameters of the digital-constant-fraction method, resulting in the misalignment of the hit times (see Eq. (5)) and positions (see Eq. (6)) of individual counter
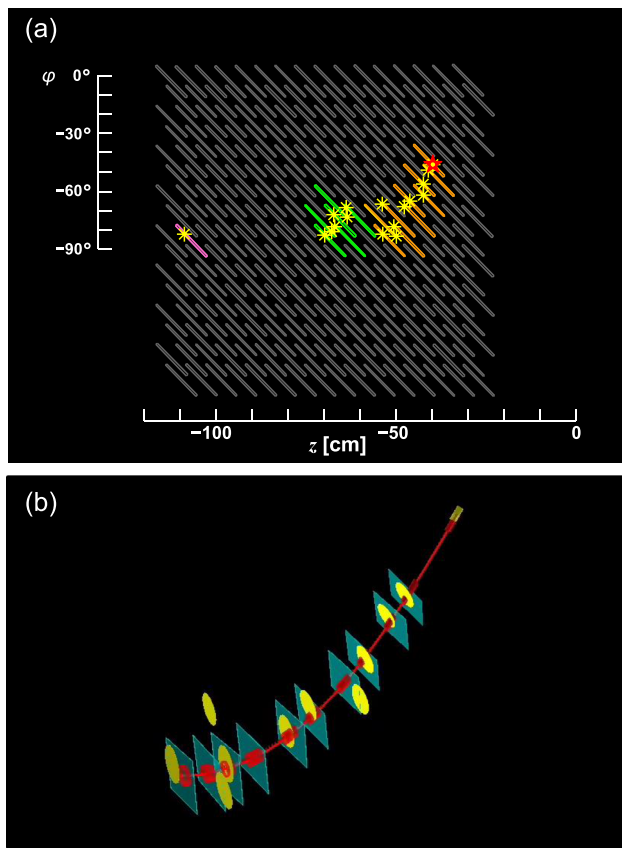
Fig. 26 An example of pTC hits in an event. **a** The ϕ–z view of the upstream sector. Counters with hits are shown in colour; different colours show different clusters. The yellow asterisk markers show the reconstructed hit positions and the red star marker shows the point matched with the track from CDCH. The first (orange) and second (green) clusters coincide within 2 ns and thus originate from a single e^+ in different turns. They are separated into different clusters by the spatial information. The third (magenta) one originates from another particle well separated in time (+180 ns). **b** A 3D view of the first cluster. The cyan squares show the counter planes (arbitrary size), the yellow ellipses show the reconstructed hits, and the red curve shows the fitted track. The seventh hit is incompatible with the others, most likely due to a hit of a secondary particle from the main e^+, and the weight becomes zero in the annealing process of DAF

measurements. From Eqs. (5) and (6), it is more effective to calibrate the linear combinations of $O_{Ch1(2)}$ than to calibrate them separately.

To align the local w_{hit} coordinate, v_{eff} and

$$O_{intra} = \frac{O_{Ch1} - O_{Ch2}}{2} \qquad (9)$$

are calibrated using the w_{hit} distribution obtained with the Michel positrons. Since the scintillator length L is precisely controlled ($\mathcal{O}(10\,\mu\text{m})$), we use this physical boundary condition. The centre of the distribution reflects O_{intra} and the width does v_{eff}. The precision of this method was evaluated

to be 1.1 mm, which is much better than the w_{hit} resolution of ~ 10 mm.

The alignment of each counter relies on two types of optical survey. One is a three-dimensional scan of the entire pTC structure including individual counters using the FARO EDGE SCANARM. This was performed on completion of the assembly prior to installation. From the scanned data, the position and rotation of each counter was reconstructed relative to reference points for spherically mounted retro-reflectors (SMRs). The other is a three-dimensional survey using the Leica Laser Tracker. This was performed in situ after the installation and measured the reference points with the SMRs in the MEG II global coordinate system. By connecting the reference points, the position and rotation (six parameters) of each counter were determined to an accuracy of a few 100 μm.

To align inter-counter timing, the following variable is calibrated for each counter:

$$O_{inter} = \frac{O_{Ch1} + O_{Ch2}}{2} + \frac{L}{2v_{eff}}. \qquad (10)$$

Two complementary methods were developed: the track-based method and the laser-based one. The former uses the Michel positron tracks and the latter uses a dedicated laser system. Details of the laser system and the method are given in [28].

The track-based method calculates a set of inter-counter time offsets $O_{inter,k}$ ($k = 1, \ldots, 512$ is the counter ID) by minimising the following χ^2 for a given data set of Michel positrons,

$$\chi^2 = \sum_{j=1}^{N_{cluster}} \sum_{i=1}^{N_{hit}^j} \left[\frac{t_{hit,i}^j - \left(t_{1st}^j + f_{1,i}^j + O_{inter,k_i} \right)}{\sigma_i^j} \right]^2, \qquad (11)$$

where j runs for all clusters with successful pTC self-tracking in the data set, i runs for hits in the cluster, t_{1st}^j is the e^+ impact time at the first hit in the cluster and it is a floating parameter in the minimisation (local parameter), the time of flight $f_{1,i}^j$ is computed by the self-tracking, and σ_i^j is the uncertainty of each measurement represented by the mean counter time resolution. The minimisation is solved with a linear least squares fit using Millepede II [29].

The track-based method can calibrate $O_{inter,k}$ relatively between the counters in a sector for a given data set. The laser method is used to connect the two sectors and to trace the temporal variation. Figure 27 shows the temporal variation of $O_{inter,k}$ in 2022 traced by the laser method. Until the 10th of August 2022, the commissioning of the run, such as exchange of electronics boards and optimisation of the bias voltages, had been made and hence the whole detector system had been unstable. The laser method allows monitor-
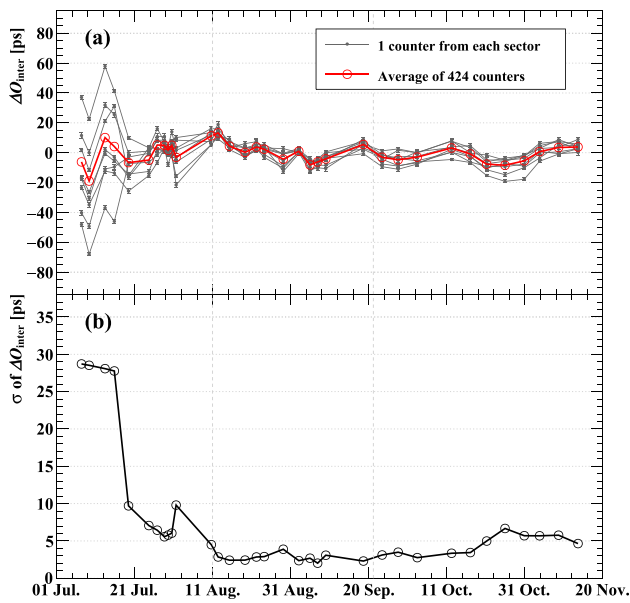
Fig. 27 **a** Temporal variation of the pTC counter time offsets O_{inter} in 2022 traced by the laser calibration. For this plot, the offsets were calibrated and aligned with the data between 11th August and 22nd September, and therefore ΔO_{inter} denotes deviation from them. The grey graphs are for sampled counters from different groups of optical paths in the laser system and the red one is for the average for all 424 laser-equipped counters. **b** The dispersion of ΔO_{inter} for the 424 counters
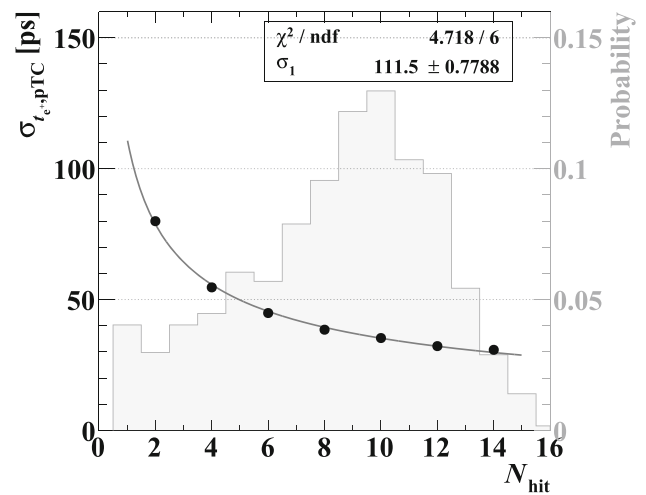

Fig. 28 Time resolution of pTC as a function of the number of hits evaluated by the even–odd analysis on the 2021 data. The curve $\sigma_{t_{e^+},\text{pTC}}(N_{\text{hit}}) = \sigma_1/\sqrt{N_{\text{hit}}}$ is fitted to the data. The histogram shows the N_{hit} distribution for the signal positrons obtained from the MC simulation

ing of the system and calibration of the change in $O_{\text{inter},k}$. Once the configuration was fixed, the system became stable. The precision of a set of laser calibration with 3000 events is evaluated to be 3 ps from the dispersion. The dispersion remained stable for about two months and then increased slightly, indicating the need to update the calibration.

The track-based method is subject to a position-dependent systematic bias because a small error in the estimation of $f_{1,i}^j$ can accumulate along the e^+ path. Such a position-dependent bias is detected and corrected by comparing the time offsets from the laser method.

The time offsets obtained by the two methods are in good agreement with a standard deviation of 31 ps, which is dominated by the intrinsic uncertainty in the laser method of 27 ps [28]. We adopt the results from the track-based one with the corrections using the laser-based one. The accuracy of the time offset calibration was estimated to be ~ 15 ps, which is negligibly small compared to the single counter time resolution of $\sigma_{t_{e^+},\text{pTC}}(N_{\text{hit}} = 1) \sim 100$ ps as discussed in Sect. 5.5.

5.5 Performance

The single-counter time resolutions were measured to be $\sigma_{t_{e^+},\text{pTC}}(N_{\text{hit}} = 1) \sim 80-100$ ps and $\sigma_{t_{e^+},\text{pTC}}(N_{\text{hit}} = 1) \sim 100-120$ ps for $H = 40$ and 50 mm counters, respectively. The ranges show the variations among the counters and the

resolutions are correlated with the light yield of the counters (the product of the yield of the scintillator and the photon detection efficiency of the SiPMs). The resolutions are on average 11% worse than those obtained in the engineering run in 2017 [25]. This is due to several reasons: a lower sampling frequency (from 2.0 GSPS to 1.4 GSPS), increase in the dark count rates due to the radiation damage to the SiPMs, and lower light yields due to the scintillator ageing and the detachment of SiPMs from the scintillator on some counters.

The multi-hit time resolution is evaluated with the "even–odd" method, in which t_{e^+}, pTC of Eq. (7) is reconstructed independently from two groups of hits in a cluster ($i \in \{2k\}$ and $i \in \{2k + 1\}$ where k is an integer), and the two results are compared. Figure 28 shows the results as a function of N_{hit}, reaching an average time resolution of $\sigma_{t_{e^+},\text{pTC}} = 43$ ps, obtained by weighting the multi-hit resolutions with N_{hit} distribution from the MC simulation. This improves the previous MEG timing counter resolution by almost a factor of two [30].

The efficiency of pTC was studied with a MC simulation. Considering the spread of the muon decay points on the target, the geometrical acceptance is 95% for the signal e^+ with the accompanying γ-ray in the fiducial volume of the LXe detector. A few percent of e^+s escape from hitting pTC due to multiple Coulomb scattering on the CDCH material, especially the end caps. The total detection efficiency is $\varepsilon_{e^+,\text{pTC}} = 91(2)\%$.
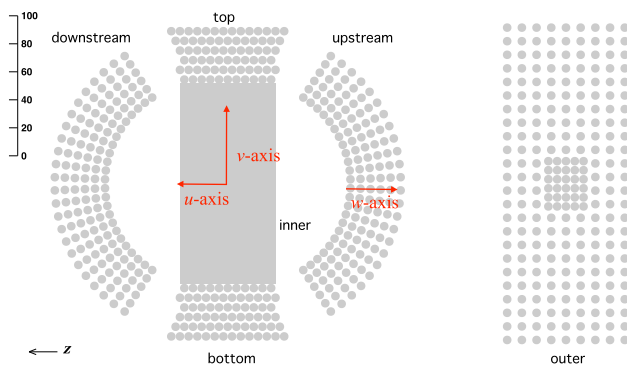
6 LXe detector

To measure the energy, position, and timing of the 52.83 MeV γ-rays from the $\mu^+ \to e^+\gamma$ decay, 900 L LXe is used. LXe has many excellent properties such as high light yield, fast response, high stopping power and good uniformity, and is therefore used in various fields such as particle physics, nuclear physics, and medicine. The LXe detector concept is briefly summarised in Sect. 6.1, and the commissioning of the detector and the initial operation are presented in Sect. 6.2. After the methods used to calibrate the photosensors are described in Sect. 6.3, the current performance of the detector is discussed in Sects. 6.4–6.7.

6.1 Detector concept

The MEG LXe detector has been upgraded to improve the energy and position resolutions for events where the γ-rays interact close to the inner face of the detector. The most important improvement is the change in the granularity of the photosensors on the inner face from 216 2-inch round-shaped PMTs to 4092 (15×15) mm^2 Multi-Pixel Photon Counters (MPPCs) operating at the LXe temperature (~ 165 K) to detect the scintillation light emitted isotropically from LXe in the VUV range ($\lambda \sim 175$ nm). The other faces of the detector are equipped with 668 PMTs which were also used in the MEG experiment. The detailed concept of the MEG II LXe detector is summarised in [3].

The local coordinate system (u, v, w) for the LXe detector is defined as follows: u coincides with z in the cylindrical coordinate system; v is directed along the negative ϕ-direction at the radius of the inner face of the LXe detector ($r_{\mathrm{in}} = 67.85$ cm), which is the direction along the inner face from bottom to top; $w = r - r_{\mathrm{in}}$, measures the depth from the inner face, as shown in Fig. 29.


Fig. 29 Net drawing of the LXe detector and the local coordinate system

6.2 Commissioning and operation

The upgrade of the LXe detector began in 2016 and was completed in 2017, after which it was installed at the experimental site as shown in Fig. 30. After the photosensors were calibrated, commissioning of the detector with the muon beam was started. From 2017 to 2020, the number of available channels of readout electronics was limited, and full readout has been available since 2021.

Some MPPC channels failed due to short circuits or open circuits in the detector, and some PMTs due to the failure of HV modules in operation since the MEG experiment; there are 47 dead channels in the MPPCs and 34 dead channels in the PMTs during the 2022 beam time. The number of scintillation photons missing due to these channels is estimated from the solid angle subtended by the corresponding photosensors and the number of photons detected in the surround-
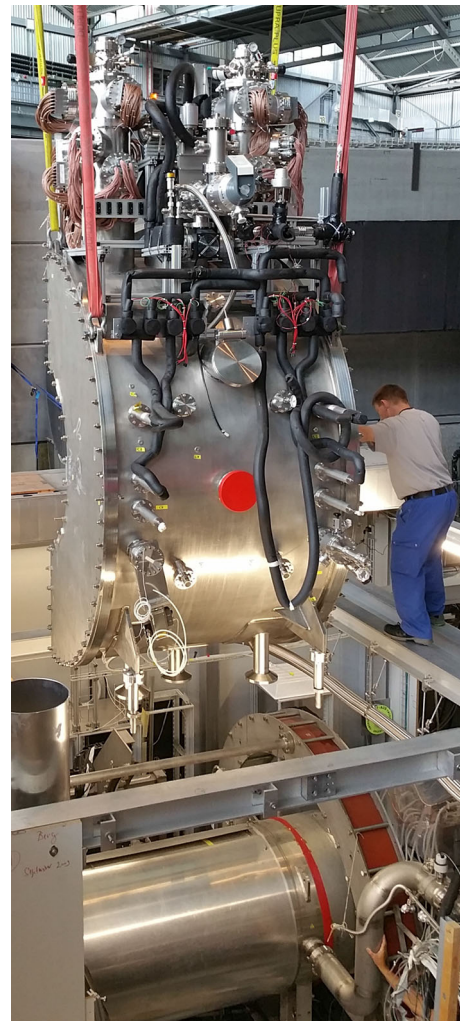
Fig. 30 The LXe detector installed into the experimental site

ing channels and is taken into account in the reconstruction algorithms to compensate for the effect of the dead channels.

Purification of xenon is necessary to achieve a good light yield from the scintillation. Purification in the liquid phase is performed each year before the beam time by circulating the liquid xenon through a molecular sieve. This method cannot be used during the physics runs because of the noise of the circulation pump. Purification in the gaseous phase is additionally performed during the whole beam time with a hot metal getter. The molecular sieve is expected to remove impurities, especially water, and the getter is expected to remove water, oxygen, and nitrogen.

Various types of calibration data, presented in Sects. 6.3 and 6.6.4, are collected at regular intervals during the physics run to study the stability and uniformity of the detector response. A detailed description of the calibration equipment can be found in [1]. The entire set of calibration data is collected thrice a week, while a smaller subset for the calibration of the photosensors is collected once a day. The dead time in the physics run due to calibration was $7-8\%$ in 2021 and was reduced to less than 5% in 2022 by optimising the calibration scheme.

Detailed studies of energy and time resolutions have been performed with quasi-monochromatic 55 and 83 MeV γ-rays produced by the π^-p charge exchange (CEX) reaction (π^-p $\rightarrow \pi^0$n, $\pi^0 \rightarrow 2\gamma$) since 2020. Since this calibration requires a π^- beam, a liquid hydrogen (LH$_2$) target in the COBRA centre, and an additional γ-ray detector (BGO calorimeter) to tag back-to-back γ-rays (see [1] for details), frequent calibration with this method is unrealistic. Therefore, a period of two to three weeks is reserved once a year for CEX data acquisition.

The photon detection efficiency (PDE) of the MPPCs for VUV light was measured 0.13 ± 0.01 on average in the 2017 commissioning run. This value is significantly lower than the value of 0.20 ± 0.02 measured with two MPPC samples in the laboratory [31]. Surface damage to MPPCs caused by the muon beam was identified as a possible cause for the lower PDE. A detailed investigation was carried out in 2019, that demonstrated that the decrease of PDE as a function of muon beam time was due to radiation damage [32].

Annealing turned out to restore the reduced PDEs effectively. Annealing of all MPPCs in the detector was performed for the first time during the accelerator shutdown period between runs 2021 and 2022. The Joule heating of the MPPCs itself served as the heat source. A custom-built constant-voltage power supply with 30 ports capable of supplying 60 to 80 V and up to 250 mA per port was used. Eight MPPCs were connected to each port and 240 MPPCs were biased simultaneously. The MPPCs were illuminated with LED light to induce a current. A reverse bias voltage of 71 V was applied to each MPPC with a typical current of 25 mA, resulting in a power dissipation of 1.775 W. Each MPPC was

annealed for ~ 28 h. PDEs high enough to tolerate radiation damage during the physics run for a full year were achieved as described in Sect. 6.3.4. This procedure (annealing during the shutdown period and continuous physics data taking during the beam period) has been and will be repeated every year during the MEG II physics run.

6.3 Sensor calibration

The kinematics of the incident γ-ray is reconstructed from the charges and timings of the signals caused by the LXe scintillation light detected by the photosensors. The charge Q_i (i is the index of the photosensor) is measured by integrating the pulse of the digital waveforms in a 150 ns wide window and converting it to the number of photo-electrons $N_{\text{phe},i}$ and then to the number of photons incident on the photosensor $N_{\text{pho},i}$, as follows:

$$
N_{\text{phe},i} = Q_i / \left(e \cdot G_i \cdot F_{\text{EC},i} \right),
$$
$$
N_{\text{pho},i} = N_{\text{phe},i} / \mathcal{E}_i,
\tag{12}
$$

where e is the elementary charge, G_i is the gain of the photosensor, $F_{\text{EC},i}$ is the excess charge factor (ECF), and $\mathcal{E}_i$ is the quantum efficiency (QE) of PMT or the PDE of MPPC. The ECF for MPPC is the ratio between the measured charge and the charge due to the primary photoelectrons, and it is larger than 1 because of cross-talk and after-pulse; for PMTs $F_{\text{EC},i} = 1$ is assumed. The results of the calibration for these parameters are described here mainly for 2021 data. The calibration of the timing parameters is described in Sect. 6.5.

6.3.1 Noise reduction

The waveform for each channel is read out by the Wave-DREAM board and digitised at 1.4 GSPS by the Domino Ring Sampler (DRS4) chip mounted on the board, as described in Sect. 8. Calibration and noise reduction are applied to the digitised waveform data by subtracting the following four types of noise templates, created from pedestal events acquired with periodically output triggers.

The first noise template is dedicated to correct the voltage offset of each sampling capacitor cell in the DRS4 chip. Voltage calibration is first performed in the online analysis (see Sect. 8.3), but some offsets that cause a low-frequency noise remain and must be removed. The remaining voltage offset, corresponding to each physical capacitor cell, is extracted by averaging the voltage for each cell for pedestal events. The second is used to compensate for high-frequency noise caused by the cross-talk of a clock signal distributed to the WaveDREAM boards for time synchronisation. Since it is synchronous with the clock signal, it can be extracted by averaging the pedestal waveforms after adjusting the timing
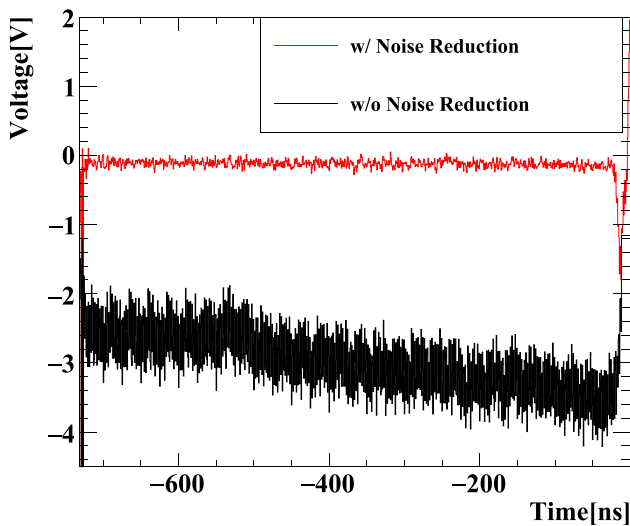
Fig. 31 The sum waveforms of all MPPCs. The black and red ones are before and after noise reduction, respectively [33]

Fig. 32 The correlation between the mean and the variance of the PMT charge at different LED intensities. The gain is calculated from the slope of the linear fit
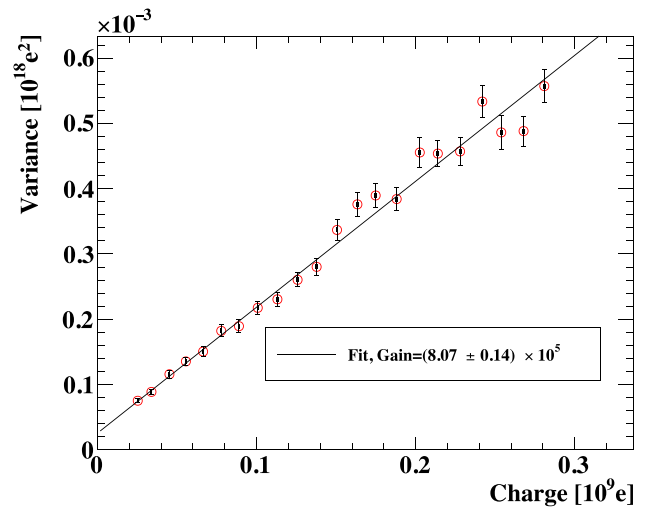
to the clock phase. The third is to correct the temperature dependence of the slope of the baseline. Each capacitor cell has a small leakage current that depends on the temperature and results in a slope of the baseline. The relation between the temperature and the slope for each channel is extracted from the pedestal events acquired at different temperatures. The fourth is to subtract the noise correlated with the sampling cell corresponding to the first point of the waveform data in the time order. The sampling process of DRS4 is running continuously and cyclically, and when a trigger signal comes it stops sampling and starts readout from the stopped cell. Therefore, the physical cell corresponding to the first point in the waveform changes for each event and the readout time of each cell also changes. It causes a variation of the voltage offset. This effect is reduced by creating noise templates depending on the first sampling cell.

Figure 31 shows the waveforms summed for all MPPC channels before and after noise reduction. The offset is corrected, and the slope and high-frequency noise are reduced. The dispersion of the reconstructed energy of pedestal events is reduced to $\sigma_{\text{noise,LXe}} = 0.15\,\text{MeV}$, which is sufficiently small compared to the energy resolution of the LXe detector (Sect. 6.6).
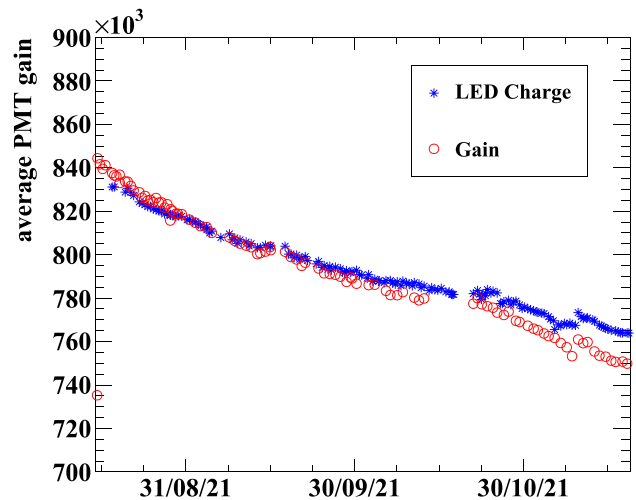
6.3.2 PMT gain

The absolute gain in each PMT is determined from the correlation between the mean $\overline{Q}_i$ and the variance $\sigma_{Q_i}^2$ of the charge for a constant light source:

$$\sigma_{Q_i}^2 = G_i \cdot e \cdot \overline{Q}_i + \sigma_{\text{noise},i}^2, \tag{13}$$

Fig. 33 Temporal evolution of the average gain of all PMTs during the 2021 run. The red plot shows the average of the absolute gains and the blue one shows the average of the mean charges for constant LED intensity scaled to the gain values with the data on 15th September

where $\sigma_{\text{noise},i}$ is a noise term. This correlation is measured by flashing the blue LEDs installed in the LXe detector at 22 different intensities. The gain is determined by fitting Eq. (13) as shown in Fig. 32.

The gains of all PMTs were set to $\sim 0.8 \times 10^6$ at the beginning of each run with 3% accuracy by adjusting HV for each PMT. The average gain decreased continuously during the run as shown in Fig. 33. This phenomenon was already observed in the MEG experiment. While a single set of HVs was used throughout the 2021 run, the HVs were readjusted twice during the 2022 run to restore the reduced gains when the average gain decreased by $10-20\%$.

The temporal evolution is traced by the absolute gain measurements. Their fluctuation is smoothed periodically in the offline reconstruction using the mean charge for fixed intensity LED events, as the accuracy of the charge measurement (statistical uncertainty $< 0.1\%$) is higher than that of the determination of the absolute gain. The discrepancy between the temporal evolution of the two measurements (red and blue points in Fig. 33), that does not introduce a significant uncertainty, could be due to the change in the transmittance of the LED light ($\lambda \sim 460$ nm) in LXe or to the LED light instability, which only affect the measurement of the mean charge. The former contribution is likely dominant because a correlation is observed between this discrepancy and the change in the light yield of the VUV scintillation light, sensitive to the purity of the LXe, which improves over time due to continued purification in the gaseous phase.

6.3.3 MPPC gains and ECFs

MPPC gains and ECFs are calibrated using low-intensity LED data. The intensity of the LEDs is adjusted for the MPPCs nearest to each LED to detect one photo-electron on average. The gain is obtained from the distance between two peaks corresponding to zero and one photo-electron. However, it is difficult to separate the two peaks with the standard integration range of 150 ns in presence of noise. Therefore the gains and the ECFs are extrapolated from the results with several shorter integration ranges.

The ECF is measured as follows:

$$F_{\mathrm{EC},i} = \overline{Q}_i / \left(e \cdot G_i \cdot \langle N_{\mathrm{phe},i} \rangle \right), \tag{14}$$
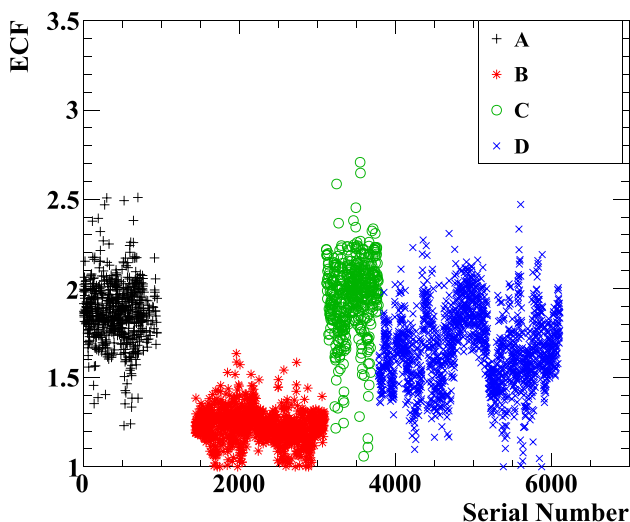
Fig. 34 The ECFs of the MPPCs versus the serial number [33]. Different markers show MPPCs produced in different production lots

where $\langle N_{\mathrm{phe},i} \rangle$ is the expected number of photo-electrons for the LED that can be calculated from the number of zero photo-electron events $n_{\mathrm{zero},i}$ and the total number of events $n_{\mathrm{total},i}$ as

$$\langle N_{\mathrm{phe},i} \rangle = - \log \left(n_{\mathrm{zero},i} / n_{\mathrm{total},i} \right). \tag{15}$$

Figure 34 shows the ECFs as a function of the serial number of the MPPCs. The MPPCs were manufactured in four different periods, each labelled with different markers. A dependence of the ECFs on the production lot was found. This dependence is still acceptable as it can be measured and corrected.

The uncertainty of the absolute gain measurement is 2.5% from statistics and that of the ECF is $1-5\%$, which mainly comes from the statistical uncertainty of $\langle N_{\mathrm{phe},i} \rangle$.

6.3.4 PDEs of MPPCs and QEs of PMTs

The MPPC PDEs and the PMT QEs for VUV light are calibrated with α-particles from ^{241}Am sources deposited on thin wires mounted inside the active volume of the detector. Since the positions of the α-particle sources are known, the expected number of photons arriving at each photosensor can be estimated with a MC simulation. Therefore, the PDEs and QEs are calculated by comparing the mean number of measured photo-electrons $\overline{N}_{\mathrm{phe},i}$ with the number $\overline{N}^{\mathrm{MC}}_{\mathrm{phe},i}$ in the MC simulation as follows:

$$\mathcal{E}_i = \mathcal{E}^{\mathrm{MC}}_i \times \frac{\overline{N}_{\mathrm{phe},i}}{\overline{N}^{\mathrm{MC}}_{\mathrm{phe},i}} \times F_{\mathrm{LY}}, \tag{16}$$

where $\mathcal{E}^{\mathrm{MC}}_i$ is the PDE (QE) assumed in the MC simulation, and F_{LY} is a light yield correction factor common to all photosensors so that $F_{\mathrm{LY}} = 1$ corresponds to the fact that the mean value of the PMT QEs is 0.16. This is the value on the sheet supplied by Hamamatsu Photonics K.K. and is the same condition as in the MC simulation.

Since the main background source in the calculation of PDE (QE) is cosmic rays, α-particle events are separated from cosmic ray events by using a pulse shape discrimination technique that distinguishes highly ionising particles (whose waveform has a shorter time component) from minimum ionising particles (whose waveform has a longer time component) based on the relation between the charge and the amplitude of all PMTs.

The systematic uncertainty in the absolute value of the PDEs (QEs) estimated with this method is 10%; the main contributions are the uncertainty in the scintillation light yield for α-particles (5%) and the uncertainty in the MC simulation for the effect of reflection at the inner surface of the detector (5%) [32].
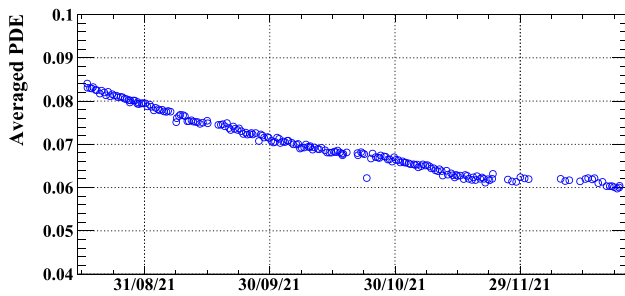
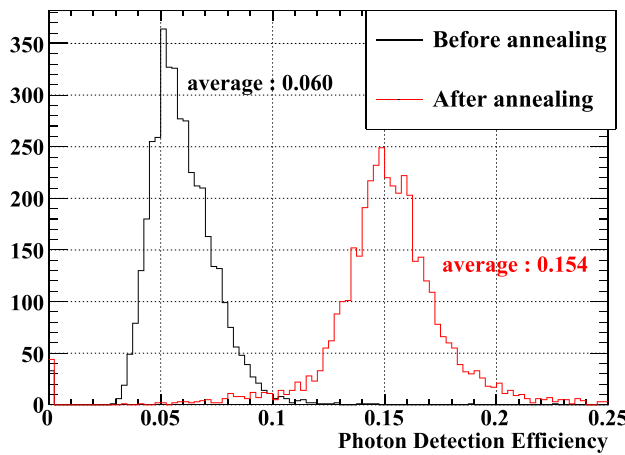**Fig. 35** Temporal evolution of the average PDE of all MPPCs

Fig. 36 Distribution of MPPC PDEs before and after the annealing in 2022

Figure 35 shows the temporal evolution of the average PDE of all MPPCs. The average PDE decreased from 0.082 to 0.060 in the 2021 run due to radiation damage. As explained in Sect. 6.2, full channel annealing was carried out after the beam time in 2021. The average PDE was increased to 0.154 by the annealing as shown in Fig. 36.

6.4 Position reconstruction and resolution

The first conversion position of the incident γ-ray in the LXe detector $\vec{x}_{\gamma,\mathrm{LXe}}$ is reconstructed from the light distribution viewed by the MPPCs. The following χ^2_{pos} is minimised:

$$\chi^2_{\mathrm{pos}}\left(\vec{x}_{\gamma,\mathrm{LXe}}\right) = \sum_{i\in\mathrm{region}}\left[\frac{N_{\mathrm{pho},i} - C \times \Omega_i\left(\vec{x}_{\gamma,\mathrm{LXe}}\right)}{\sigma_{\mathrm{pho},i}}\right]^2,$$
(17)

$$\sigma_{\mathrm{pho},i} = N_{\mathrm{pho},i}/\sqrt{N_{\mathrm{phe},i}},$$
(18)

where $\Omega_i(\vec{x}_{\gamma,\mathrm{LXe}})$ is the solid angle at position $\vec{x}_{\gamma,\mathrm{LXe}}$ subtended by the MPPC, C is a floating parameter of the fit to convert the solid angle to the number of photons, and $\sigma_{\mathrm{pho},i}$ is the uncertainty of $N_{\mathrm{pho},i}$ for each MPPC defined in Eq. (18).

The MPPCs in a circular region around the peak position in the light distribution are used for the fit.

This fit is based on the assumption that the number of photons detected by each MPPC is proportional to the solid angle at the interaction point subtended by the MPPC. In reality, the source of the scintillation photons has a finite size because an electromagnetic shower forms in a direction that correlates with the direction of the incident γ-ray. Therefore, the result of the fitting, $\vec{x}_{\gamma,\mathrm{fit}} = (u_{\gamma,\mathrm{fit}}, v_{\gamma,\mathrm{fit}}, w_{\gamma,\mathrm{fit}})$, is biassed in the direction of the shower evolution. To account for this effect, two corrections are made based on the MC simulation studies. The first is a correction depending on u_{fit}. The position is reconstructed further outward when the incident angle is large (large $|u|$), and, therefore, a larger correction is required. The second is a correction for the event-by-event fluctuation toward the shower evolution which can be estimated from the difference of $\vec{x}_{\mathrm{fit}}$ reconstructed with different radii of the circular region.

A systematic error in position reconstruction results from errors in MPPC positions. To take full advantage of the improved granularity of the readout, we measured the MPPCs' positions using two complementary methods. The first is a direct optical survey using a 3D laser scanner, which was carried out at room temperature during the construction phase. The second is a measurement with a well-aligned collimated X-ray beam, which was carried out after the detector had been installed on site and filled with LXe. The latter is necessary because thermal contraction and deformation during LXe filling affect the sensor positions. The methods and results are described in detail in [34]. The uncertainty of the first method is ~ 0.1 mm. The largest uncertainty results from the reproducibility in the second method. It was checked by moving and repositioning the LXe detector and the γ-ray beam and by repeating the optical survey. It resulted to be 0.57 mm in z. The total uncertainties were reduced to below 0.6 mm in z and 0.7 mrad in ϕ, which are sufficiently small compared to the position resolution described below. The global position of the detector is also aligned with the cosmic ray events passing through both the LXe detector and the CDCH, as described in Sect. 4.5.4.

The position resolutions are evaluated by imaging a lead collimator with γ-rays from the $^7\mathrm{Li}(\mathrm{p},\gamma)^8\mathrm{Be}$ reaction produced by a proton beam accelerated by a Cockcroft–Walton (CW) accelerator [35]. A $(240 \times 240 \times 25)$ mm^3 collimator with eight slits, each 5 mm wide and 80 mm long with 50 mm spacing between the slits, was installed between the detector and the COBRA magnet in a dedicated run. Figure 37 shows the two-dimensional position distribution of the γ-rays that passed through the collimator. The sharpness of the reconstructed slit images represents the v resolution. The u-resolution is measured by rotating the collimator by $90°$. The resolutions are estimated by fitting the MC simulation model, which was smeared by the resolution, to the
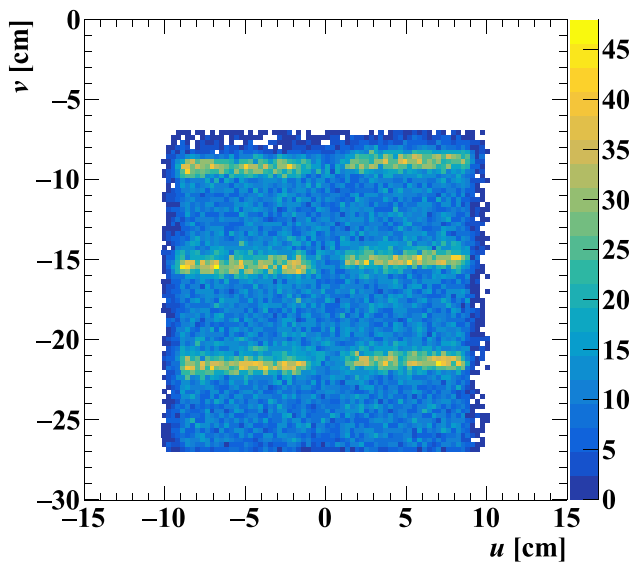
Fig. 37 The position distribution of ^{7}Li$(p, \gamma)^8$Be line events in u–v plane with the collimator for the v-resolution measurement. The readout region covers six out of eight slits, which are imaged as horizontal lines

Fig. 38 The time difference between the reconstructed γ-ray timing in LXe detector and that on the pre-shower counter for $E_\gamma = 55$ MeV fitted with a double Gaussian function

data, resulting in $\sigma_{u_\gamma, v_\gamma} = 2.5$ mm (4.0 mm) for $w < 2$ cm (> 2 cm) in u and v. The position resolution in w is estimated to be $\sigma_{w_\gamma} = 5.0$ mm based on the MC simulation.
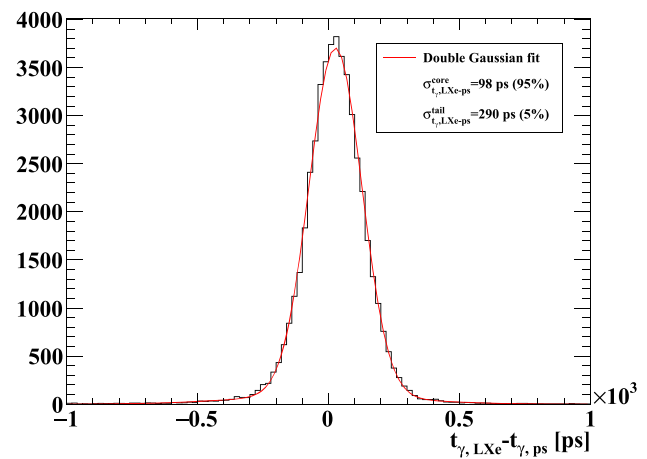
6.5 Time reconstruction and resolution

The time of the γ-ray first interaction with LXe is reconstructed by minimising the following chi-square function:

$$\chi^2(t_{\gamma,\mathrm{LXe}})$$
$$= \sum_i \left(\frac{t_{\mathrm{pm},i} - t_{\mathrm{prop},i} - t_{\mathrm{walk},i} - t_{\mathrm{offset},i} - t_{\gamma,\mathrm{LXe}}}{\sigma_{\mathrm{pm},i}} \right)^2,$$
(19)

where $t_{\mathrm{pm},i}$ is a time detected at each sensor calculated from the waveform data using a constant fraction method to mitigate the time walk effect; $t_{\mathrm{prop},i}$ is the travel time of the scintillation light from the reconstructed first interaction point to each sensor; $t_{\mathrm{walk},i}$ is the effect of the remaining time walk, and $t_{\mathrm{offset},i}$ is the time offset of each sensor. Photosensors that have detected $N_{\mathrm{phe},i} > 50$ are used in the fit.

The two γ-rays from π^0 decay are used to calibrate $t_{\mathrm{walk},i}$ and $t_{\mathrm{offset},i}$ and evaluate the time resolution. A pre-shower counter, consisting of a 4 mm thick lead converter and two plastic plates read out by MPPCs from both ends, was installed in the CEX run on the opposite side of the LXe detector across the LH$_2$ target to measure time with high precision. The pre-shower counter detects one of the two γ-rays and the detection time $t_{\gamma,\mathrm{ps}}$ is used as a reference for the hit time of the other γ-ray in the LXe detector. The

parameter $t_{\mathrm{walk},i}$ is obtained as a function of $N_{\mathrm{phe},i}$ for the remaining time from the reference time, and a common function is used for photosensors on the same face of the detector, while $t_{\mathrm{offset},i}$ is obtained for each channel as a constant offset remaining after the $t_{\mathrm{walk},i}$ correction.

Since the position of the π^0 decay vertex is unknown, the spread σ_{vertex} contributes to the dispersion of the time difference of the two γ-rays. The time dispersion due to σ_{vertex} was measured with two plastic counters, a pre-shower counter and another counter of identical structure placed in front of the LXe detector in a dedicated CEX run.

Figure 38 shows the distribution of $t_{\gamma,\mathrm{LXe\text{-}ps}} = t_{\gamma,\mathrm{LXe}} - t_{\gamma,\mathrm{ps}}$ with the times at the centre of the vertex distribution converted and corrected for their times of flight. A double Gaussian function was fitted to the distribution, resulting in $\sigma^{\mathrm{core}}_{t_{\gamma,\mathrm{LXe\text{-}ps}}} = 98$ ps in the core part (95%) and $\sigma^{\mathrm{tail}}_{t_{\gamma,\mathrm{LXe\text{-}ps}}} = 290$ ps in the tail part (5%). The time resolution of the pre-shower counter was assessed by the difference between the time of the incident γ-ray reconstructed by each plate: $\sigma_{t_{\gamma,\mathrm{ps}}} = 28.2 \pm 0.2$ ps. The time dispersion due to σ_{vertex} is $\sigma_{t_\gamma,\mathrm{vertex}} = 68 \pm 6$ ps. Finally, the time resolution of the LXe detector is $\sigma_{t_{\gamma,\mathrm{LXe}}} = 65 \pm 6$ ps at $E_\gamma = 55$ MeV. The large uncertainty in $\sigma_{t_{\gamma,\mathrm{LXe}}}$ results from the large statistical uncertainty in $\sigma_{t_\gamma,\mathrm{vertex}}$, due to the instability of the LH$_2$ target in the 2021 CEX run.

6.6 Energy reconstruction and resolution

The energy of the incident γ-ray, E_γ, is reconstructed by adding the number of scintillation photons collected by each photosensor $N_{\mathrm{pho},i}$ and scaling it as

$$E_\gamma = S \times T(t) \times F(u, v, w) \times N_{\mathrm{sum}},$$
(20)
$$N_{\mathrm{sum}} = N_{\mathrm{MPPC}} \times k(t) + N_{\mathrm{PMT}},$$
(21)

$$N_{\text{MPPC(PMT)}} = \sum_{i \in \text{MPPC(PMT)}} w_i(u, v) \times N_{\text{pho},i}, \qquad (22)$$

where S is the scaling factor of N_{sum} to the energy, $T(t)$ and $k(t)$ are correction functions for the temporal evolution described in Sect. 6.6.1, $F(u, v, w)$ is a function to correct for position dependence described in Sect. 6.6.2, and $w_i(u, v)$ is a weight for each photosensor. The weight $w_i(u, v)$ is a product of the photosensor coverage, the dead channel compensation factor (see Sect. 6.2), and the light collection efficiency factor as a function of the reconstructed γ-ray position (u, v) and the face of the detector.

Pile-up of low-energy γ-rays from μ^+ decays affect the energy reconstruction. To mitigate this effect, pile-up identification and unfolding algorithms are applied as described in Sect. 6.7.

6.6.1 Time dependence

The stability of the detector is monitored with the $^7\text{Li}(p, \gamma)^8\text{Be}$ reaction (17.6 MeV line), α-particles and cosmic rays. Figure 39a and b show typical energy spectra for the $^7\text{Li}(p, \gamma)^8\text{Be}$ reaction and cosmic rays, respectively. The $^7\text{Li}(p, \gamma)^8\text{Be}$ spectrum shows a clear peak at 17.6 MeV and a secondary peak at ~ 14 MeV as expected [36]. For the cosmic ray spectrum, event selection based on the reconstructed position and the ratio of N_{MPPC} to the number of photons detected on the outer faces is applied. After the selection, the distribution of energy release follows a Landau distribution with a broad peak at ~ 170 MeV.

The temporal evolution of the normalised numbers of detected photons on the MPPC and PMT surfaces for these data are shown in Fig. 39c–d. They show common trends for all calibration sources, but different trends were observed between MPPCs and PMTs. This difference results from the LXe purity and the different distances to the α-particle sources used in the calculation of PDE (QE). The cosmic ray data are used to correct for the difference as the time-dependent weights of MPPCs and PMTs $k(t)$ in Eq. (21).

The temporal variation can also be evaluated using the energy spectrum of the background γ-rays, with an endpoint energy of 52.83 MeV, measured during the physics run (see also Sect. 6.7). Figure 39e shows the temporal evolution of the normalised N_{sum} for the cosmic rays and the background γ-rays. A function $T(t)$ to correct for this time dependence of N_{sum} is constructed using cosmic rays for a finer structure of temporal evolution and background γ-rays for a coarser structure. The estimated accuracy of the temporal evolution correction is 0.3% from the residual variations of the scales for the background γ-rays.
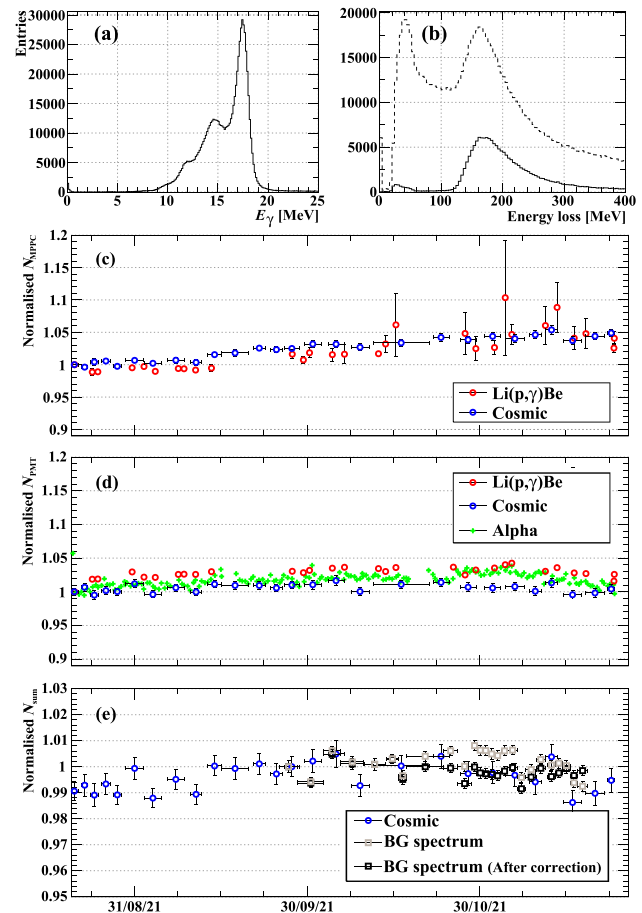

Fig. 39 **a** Energy spectrum of the $^7\text{Li}(p, \gamma)^8\text{Be}$ line. **b** Energy spectrum of the cosmic ray data. The dotted line shows the raw spectrum while the solid line shows the spectrum after the cosmic ray event selection. **c** and **d** Temporal variation of the light yield for each calibration source during 2021 run measured by MPPCs and PMTs, respectively. The data are normalised to 1 at the beginning of the beam time. **e** Temporal variation of N_{sum}. The data are normalised at 1 at the beginning of physics run

6.6.2 Position dependence

A non-uniform response of the energy scale is visible in Fig. 40. A three-dimensional correction function $F(u, v, w)$ was created using the 55 MeV γ-rays of $\pi^0 \rightarrow \gamma\gamma$ decays, the $^7\text{Li}(p, \gamma)^8\text{Be}$ 17.6 MeV line and the background γ-rays to smooth the response.

The physics run in 2021 was divided into five periods based on the intensity of the muon beam, and $F(u, v, w)$ was calculated for each period. The period-dependent $F(u, v, w)$ can not only complement the correction for the temporal evolution due to the change in LXe purity but also contribute to the stability of the energy resolution.

The accuracy of the non-uniformity correction is estimated to be 0.2% by mean of the uncertainty of the three-dimensional correction factors.
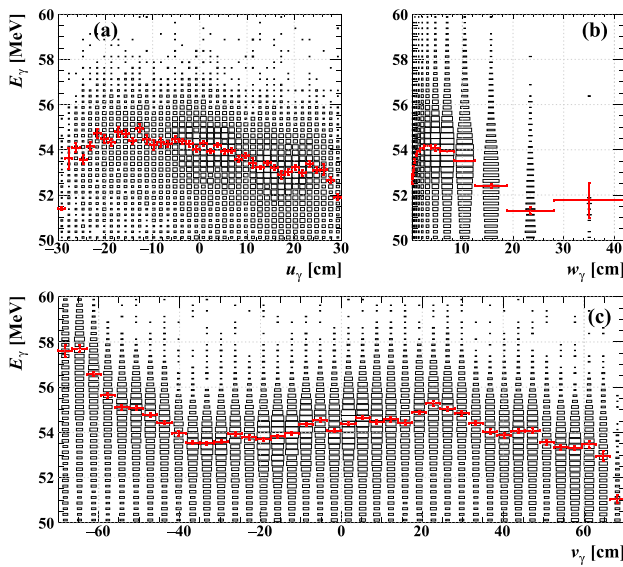
Fig. 40 Position dependence of the reconstructed 55 MeV γ-rays from $\pi^0 \to \gamma\gamma$ decays. The red points are the peak energy in slices projected along u_γ, v_γ, or w_γ

Fig. 41 Energy response to 55 MeV γ-rays hitting a central area of the detector ($u \in [-10\,\mathrm{cm}, 10\,\mathrm{cm}] \wedge v \in [-30\,\mathrm{cm}, -10\,\mathrm{cm}]$) in different w ranges. The fitting function of Eq. (23) is shown in red
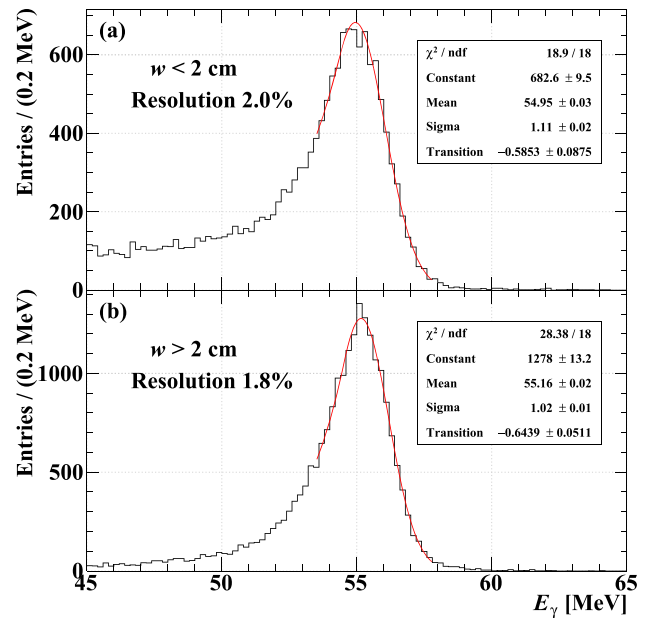
6.6.3 Energy scale

The scale factor S is determined from the peak of the N_{sum} distribution for the 55 MeV γ-rays and the energy scale of the background γ-rays. The uncertainty for the E_γ energy scale in 2021 is 0.4%, Table 3 reports the breakdown in separate contributions.

6.6.4 Energy resolution

The energy response was investigated with the quasi-monochromatic 55 MeV γ-rays. Figure 41 shows the energy response in a central part of the detector in different w regions. Asymmetric spectra were observed mainly at $w < 2$ cm; the low-energy tail originates from γ-rays interacting in front of the detector fiducial volume and shower leaks from the incident face. The energy resolution is evaluated by

Table 3 Breakdown of the energy scale uncertainty in 2021

Element	Uncertainty (%)
Temporal evolution	0.3
Position dependence	0.2
Non-linearity between 55 MeV and 52.83 MeV	0.1
Total	0.4

fitting the following function to the data:

$$f(x) = \begin{cases} A\exp\left[-\dfrac{\left(x-\mu_{E_\gamma}\right)^2}{2\sigma_{E_\gamma}^2}\right] & (\text{if } x > \mu_{E_\gamma} + \tau), \\ A\exp\left[\dfrac{\tau\left(\tau/2 - x + \mu_{E_\gamma}\right)}{\sigma_{E_\gamma}^2}\right] & (\text{if } x \leq \mu_{E_\gamma} + \tau), \end{cases}$$
(23)

where $A, \mu_{E_\gamma}, \sigma_{E_\gamma}$, and τ are the constant, mean, sigma, and transition parameters in Fig. 41, respectively. The relative energy resolution is equal to $\sigma_{E_\gamma}/\mu_{E_\gamma} = 2.0\%$ (1.8%) for $w < 2$ cm ($w > 2$ cm).

The expected relative energy resolution for MEG II was estimated to be $1.0-1.7\%$ based on the difference between the measured and simulated values in MEG [3] as the reason for the difference was not fully understood. The obtained resolution of 1.8% for $w > 2$ cm corresponds to the worst case where the difference is completely preserved. The reason for this is not entirely clear, but one of the possible causes is the optical properties of LXe, as discussed in [3], as the difference was observed in both MEG and MEG II experiments. The hypothesis that the cause of this difference is due to the PMT behaviour is ruled out since it remains despite the change from PMTs to MPPCs on the front face in MEG II.

6.7 Background rejection and efficiency

Pile-up γ-rays at high beam intensities increase the background events near the signal energy. Therefore, a dedicated analysis is applied to reduce this contamination. Pile-up events can be identified from the light distribution in the MPPCs. If the pile-up γ-rays are temporally separated from the main γ-ray, multiple γ-rays are unfolded in the weighted sum waveforms of the MPPCs and PMTs by fitting a superposition of n template pulses, where n is the number of detected γ-rays. If, on the other hand, the pile-up γ-rays are too close in time with the main γ-ray to be unfolded, such events are discarded from the analysis sample. If the reduced chi-square values of the waveform fitting are large ($\chi^2_{\rm PMT}/N_{\rm dof} > 8$ or $\chi^2_{\rm MPPC}/N_{\rm dof} > 20$), such events are also discarded.

The background E_γ spectra with and without this pile-up analysis at $R_\mu = 5 \times 10^7\,{\rm s}^{-1}$ are shown in Fig. 42. The background events with $E_\gamma \in [48\,{\rm MeV}, 58\,{\rm MeV}]$ are reduced by 35% by the pile-up analysis. The reduction around the signal energy is apparent. The analysis efficiency for signal γ-rays after applying this pile-up analysis is estimated to be $(92 \pm 2)\%$ at $R_\mu = 3 \times 10^7\,{\rm s}^{-1}$ using a dedicated MC simulation of signal events with pile-up γ-rays and RMD-enhanced data tagged by the RDC.

The cosmic ray background events in the signal region have different depth distributions and MPPC/PMT charge ratios than the signal events originating from the target. Using this information, events identified as cosmic rays are removed. The inefficiency of the signal events due to this cut is negligible.

The detection efficiency for signal γ-ray is estimated from the MC simulation $\varepsilon_\gamma = 69\%$ [3]. To check and correct this MC estimate, we used the $\pi^0 \rightarrow 2\gamma$ data. Once the BGO calorimeter detects an 83 MeV γ-ray, we know that the other 55 MeV γ-ray is emitted in the opposite direction (namely, towards the LXe detection). Therefore, by counting the events where the LXe detector detects γ-rays in the self-triggered BGO events, we can measure the detection efficiency of the LXe detector at 55 MeV. To account for the different measurement conditions compared to the standard physics run, such as the additional material for the LH$_2$ target system, a dedicated MC simulation was performed for this measurement. The estimated MC efficiency for this setup is $\varepsilon^{\rm MC}_{\gamma,{\rm CEX}} = 64\%$, while the efficiency from the data is $\varepsilon^{\rm data}_{\gamma,{\rm CEX}} = (61 \pm 1)\%$. This discrepancy has not yet been resolved and is accounted for in the systematic uncertainty. The best estimate of the detection efficiency for the signal γ-rays is $\varepsilon_\gamma = (67 \pm 2)\%$.
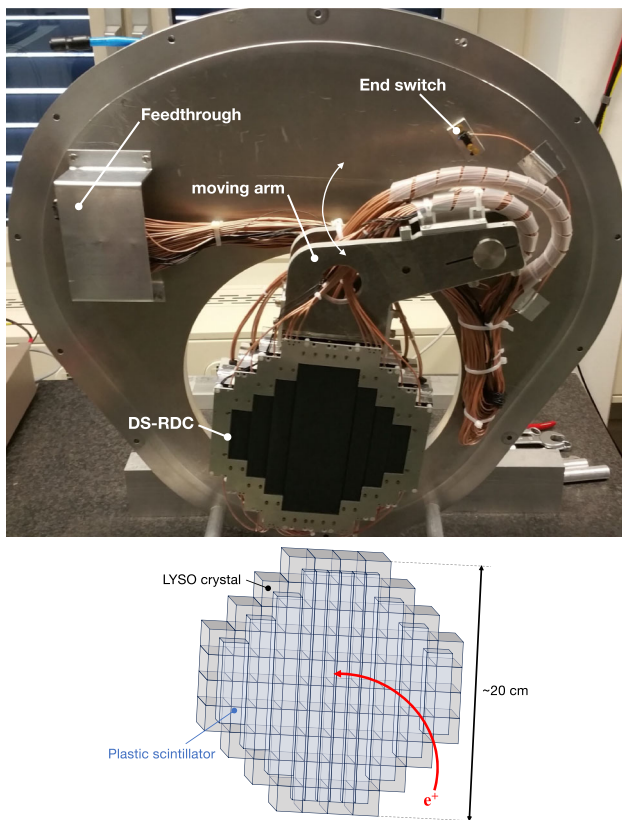
The overall efficiency for signal γ-rays is the product of the detection efficiency and the analysis efficiency $\varepsilon_\gamma = (62 \pm 3)\%$.
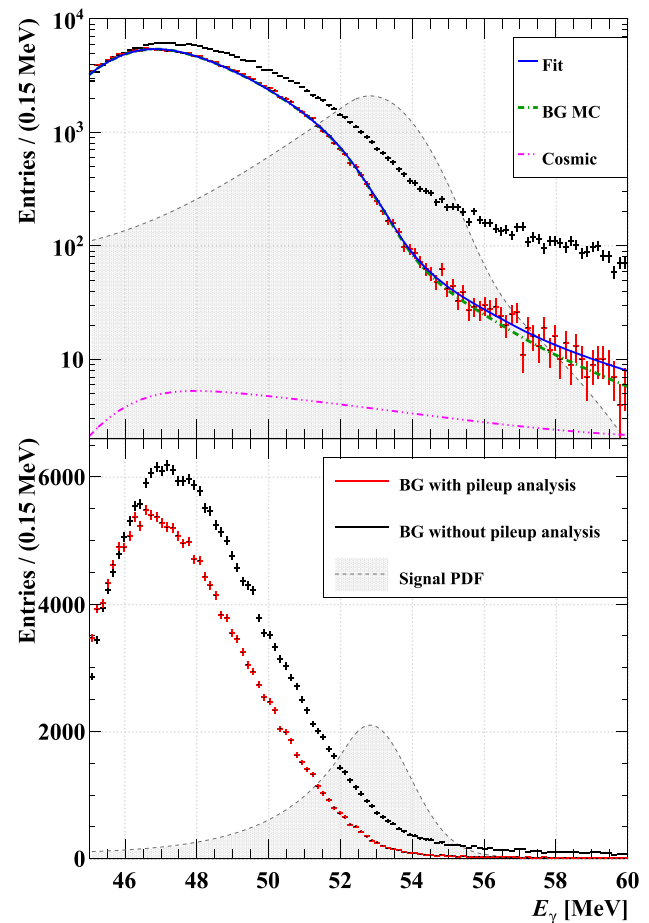
Fig. 42 Background E_γ spectra with (red) and without (black) pile-up analysis at $R_\mu = 5 \times 10^7\,{\rm s}^{-1}$ in log scale (top) and in linear scale (bottom). The drop below ~ 47 MeV is a trigger threshold effect (see Sect. 8.4.1). The blue solid curve in the top panel is the best fit to the spectrum with pile-up analysis, resulting from the sum of the spectrum obtained with a dedicated MC simulation smeared for the worse resolution in the data (green dashed) and the measured cosmic ray spectrum (magenta dashed). The expected spectrum for the signal γ-rays, arbitrarily normalised to 50 000 events in $E_\gamma \in [48\,{\rm MeV}, 58\,{\rm MeV}]$, is also superimposed (grey shaded)

7 Radiative decay counter

One of the main sources of high-energy γ-rays are the RMD ($\mu^+ \rightarrow {\rm e}^+ \nu \bar{\nu} \gamma$) events. If one of these events coincides in time with a high-energy positron from a Michel decay of another muon, it can become an accidental background event. The RDC is a new subdetector introduced in the MEG II experiment to identify such high-energy γ-rays by detecting the low-energy positrons emitted in the same RMD. When an RMD emits a γ-ray with an energy above 48 MeV, the energy of a large fraction ($\sim 66\%$) of the accompanying positrons falls in the 1 to 5 MeV range. The trajectories of these low-energy positrons in the COBRA magnetic field have too small radii to be detected by CDCH or pTC. Therefore, dedicated positron detectors located close to the beam axis are required.
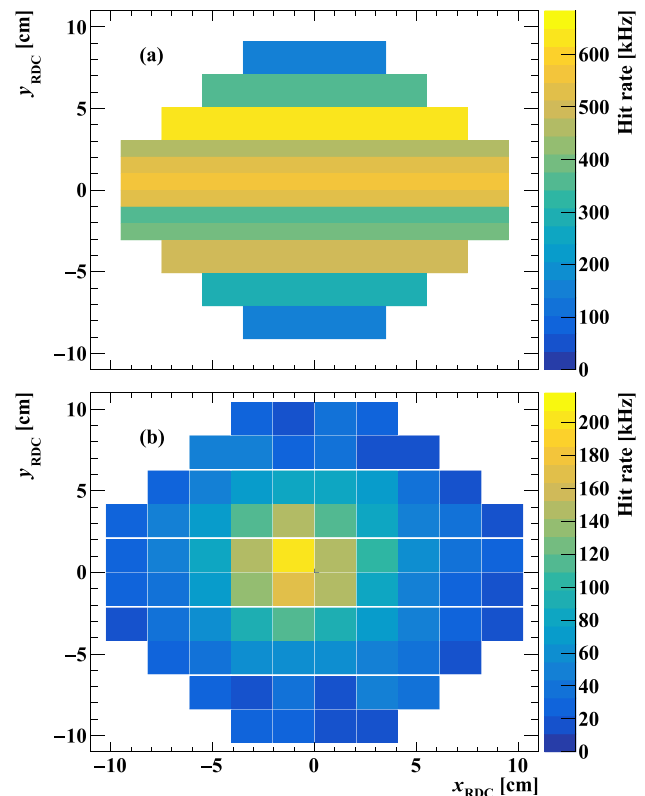
Fig. 43 The downstream RDC

on each side of each bar with optical cement. The other six PS bars located in the outer regions are 2 cm wide with varying lengths; three MPPCs are glued on each side. The MPPCs on the same side of each bar are connected in series and their signals are read out by one channel.

The detector is supported by a movable arm with a pneumatic cylinder so that it can be moved out of the beam axis to insert the beamline for the proton beam from the CW accelerator and the Li target to calibrate the LXe detector. Figure 43 shows the DS-RDC and the moving arm system. The position of the DS-RDC is monitored by physical switches. To avoid collisions with the CW beamline, the two systems are software-locked so that one cannot be deployed while the other is installed.

7.1.1 Operation of the downstream RDC

The DS-RDC is expected to be on the beam axis (measurement position) during the physics run, but this was not always the case as the interlock system was not yet fully functional. In 2021(2022) the DS-RDC was in the measurement position for 74% (89%) of the physics run.

Figure 44 shows the distributions of hit rates of PSs and crystals at $R_\mu = 3 \times 10^7 \, \text{s}^{-1}$ in 2021. As expected,

Time-coincidence measurement can be used to identify the accidental background events with RMD γ-rays, but standard Michel positrons happen to hit accidentally the RDC; they usually have higher energies than RMD positrons. Hence, measurement of positron energy is an additional effective tool to select efficiently the RMD positrons.

In 2017, an RDC was installed at the downstream beamline (Downstream-RDC, DS-RDC). It measures both energy and timing. An additional RDC that measures timing only is currently being developed for installation upstream (Upstream-RDC, US-RDC).

7.1 Downstream RDC

The DS-RDC is located 142 cm downstream of the target on the beam axis. It consists of 76 LYSO crystals for energy measurement, arranged in an octagonal plane, and 12 plastic scintillator bars (PSs) for timing measurement, arranged in front of the crystals in a plane covering the same area. The size of each LYSO crystal is $(2 \times 2 \times 2) \, \text{cm}^3$. Each crystal is covered with a 65 µm thick reflective sheet (ESR, 3M) to increase efficiency of the light collection. One MPPC with pixel size of 25 µm (S125720-25, Hamamatsu Photonics) is attached to each LYSO crystal with a spring. Six 1 cm wide PS bars are used in the central region; two MPPCs are glued

Fig. 44 Hit rate distributions of PSs (**a**) and crystals (**b**) at $R_\mu = 3 \times 10^7 \, \text{s}^{-1}$ in 2021. The axes are the DS-RDC local coordinates defined by a rotation of 83° around the beam axis

the distributions peak near the centre. The shift of the peak from the centre is due to the off-centre beam position on the target shown in Fig. 16. The total hit rates in the DS-RDC are 4.3 MHz, 5.5 MHz, and 6.5 MHz at $R_\mu = 3, 4,$ and $5 \times 10^7 \, \text{s}^{-1}$, respectively. The ratios of the overall hit rates to R_μ are independent of R_μ and are always $0.13-0.14$. Therefore, the DS-RDC serves as a real-time diagnostic tool for the beam using the hit rate and distribution.

The energy deposition in each LYSO crystal is reconstructed as

$$E_{i,\text{LYSO}} = A_i \times Q_{i,\text{LYSO}} \quad (i = 0, 1, \ldots, 75), \tag{24}$$

where $Q_{i,\text{LYSO}}$ is the integrated charge of the LYSO signal for a 250 ns window and A_i is an energy scale factor for each crystal. The factor A_i was calibrated before the start of the physics run using the 597 keV $(88 + 202 + 307 \, \text{keV})$ γ-ray emission following the β-decay of ^{176}Lu, which is naturally present in LYSO crystals (self-luminescence).

Figure 45 shows an example of the charge distribution obtained by self-luminescence. The following function is fitted to the main peak to obtain A_i:

$$\int \mathcal{G}\left(x/A_i - E, E \times \sigma_E + \sigma_{\text{noise}}^2\right) \times \mathcal{D}(E) \, dE, \tag{25}$$

$$\mathcal{G}(x, \sigma) = \exp\left(-x^2/\sigma^2\right), \tag{26}$$

$$\mathcal{D}(x) = \sum_{j=0}^{6} p_j \times \beta\left(x/A_i - E_j\right), \tag{27}$$

$$\beta(x) = C(Q - x)^2\left(x + m_e c^2\right)\sqrt{x^2 + 2x m_e c^2}, \tag{28}$$

where E_{0-6} are the energies of the LYSO self-luminescence γ-ray peaks, p_{0-6} are the fitting parameters representing the amplitudes of the γ-ray peaks, C is a constant, $Q = 596 \, \text{keV}$ is the Q-value of the ^{176}Lu β-decay, and $m_e c^2$ is the rest energy of the electron.

7.1.2 Performance

Typical waveforms of the DS-RDC are shown in Fig. 46. Due to the high hit rate, several positrons can hit the DS-RDC in one time window; in this example, two pulses are visible in the PSs and four in the LYSO crystals. First, the signal from each PS is analysed to detect hits and to measure their times $t_{\text{e}^+,\text{RDC}}$. The time response of the PSs is fast enough to reconstruct such pile-up hits separately. The time resolution is $\sigma_{t_{\text{e}^+,\text{RDC}}} < 90 \, \text{ps}$ for all bars measured using a ^{90}Sr source in laboratory tests [3]. Then, the signals of the LYSO crystals, whose decay time constant is approximately 50 ns, are analysed for each hit found in the PSs. The integration window is defined by $t_{\text{e}^+,\text{RDC}}$, and the energy for the hit,
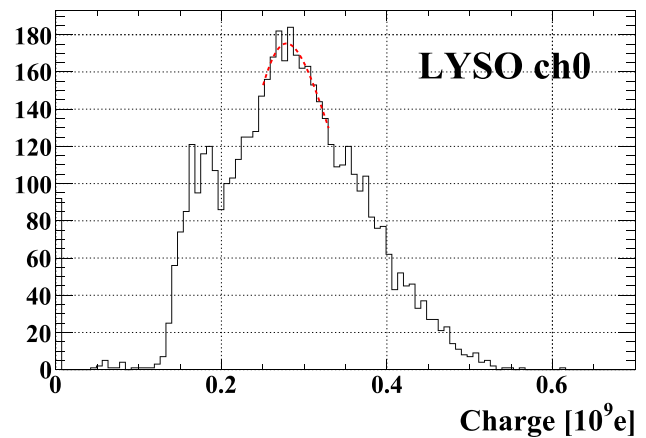

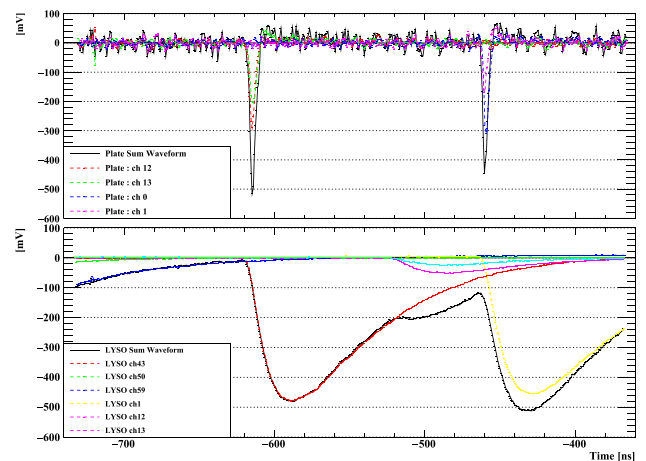**Fig. 45** Charge spectrum for the LYSO self-luminescence and fit result with Eq. (25) (red curve)

Fig. 46 Typical waveforms of the PSs (top) and the LYSO crystals (bottom)

$E_{\text{e}^+,\text{RDC}}$, is reconstructed as the sum of $E_{i,\text{LYSO}}$. The energy resolution was estimated to be $\sigma_{E_{\text{e}^+,\text{RDC}}} = (7.5 \pm 0.3)\%$ at 1 MeV by fitting the spectrum of self-luminescence and the 1.836 MeV peak of a ^{88}Y source. For $\sim 17\%$ of the events at $R_\mu = 3 \times 10^7 \, \text{s}^{-1}$, $E_{\text{e}^+,\text{RDC}}$ is not reconstructed due to pile-up in LYSO. These events are flagged and treated separately in the following analysis.

The RDC is not used as a veto counter but serves as an additional discriminant in the likelihood analysis for the $\mu^+ \rightarrow \text{e}^+\gamma$ search (see Sect. 10). The following two observables are used as discriminating variables between signal and background: the time difference between DS-RDC and the LXe detector, $t_{\text{e}^+,\text{RDC}} - t_{\gamma,\text{LXe}}$, and $E_{\text{e}^+,\text{RDC}}$. If multiple hits are reconstructed in one event, the hit with the smallest $|t_{\text{e}^+,\text{RDC}} - t_{\gamma,\text{LXe}}|$ is selected. Since the distributions for the RMD observables are correlated with the E_γ measured by the LXe detector, the three-dimensional distribution in $(t_{\text{e}^+,\text{RDC}} - t_{\gamma,\text{LXe}}, E_{\text{e}^+,\text{RDC}}, E_\gamma)$ for the signal and the background is evaluated and used in the likelihood function.
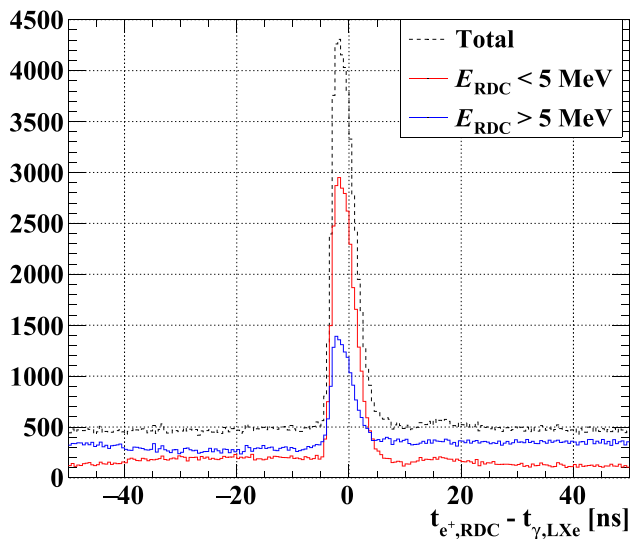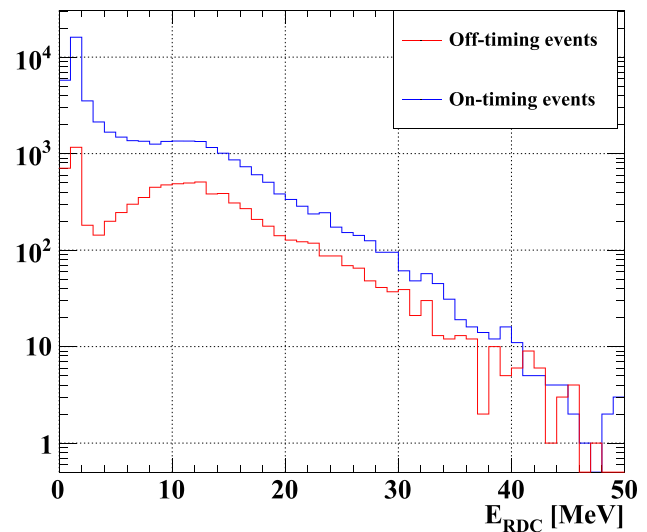
Fig. 47 Distributions of time difference between positrons detected in DS-RDC and γ-rays detected in the LXe detector with $E_\gamma \in [48\,\text{MeV}, 58\,\text{MeV}]$

Fig. 48 Energy spectra in the LYSO crystals for on-timing (red) and off-timing (blue) events

Figure 47 shows the measured distribution for $t_{e^+,\text{RDC}} - t_{\gamma,\text{LXe}}$. The peak around 0 ns is due to RMD events while the flat distribution below it is due to accidental hits. The peak timing value was stable within 14 ps throughout the 2021 physics run.

To show that the peak is indeed due to RMD events and to highlight the effect of energy measurement, the distributions in different $E_{e^+,\text{RDC}}$ regions are also shown. As expected, the number of RMD events is larger for events with $E_{e^+,\text{RDC}} < 5\,\text{MeV}$. While the time distribution of the accidental hits without the $E_{e^+,\text{RDC}}$ cut is flat, we see a left to right asymmetry in the plots with $E_{e^+,\text{RDC}}$ cut. This is because the energy reconstruction is biased by a pile-up hit associated with a γ from RMD; namely hits in the region close to the peak are likely to have a pile-up hit after (before) them, which results in an asymmetric energy bias around the peak region. In the signal events, such an effect is not expected because RDC hits are only accidental. Since pile-up hits with the time difference larger than 40 ns do not bias (or have a negligible impact) the energy reconstruction, such region is used to emulate the RDC response in the signal events. The region with $t_{e^+,\text{RDC}} - t_{\gamma,\text{LXe}} \in [-8\,\text{ns}, 8\,\text{ns}]$ is defined as "on-timing" and $t_{e^+,\text{RDC}} - t_{\gamma,\text{LXe}} \in [-60\,\text{ns}, -50\,\text{ns}]$ as "off-timing" events.

The $E_{e^+,\text{RDC}}$ distributions are shown separately in Fig. 48 for the on-timing and off-timing events.

Since the probability of getting a DS-RDC hit from the $\mu^+ \to e^+\gamma$ decay is very low ($< 0.3\%$), the hits for the signal events are dominated by the accidental hits. Therefore, the distribution for the off-timing events represents the distribution for the $\mu^+ \to e^+\gamma$ signal events, while the distribution

for the accidental background consists of a combination of the on-timing and off-timing distributions.

The fraction of accidental background events tagged by the DS-RDC (tagged RMD fraction) clearly indicates the DS-RDC's performance. It is the product of the fraction of the γ-rays from RMDs to total background γ-rays, the fraction of positrons emitted downstream, the fraction of time with DS-RDC at the measurement position in the physics run, and the detection efficiency of DS-RDS, and is calculated by the ratio of the number of on-timing events, subtracting off-timing events, to the total number of events in the $\mu^+ \to e^+\gamma$ trigger data set.

The result for the 2021 data is shown in Fig. 49 as a function of E_γ; the average fraction is $(14.1 \pm 0.2)\%$, while the expected fraction is 20%. The breakdown of this fraction can be found in Table 4. The discrepancy between the measured and the expected fraction is listed as an unknown contribution. Even though this discrepancy itself does not become a systematic uncertainty in the $\mu^+ \to e^+\gamma$ search since the measured fraction is used, we are trying to understand and improve it for the future analysis. One of the possible causes is that more background γ-rays come from positron annihilation-in-flight events, leading to a reduction in the RMD fraction. The small fraction of the period in the measurement position is due to problems with the interlock system and would be close to 1 in the following years.
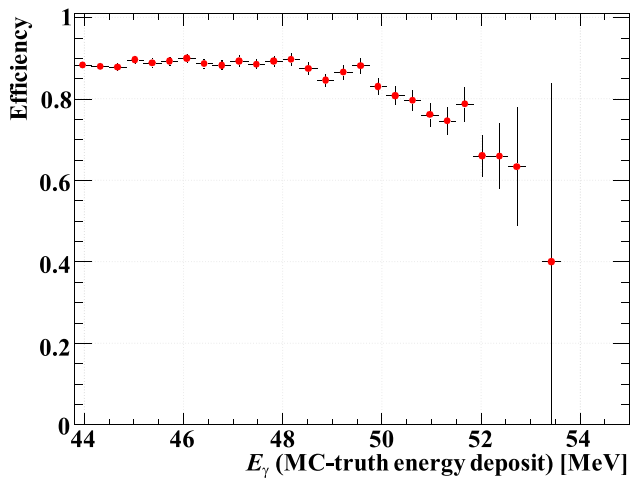
The detection efficiency of DS-RDC versus E_γ derived from MC simulations is shown in Fig. 50. The efficiency decreases at higher E_γ because the higher E_γ is, the lower the energy of the e^+ from the RMD is. At very low energy the e^+s may go undetected because they stop in the gas or in the inactive material of DS-RDC, or their energy deposition is
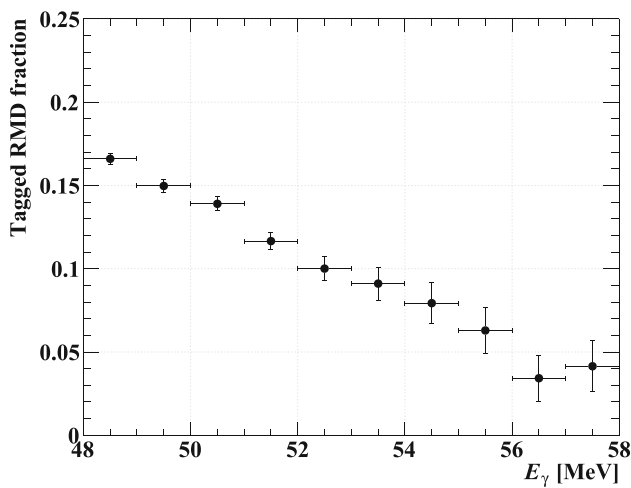
Fig. 49 Tagged RMD fraction as a function of E_γ. See the text for the definition

**Table 4** Breakdown of the efficiencies for the tagged RMD fraction for $E_\gamma > 48$ MeV in 2021

RMD fraction	0.70
Emission to downstream	0.48
Period in measurement position	0.73
Detection efficiency	0.82
Unknown contribution	0.70

Fig. 50 Detection efficiency of DS-RDC as a function of E_γ evaluated with a MC simulation. The efficiency is defined as the ratio of the number of RMD events with a hit in DS-RDC to the number of RMD events in which the positrons are emitted downstream [37]

too low. The plateau below ~ 48 MeV is due to the geometric acceptance (88%).

The decreasing trend of the tagged RMD fraction with E_γ is not only due to the E_γ dependence of the detection efficiency but also to the E_γ dependence of the fraction of γ-rays originating from RMDs. The γ-rays from
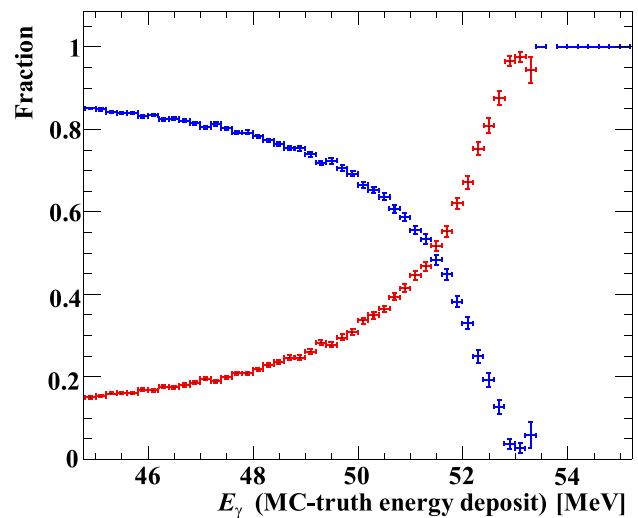
Fig. 51 Fraction of high-energy γ-ray sources from a MC simulation: RMD in blue and positron annihilation-in-flight in red [37]

positron annihilation-in-flight become dominant at higher E_γ as shown in Fig. 51. This energy dependence is also the cause of the correlation between E_γ and the DS-RDC observables.

DS-RDC is estimated to improve sensitivity by $(7 \pm 1)\%$, based on the performance in 2021, under the assumption that the DS-RDC is always at the measurement position during the physics run. This value is significantly lower than the 15% value given in [3]. The main cause is that the correlation with E_γ was not properly considered.

7.2 Upstream RDC

Since the upstream RDC will be installed in the path of the muon beam, it must have a low material budget and a high rate capability, as well as good efficiency and timing resolution. Only the timing can be detected by the US-RDC to meet the requirement of low material budget. For the US-RDC a resistive plate chamber based on diamond-like carbon (DLC) electrodes is under development [38,39]. The DLC deposited on 50 μm thick polyimide foils makes the material budget low enough (0.1% X_0). A prototype of the detector with a size of (2×2) cm^2 was built and tested with the muon beam. The results were promising and met the demanding requirements. Currently, the detector design for a larger detector size is being investigated.

Table 5 Breakdown of detector channels connected to the MEG II WaveDAQ system

Detector	Channel type	# channels	MEG
LXe det. inner face	MPPC	4092	216(PMT)
LXe det.	PMT	668	630
pTC	SiPM	1024	60
CDCH	Differential Frontend	2432	1728
Others	Various	57	≈ 50
Total		8591	2639

8 Trigger and data acquisition

8.1 Concepts and design

The experiment trigger and data acquisition system evolved from the experience obtained while operating the MEG trigger [40] and data acquisition system, which exploited the DRS4 chip [41].

The MEG II detector's granularity requires a number of channels approximately four times larger than in the MEG detector. The breakdown of channels in the MEG II experiment is reported in Table 5. Such an increase in number of channels was possible only by merging the previously separated trigger and data acquisition branches into the WaveDAQ system [42].

WaveDAQ is a highly integrated custom trigger and data acquisition system designed to fulfil the MEG II requirements in terms of detector resolution and background suppression, both at the offline and online stages. The final system consists of 35 crates, each containing up to 16 WaveDREAM modules. The WaveDREAM is a fully contained 16-channel data acquisition platform that employs two DRS4 chips to digitise the analogue signal at sampling speed in the range $0.8-5$ GSPS

To preserve the timing characteristics of the detector signals, the input channels are designed with a programmable gain stage in the range $0.25-100$ with an analogue bandwidth up to 800 MHz capable of providing the bias voltage needed by SiPMs.

When an event of interest is identified, the analogue waveform amplitudes are readout by an external analogue to digital converter and transmitted to a dedicated Data Concentrator Board (DCB) that sends the digitised waveforms over the Ethernet network to the readout computer.

The trigger decision is generated by a group of dedicated FPGA Trigger Concentrator Boards (TCBs) arranged in a tree layer structure, which must generate the decision in ~ 600 ns, because of constraints on DRS4 buffer length when operating at 1.4 GSPS.

8.2 Installation and commissioning

Due to budget constraints, the WaveDREAM system was commissioned using a multi-stage approach [43]. In 2015, we conducted an engineering run in which half of the pTC detector was tested with the PSI muon beam to check the reliability of a WaveDAQ crate. From 2016 to 2020, we increased the number of available DAQ crates from four to nine, including partial readouts for LXe and CDCH, as well as some of the auxiliary channels.

Furthermore, we installed two specialised WaveDAQ crates in our setup. One crate serves as a trigger concentration unit, while the other crate serves as a central hub for distributing critical system control signals, including triggers, clocks, and synchronisation signals.

Throughout each stage of the commissioning process, we carefully checked and developed the following items:

– The electronics noise for all detectors and readout schemes, including single-ended and low front-end amplification $(1-5)$ for LXe, single-ended and high front-end amplification $(50-100)$ for pTC, and differential for CDCH.
– The clock distribution and system synchronisation.
– Basic trigger algorithms for all detectors.
– The Ethernet readout infrastructure and software readout code.

The full system was installed and commissioned in March 2021, ready for the first DAQ campaign, which started in May of the same year. Figure 52 shows a panoramic view of the system.

8.3 Data acquisition design and performance

The DAQ operates in push-mode, meaning that when it receives a trigger signal, all boards prepare the data to be fetched by the DCBs and then delivered to the DAQ server via an Ethernet connection. To maximise data transmission rates, the UDP protocol is adopted over TCP, since it is not connection-based. However, a drawback of UDP is that lost packets are possible, resulting in incomplete event reception and, therefore, DAQ inefficiency.

The typical trigger rate during physics runs ranges from 10 to 30 Hz, depending on trigger thresholds and beam rate. Given that each waveform is approximately ~ 1.5 kB and the number of WDB boards in the system, a 10 Gbit s^{-1} connection between the WaveDAQ and the DAQ server is necessary.

To accommodate the substantial data rate produced by the system, a private network has been installed and managed in terms of Dynamic Host Configuration Protocol (DCHP) and Domain Name System (DNS) servers by the DAQ server, independent of the laboratory network. The 35
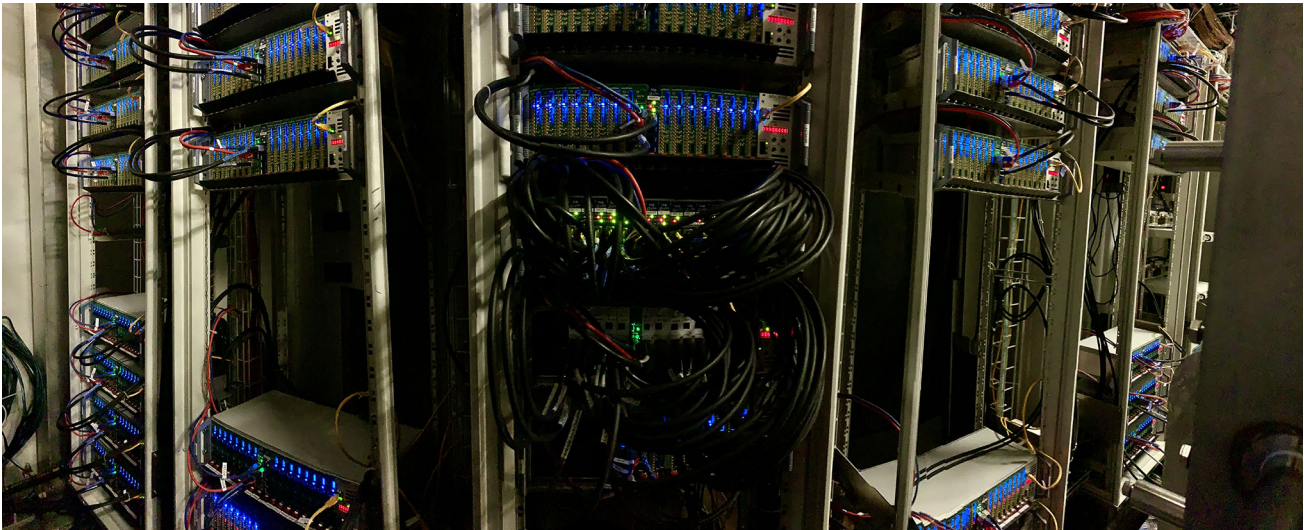
Fig. 52 Panoramic view of the full TDAQ system installed in the PiE5 area. The DAQ crates filled with WaveDREAM boards have the blue LED shining, the trigger and clock distribution crates fully cabled are at the centre of the picture

WaveDAQ crates are distributed among six racks, each of which has a Top-of-Rack switch (MikroTik CRS354-48G-4S+2Q+RM [44]) to gather the data from all the DCBs in the rack and forward them out of the experimental area to the aggregation switch (MikroTik CRS326-24S+2Q+RM). Since the DCB link is at $1\,\mathrm{Gbit\,s^{-1}}$ and the maximum number of DCBs hosted in a rack is eight, we designed the downstream connection using two $10\,\mathrm{Gbit\,s^{-1}}$ lanes to avoid bottlenecks at this stage.

The aggregation switch collects packets from the six Top-of-Rack switches and provides a $10\,\mathrm{Gbit\,s^{-1}}$ connection to the DAQ server, which defines the maximum DAQ rate to be approximately 50 Hz in line with requirements.

The DAQ server and the DAQ software process up to 1×10^6 packets per second, build events, apply DRS chip calibrations, and write events to disk continuously and without loss. A multi-threaded software has been designed with four independent processing steps:

Collector: collects all the packets from the kernel and stores them in a local buffer.

Builder: fetches fragments of events and merges all the packets belonging to the same event and the same board. A built event is then passed to the next buffer.

Worker: applies DRS voltage calibrations to all the waveforms in built events.

Data handler: writes the events to disk after applying data reduction algorithms, described in Sect. 8.3.1.

Each of the steps can be parallelised as needed; in total, we use 32 threads.

8.3.1 Data reduction

A full MEG II event is as large as 16 MB, which is a huge value. The event size can be substantially reduced without deteriorating the experiment's performance by applying data reduction schemes that are tailored to each detector. The methods implemented at the data handler stage are:

1. Waveform re-binning: merge the waveform bins in groups of 2^n ($n = 1,2,3,4,5$).
2. Region of interest (ROI): slice the waveform in a predefined window around the trigger time.
3. Zero suppression: discard waveform without pulses.

For the LXe detector, re-binning is widely used; waveforms are retained at the nominal frequency in a region around the signal edges large enough to preserve their time reconstruction, while other bins are re-binned, with a factor ranging from 8 to 32 dependent on the pulse height. An example of a re-binned waveform is in Fig. 53. Waveforms with very small or no pulses are fully re-binned with a re-bin factor of 8 also in the signal region.

The pTC detector is highly segmented with a very good signal-to-noise separation, large enough to safely apply zero suppression. As a result, the size of pTC events is negligible, since only a small fraction of pTC counters is hit by a positron in each event. ROI cuts are also applied.

The same approach cannot be used for the CDCH because the signal-to-noise separation is not at the same level, so all waveforms are written to disk re-binned by a factor of ten, since this has no impact on reconstructed tracks. A limited ROI cut of 10% of the full range is also applied at the beginning and end of the waveforms.
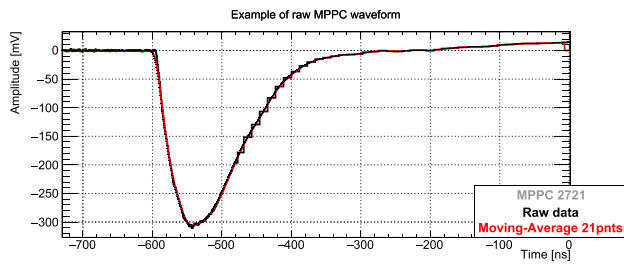
Fig. 53 Example of a re-binned LXe waveform, here the re-bin factor is 16. In red the recovered waveform by smoothing the raw data with a moving average

The overall event size reduction is a factor ≈ 10.

8.3.2 Performance

Performance-wise, the infrastructure that was built and commissioned during the early stages of data collection guarantees an efficiency of over 99% for trigger rates up to 35 Hz, corresponding to a traffic rate on the private network of about $8 \, \mathrm{Gbit \, s^{-1}}$. However, some inefficiency is observed above this threshold.

In the case of detector calibration runs, in which only a subsample of signals are required, we can run the system at the current maximum DCB rate of about 52 Hz. This is crucial to reduce the detector calibration time to the minimum and increase the sample of physics data.

Additional improvements are under study to increase the network rate up to $10 \, \mathrm{Gbit \, s^{-1}}$ and the DCB connection speed, which is not at the design value of $1 \, \mathrm{Gbit \, s^{-1}}$ yet.

8.4 Trigger capabilities

The WaveDAQ system supports up to 64 independent trigger lines, each with its own prescaling factor, to allow the correct mixing of various conditions in the same data set. The trigger lines are identified by a number, which is also used as a priority order if multiple conditions are matched simultaneously. This is relevant when triggers with reduced bias are mixed with the physics trigger for offline studies. The remaining triggers are dedicated to collecting detector-specific calibration data.

8.4.1 $\mu^+ \rightarrow e^+\gamma$ trigger

The $\mu^+ \rightarrow e^+\gamma$ trigger is based on the simultaneous presence of the following three conditions:

γ-ray energy   The weighted sum of all photosensors in the LXe detector is above the threshold.

Time coincidence   The time difference $T_{e^+\gamma}$ between the group of MPPC closest to the γ-ray con-
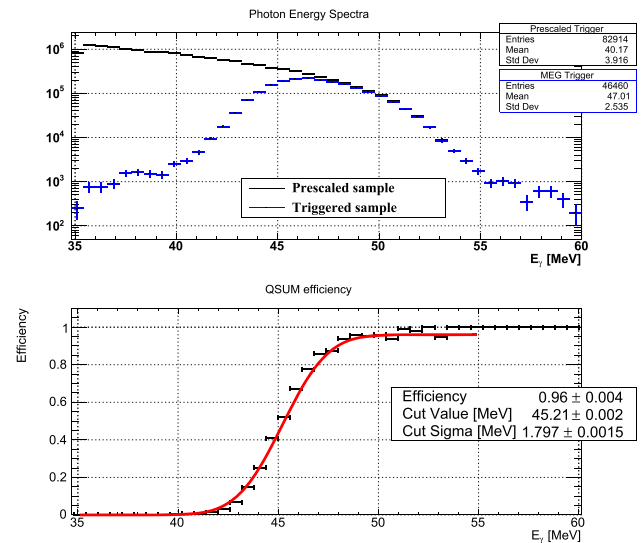
Fig. 54 (Top) Offline-computed γ-ray energy spectra with different thresholds; (bottom) efficiency function obtained from their ratio. The fit yields an online Gaussian resolution of $\sim 4\%$

version and the positron hit on the timing counter is within a programmable time window.

Direction match   The γ-ray conversion point in the LXe detector and the impact position of the positron in the pTC are compatible with a two-body muon decay at rest from the target.

Three dedicated triggers, each with one of the conditions relaxed, are recorded during the physics run with a large enough prescaling not to dominate the throughput.

By comparing the distribution of offline-reconstructed observables, which are expected to have better resolutions than online-computed ones, it is possible to evaluate the effect of the online selection: in Fig. 54, the γ-ray energy spectra are reported. To extract the trigger selection resolution, their ratio is fitted with an integrated Gaussian function, also known as the Gauss error function. The measured resolution is $\sim 4\%$.

The γ-ray energy efficiency, ε_{E_γ}, is estimated by multiplying the integrated Gaussian function of Fig. 54 with the expected response to a 52.83 MeV γ-ray, estimated by scaling the fits of Fig. 41. The current estimate is $\varepsilon_{E_\gamma} = 96\%$, limited by the sub optimal response in terms of uniformity over the inner face of the LXe detector. The online calibration has been improved in the next runs.

Figure 55 shows the time selection window $T_{e^+\gamma}$, which varies depending on the γ-ray conversion depth, denoted as w and defined in Sect. 6.1. It is evident that the trigger selection window exhibits a noticeable dependence on this parameter. The cause of this behaviour was identified as a significant time walk effect in the time measurement performed by the
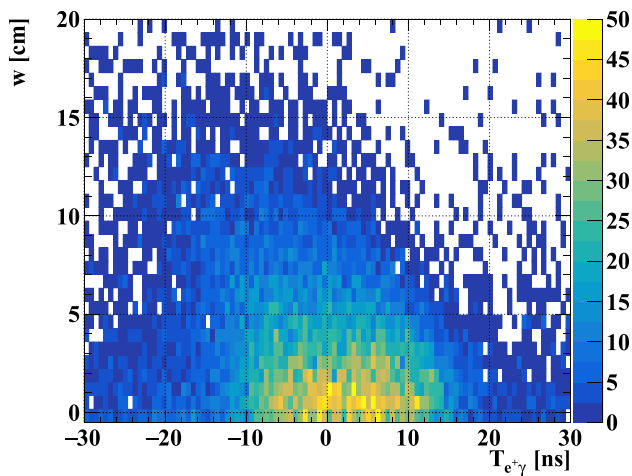
Fig. 55 Time distance distribution for γ-ray–positron pairs $T_{e+\gamma}$ as function of the γ-ray conversion depth w as defined in Sect. 6.1

MPPC detectors. Because these detectors have a rise time of a few nanoseconds, the effect is considerably larger than the expectation based on MC studies. While we achieve full efficiency for shallow events, the efficiency is significantly reduced when the conversion occurs at $w > 10$ cm. We evaluated the efficiency in slices of w and then averaged over its distribution, the resulting value is $\varepsilon_{T_{e+\gamma}} = 94\%$. This was improved from the 2022 run, as described in Sect. 8.4.1.1.

The efficiency of direction match ε_{DM} can only be measured indirectly, using an unbiased set of positron tracks with $p_{e+} > 52$ MeV/c, since there is no physics source for back-to-back events. An artificial set of such events is generated by back-propagating the positron track from the target in the LXe detector; the actual positron hit point in the pTC is then paired with the estimated hit point of the γ-ray. The efficiency is determined by comparing the pTC–LXe hit positions of each event with the table in use in the trigger firmware, which is built on MC simulations, to have $\varepsilon_{DM} = 88.5\%$.

The non-optimal efficiency ε_{DM} obtained on 2021 data is attributed to a small offset in the beam positioning at the COBRA centre and low statistics for double-turn tracks in the MC used to produce the firmware. A new production based on latest results is under study for the incoming runs.

The $\mu^+ \rightarrow e^+\gamma$ trigger efficiency is the product of the efficiencies of the three observables involved:

$$\varepsilon_{TRG} = \varepsilon_{E_\gamma} \times \varepsilon_{T_{e+\gamma}} \times \varepsilon_{DM} \approx (80 \pm 1)\%. \tag{29}$$

This number was measured at $R_\mu = 3 \times 10^7$ s^{-1}, at higher rates the trigger efficiency is degraded by 2% at most due to tighter trigger thresholds, in particular the $T_{e+\gamma}$ cut.

Improvements since 2022 The γ-ray conversion time algorithm was improved during the 2022 run. Instead of using the group of MPPCs closest to the γ-ray conversion point, the

signal from the first PMT in the LXe detector's back face is used. This modification was made because PMTs have a faster response time compared to MPPCs. As a result, we achieved a more precise measurement of $T_{e+\gamma}$, leading, as expected, to an improvement in $\varepsilon_{T_{e+\gamma}}$.

Similarly an improved LXe detector calibration at trigger level returns a more uniform response over the entrance face; therefore ε_{E_γ} is expected to improve.

With the finalisation of the positron reconstruction algorithm and the availability of a large sample of reconstructed positron tracks, we aim to investigate how to extend the direction match table to increase ε_{DM}.

8.4.2 Calibration and other triggers

In experiments such as MEG II, where a tiny signal needs to be detected in a harsh background, a complete and complementary set of calibration methods is deployed, most of which are accompanied by dedicated trigger logic. The auxiliary crate, a dedicated WaveDAQ unit, collects all the signals from the calibration devices.

Among the various calibrations, the LXe detector calibration is the most challenging. A detailed description is available in Sects. 6.3 and 6.6.4. About 10 trigger lines are dedicated to this task. The energy scale calibration relies on the collection of γ-rays of known energies in the detector in the range 9 to 130 MeV. A γ-ray is triggered by a threshold on the estimated energy deposit, which, in some cases, is in coincidence with an auxiliary device: the neutron generator for the 9 MeV events and the BGO calorimeter for the CEX campaign.

Figure 56 shows the energy spectrum of the 55 and 83 MeV lines as reconstructed by the trigger logic. The line fit returns the online energy resolution at the signal energy. The sensor gains of the LXe detector are calibrated using a set of LEDs flashing at well-known intensities. The LED drivers are connected to the WaveDAQ system and provide TTL signals in time with the LED light emission.

The QEs of the PMTs and the PDEs of the MPPCs are measured by comparing the light measured from the decay of α-particles submerged in the LXe detector with MC simulations. These events are selected using a pulse shape discrimination logic, already used in the MEG experiment and described in [45]. A revised version of the trigger logic is implemented in the MEG II experiment using the signals gathered from all the outer face PMTs.

The pTC is calibrated daily using the laser-based system to monitor the counter time offsets. A dedicated trigger line is used, and the laser pulse generator provides a signal synchronous with the laser pulse, which is connected to a dedicated WaveDAQ input channel and used as a trigger. The calibration results are shown in Fig. 27.
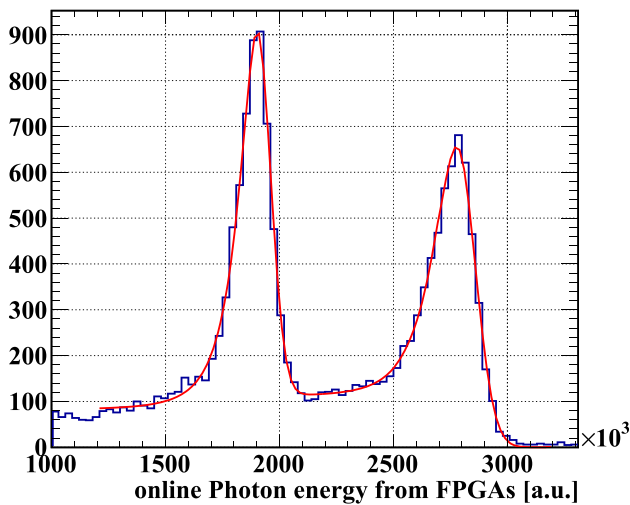
Fig. 56 CEX online γ-ray spectrum as reconstructed by online trigger processing. The two peaks at 55 and 83 MeV are clearly visible, the CEX configuration is described in Sect. 6.2. Being monochromatic lines, the online resolution here can be measured without relying on offline processing. The function used in the fit is the sum of two response functions as in Eq. (23) for the two energy lines plus a flat background. The online resolution at 55 MeV is 3.1%

9 Computing

Significant offline computing resources are required to store the data on disk, process them, produce MC simulation samples, and provide the analysis platform to individual users. The MEG II offline computing system is based on an on-premise high-performance computing (HPC) cluster, operated by the Science IT Infrastructure and Services Department of PSI. It consists of login nodes, computing nodes with 320 CPU cores for batch jobs, and storage servers with a capacity of 2 PB. Two types of storage architectures are used: one based on IBM Spectrum Scale (known as GPFS) with a capacity of 1.1 PB, used as main storage for intensive I/O activities; the other based on the standard NAS system. All nodes and storage are connected via the InfiniBand (EDR 100 Gbit s^{-1}) network to ensure high throughput and low latency. The batch jobs are managed by Slurm [46]. The availability of the system was 98% (or 99.8% during the DAQ period) in 2022. Additional $\sim$ 500 CPU cores are available for offline processing using a general-purpose HPC cluster at PSI.

The data rate during 2022 was 180 MB s^{-1} at $R_\mu = 5 \times 10^7$ s^{-1}. The raw data in the MIDAS file format [47] are transferred from the DAQ machine to the offline cluster over a 10 Gbit s^{-1} local area network and then compressed with the bzip2 algorithm to reduce the size by a factor of 3. The compressed raw data are stored on the disk for offline analysis and, in parallel, sent to a tape-based archive system at Swiss National Supercomputing Centre (CSCS) in Lugano over a dedicated 100 Gbit s^{-1} network between PSI

and CSCS. The raw data, as well as the processed data sets used for publications of physics results, will be preserved and published there.

The total raw data in 2022 amounts to 420 TB. After the first reconstruction phase, followed by a pre-selection of events, the raw data are deleted from the disk.

The MEG II software suite consists of several programs for simulation and analysis: a MC program for event generation, particle tracking and detector simulation; a program for simulation of event mixing and readout electronics, a program for reconstruction and a program for statistical analysis. The overall structure is similar to that of the MEG experiment [48], while the MC program was renewed with Geant4 [49,50]. All the programs are based on ROME [51], a framework generator, and are written in C++17. The file format in ROOT [52] is used throughout for I/O, while the reconstruction program can also read the (compressed) MIDAS files.

The framework relies heavily on packages that are widely used in the high-energy physics community, such as Geant4, ROOT and GENFIT, while it can also easily integrate external C++ packages. In order to implement deep-learning-based algorithms, the reconstruction program supports the application of models in the ONNX format [53] by means of ONNX Runtime C++ API [54]. Therefore, users can build and train models in their preferred machine-learning framework and environment while maintaining the single common interface in the reconstruction program. On the other hand, this framework limits the processors available in the inference stage to CPUs.

The analysis environment is also provided as a container for Docker [55] and Apptainer [56] so that the analysis can be performed seamlessly in other systems, e.g. in a local cluster in other institutes or even on a personal laptop.

The average time to simulate a signal event is 37 s using a single processor core, with 80% of the time spent in tracking scintillation photons in LXe. The average time to reconstruct an event at $R_\mu = 5 \times 10^7$ s^{-1} is 50 s with the current reconstruction algorithms; the largest contribution (64%) comes from track-finding in CDCH at high occupancy. All the physics data in 2022 can be processed in $\sim$ 60 days with 500 cores in parallel.

10 Sensitivity

A confidence interval for the branching ratio $\mathcal{B}$ of the $\mu^+ \to e^+\gamma$ decay is extracted with a likelihood analysis over six or seven variables that have discriminating power for the signal versus the background: the positron energy E_{e^+} and the γ-ray energy E_γ (both of which have a peak value at $\sim$ 52.83 MeV for signal events); the relative angle $\Theta_{e^+\gamma}$ or two independent projections thereof, $\theta_{e^+\gamma}$ and $\phi_{e^+\gamma}$, as defined
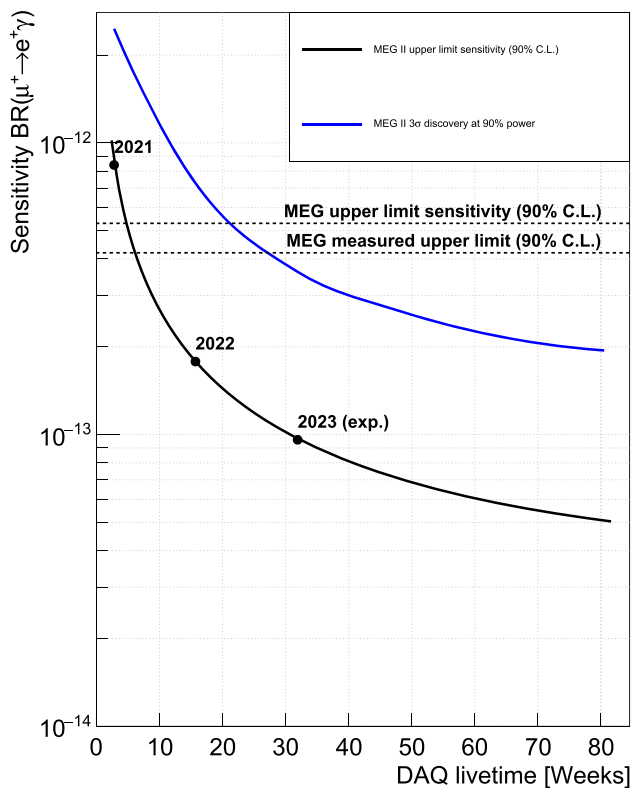
Fig. 57 Expected MEG II upper limit sensitivity (90% CL) (black curve) and 3σ discovery potential (blue curve) versus DAQ time, compared with MEG upper limit sensitivity (90% CL) and measured upper limit (90% CL) [2]. The points mark the sensitivity for the past years and the estimation for the current one. See text for details

in [2]; the relative time $t_{e^+\gamma}$ (which is expected to have a peak value at zero); two quantities that exploit the RDC: the RDC energy deposit E_{e^+}, RDC and the relative time $t_{e^+,RDC} - t_{\gamma,LXe}$ (whose distributions are different for events caused by RMDs and accidental RDC–LXe coincidences that can also occur for signal events). The interval (or upper limit if the lower limit includes zero) for $\mathcal{B}(\mu^+ \to e^+\gamma)$ with a confidence level (CL) of 90% is extracted using a frequentist approach that also takes systematic uncertainties into account as described in [2].

The probability density functions (PDFs) for the accidental background used to construct the likelihood function are extracted from the side-bands of an analysis region defined by $E_\gamma \in [48\,\mathrm{MeV}, 58\,\mathrm{MeV}]$ and $t_{e^+\gamma} \in [-500\,\mathrm{ps}, 500\,\mathrm{ps}]$. The PDFs for the signal and RMD are obtained by convolving the expected distributions with resolution functions extracted from the data, with minor MC-based corrections.

Two different analysis strategies are adopted. In one, resolution functions of some of the variables that change from event to event are assigned on the event-by-event basis (e.g. based on the uncertainties in the positron kinematic variables that can be estimated from the track fit, or the reconstructed position of the γ-ray conversion point in the LXe detector).

In the other, the events are divided into several categories, depending on the quality of the reconstruction, and different PDF sets are extracted for each category. The first approach allows maximising statistical sensitivity, while the second approach is less prone to systematic uncertainties.

The sensitivity of the experiment reflects the resolution functions and the efficiencies. Table 6 summarises the main results discussed in the previous sections, compared to the predictions from [3,57]. Average values are given here, although event-by-event PDFs are used in the likelihood analysis. If the resolution function is described by a sum of Gaussian PDFs, the width of the principal component (*core resolution*) is given. For positron observables, the typical core fraction is 90%. For E_γ, the main deviation from Gaussianity is the long tail at low energy. The positron resolutions are evaluated at $R_\mu = 4 \times 10^7\,\mathrm{s}^{-1}$, while a $5-7\%$ deterioration is observed from $R_\mu = 3 \times 10^7\,\mathrm{s}^{-1}$ to $5 \times 10^7\,\mathrm{s}^{-1}$.

The signal PDFs take into account the correlations of ϕ_{e^+} with E_{e^+} and θ_{e^+}, which translate into correlations of $\phi_{e^+\gamma}$ with E_{e^+} and $\theta_{e^+\gamma}$. Since the true values of E_{e^+} and $\theta_{e^+\gamma}$ for the signal events are known, it is possible to correct $\phi_{e^+\gamma}$ event-by-event (or, in other words, to account for the correlation event-by-event in the PDFs as in [2]). For this reason, the effective statistical error on ϕ_{e^+} that determines the $\phi_{e^+\gamma}$ resolution is lower than the global ϕ_{e^+} resolution. In the table we quote this effective statistical error and since it also depends on ϕ_{e^+} itself, we quote the value at $\phi_{e^+} = 0$ to allow consistent comparison with the numbers quoted in previous papers, where the same convention was used.

The $t_{e^+\gamma}$ resolution was evaluated from the peak in the $t_{e^+\gamma}$ distribution due to the coincident RMD events, with taking into account the E_γ- and E_{e^+}-dependence of the time resolutions. The result is consistent with the combination of the resolutions measured for γ-ray and e^+ individually.

Simulated pseudo-experiments are used to evaluate the sensitivity of the experiment $\mathcal{S}_{90}$, defined as the median value of the distribution of the 90% CL upper limits resulting from the likelihood analysis for a null signal hypothesis. Simulated pseudo-experiments are also used to evaluate the 3σ discovery at 90% power. Figure 57 shows the projected sensitivity and the projected discovery limit versus the DAQ lifetime assuming that the resolutions in Table 6 remain stable in the coming years and that the analysis remains the same as today. Systematic uncertainties, which are expected to give a minor contribution, are not included.

The prediction reflects the current status and knowledge of the detector, and the quality of the current data analysis. The evolution of the detector behaviour, the continuous improvement of the reconstruction algorithms and the increasingly better understanding of the systematic uncertainties will determine the final sensitivity of the experiment. Nevertheless, we are confident that the design sensitivity of $\mathcal{S}_{90} = 6 \times 10^{-14}$ will be achieved by the end of 2026.

Table 6 Resolutions (Gaussian σ) and efficiencies measured at $R_\mu = 4 \times 10^7 \,\mathrm{s}^{-1}$, compared with the predictions from [3,57]

Resolutions	Foreseen	Achieved
E_{e^+} (keV)	100	89
ϕ_{e^+} [a], θ_{e^+} (mrad)	3.7/6.7	4.1/7.2
y_{e^+}, z_{e^+} (mm)	0.7/1.6	0.74/2.0
E_γ(%) $(w < 2\,\mathrm{cm})/(w > 2\,\mathrm{cm})$	1.7/1.7	2.0/1.8
u_γ, v_γ, w_γ (mm)	2.4/2.4/5.0	2.5/2.5/5.0
$t_{\mathrm{e}^+\gamma}$ (ps)	70	78
Efficiency (%)		
ε_γ	69	62
$\varepsilon_{\mathrm{e}^+}$	65	67
$\varepsilon_{\mathrm{TRG}}$	≈ 99	80

[a] At $\phi_{\mathrm{e}^+} = 0$ with correlation taken into account. See text for the details

11 Conclusions

We have presented a detailed overview of the operation of all components of the MEG II detector during the engineering runs in the years 2016–2020 and in the physics run in the years 2021–2022. We found several problems, to name a few: CDCH breakages, faster than expected decrease of MPPC PDEs for LXe and mild degradation of time resolution of pTC, both due to radiation damage. After having accumulated some delay in the schedule, those problems were solved or tackled so as to minimise their effects on the sensitivity. Additional planned steps should further reduce these effects.

Since 2021 the MEG II experiment has regularly operated with performances close to its design values. On this basis, we estimated the sensitivity to the $\mu^+ \to \mathrm{e}^+\gamma$ decay versus the DAQ lifetime and calendar year. The sensitivity obtained with the 2021–2022 data will be significantly better than the existing MEG limit.

Data Availability Statement This manuscript has associated data in a data repository. [Authors' comment: Additional raw data used in this manuscript are available under request.]

References

1. J. Adam et al., The MEG detector for $\mu^+ \to \mathrm{e}^+\gamma$ decay search. Eur. Phys. J. C **73**(4), 2365 (2013). https://doi.org/10.1140/epjc/s10052-013-2365-2. arXiv:1303.2348
2. A.M. Baldini et al. (MEG Collaboration), Search for the lepton flavour violating decay $\mu^+ \to \mathrm{e}^+\gamma$ with the full dataset of the MEG experiment. Eur. Phys. J. C **76**(8), 434 (2016). https://doi.org/10.1140/epjc/s10052-016-4271-x
3. A.M. Baldini et al. (MEG II Collaboration), The design of the MEG II experiment. Eur. Phys. J. C **78**(5) (2018). https://doi.org/10.1140/epjc/s10052-018-5845-6
4. W. Joho, The S.I.N ring cyclotron after one year of operation. IEEE Trans. Nucl. Sci. **22**(3), 1397–1401 (1975). https://doi.org/10.1109/TNS.1975.4327894
5. J. Grillenberger, C. Baumgarten, M. Seidel, The high intensity proton accelerator facility. SciPost Phys. Proc. **5**, 002 (2021). https://doi.org/10.21468/SciPostPhysProc.5.002
6. K. Arndt et al., Technical design of the phase I Mu3e experiment. Nucl. Instrum. Methods A **1014**, 165679 (2021). https://doi.org/10.1016/j.nima.2021.165679. arXiv:2009.11690
7. M. Ahmed et al. (MEGA Collaboration), Search for the lepton-family-number nonconserving decay $\mu^+ \to \mathrm{e}^+\gamma$. Phys. Rev. D **65**, 112002 (2002). https://doi.org/10.1103/PhysRevD.65.112002
8. F. Berg, CMBL—a high-intensity muon beam line & scintillation target with monitoring system for next-generation charged lepton flavour violation experiments. PhD thesis, ETH Zurich (2017). https://www.research-collection.ethz.ch/handle/20.500.11850/213470
9. G. Cavoto et al., A photogrammetric method for target monitoring inside the MEG II detector. Rev. Sci. Instrum. **92**(4), 043707 (2021). https://doi.org/10.1063/5.0034842. arXiv:2010.11576
10. D. Palo et al., Precise photographic monitoring of MEG II thin-film muon stopping target position and shape. Nucl. Instrum. Methods A **944**, 162511 (2019). https://doi.org/10.1016/j.nima.2019.162511. arXiv:1905.10995

11. M. Chiappini et al., The cylindrical drift chamber of the MEG II experiment. Nucl. Instrum. Methods A **1047**, 167740 (2023). https://doi.org/10.1016/j.nima.2022.167740

12. A.M. Baldini et al., Gas distribution and monitoring for the drift chamber of the MEG II experiment. J. Instrum. **13**(06), P06018 (2018). https://doi.org/10.1088/1748-0221/13/06/P06018. arXiv:1804.08482

13. H. Schindler, Garfield++ user guide (Version 2023.1). https://garfieldpp.web.cern.ch/documentation/. Accessed 2023

14. A. Baldini et al., Detailed analysis of chemical corrosion of ultra-thin wires used in drift chamber detectors. J. Instrum. **16**, T12003 (2021). https://doi.org/10.1088/1748-0221/16/12/T12003

15. A.M. Baldini et al., Performances of a new generation tracking detector: the MEG II cylindrical drift chamber. Eur. Phys. J. C (2023, to be submitted)

16. R. Frühwirth, A. Strandlie, Track fitting with ambiguities and noise: a study of elastic tracking and nonlinear filters. Comput. Phys. Commun. **120**(2), 197–214 (1999). https://doi.org/10.1016/S0010-4655(99)00231-3

17. C. Höppner et al., A novel generic framework for track fitting in complex detector systems. Nucl. Instrum. Methods A **620**(2), 518–525 (2010). https://doi.org/10.1016/j.nima.2010.03.136

18. J. Rauch, T. Schlüter, GENFIT—a generic track-fitting toolkit. J. Phys. Conf. Ser. **608**, 012042 (2015). https://doi.org/10.1088/1742-6596/608/1/012042. See also https://github.com/GenFit/GenFit

19. D. Palo, W. Molzon, Neural network applications to improve drift chamber track position measurements. Nucl. Instrum. Methods A (2023, to be submitted)

20. R. Frühwirth, A. Strandlie, *Pattern Recognition, Tracking and Vertex Reconstruction in Particle Detectors*. Verlag der Österreichischen Akademie der Wissenschaften (2021)

21. D. Primor et al., A novel approach to track finding in a drift tube chamber. J. Instrum. **2**(01), P01009 (2007). https://doi.org/10.1088/1748-0221/2/01/P01009

22. A. Baldini et al., The measuring systems of the wire tension for the MEG II drift chamber by means of the resonant frequency technique. Nucl. Instrum. Methods A **1045**, 167524 (2023). https://doi.org/10.1016/j.nima.2022.167534

23. G. Chiarello et al., An automatic system for the wiring of drift chambers for modern high intensity and high precision particle physics experiments. J. Instrum. **15**, C07034 (2020). https://doi.org/10.1088/1748-0221/15/07/C07034

24. Luxium Solutions, Fast timing plastic scintillators BC418 BC420 BC422 BC422q. www.crystals.saint-gobain.com/radiation-detection-scintillators/plastic-scintillators/fast-timing-bc-418-bc-420-bc-422-bc-422q. Accessed 2023

25. M. Nishimura et al., Full system of positron timing counter in MEG II having time resolution below 40 ps with fast plastic scintillator readout by SiPMs. Nucl. Instrum. Methods A **958**, 162785 (2020). https://doi.org/10.1016/j.nima.2019.162785

26. P.W. Cattaneo et al., Development of high precision timing counter based on plastic scintillator with SiPM readout. IEEE Trans. Nucl. Sci. **61**(5), 2657–2666 (2014). https://doi.org/10.1109/TNS.2014.2347576. arXiv:1402.1404

27. G. Boca et al., Timing resolution of a plastic scintillator counter read out by radiation damaged SiPMs connected in series. Nucl. Instrum. Methods A **999**, 165173 (2021). https://doi.org/10.1016/j.nima.2021.165173. arXiv:2005.05027

28. G. Boca et al., The laser-based time calibration system for the MEG II pixelated Timing Counter. Nucl. Instrum. Methods A **947**, 162672 (2019). https://doi.org/10.1016/j.nima.2019.162672

29. V. Blobel, Software alignment for tracking detectors. Nucl. Instrum. Methods A **566**, 5–14 (2006). https://doi.org/10.1016/j.nima.2006.05.157. See also https://www.terascale.de/wiki/millepede_ii/

30. M. De Gerone et al., Development and commissioning of the timing counter for the MEG experiment. IEEE Trans. Nucl. Sci. **59**, 379–388 (2012). https://doi.org/10.1109/TNS.2012.2187311. arXiv:1112.0110

31. K. Ieki et al., Large-area MPPC with enhanced VUV sensitivity for liquid xenon scintillation detector. Nucl. Instrum. Methods A **925**, 148–155 (2019). https://doi.org/10.1016/j.nima.2019.02.010

32. K. Ieki et al., Study on degradation of VUV-sensitivity of MPPC for liquid xenon scintillation detector by radiation damage in MEG II experiment. Nucl. Instrum. Methods A **1053**, 168365 (2023). https://doi.org/10.1016/j.nima.2023.168365

33. S. Kobayashi, Full commissioning of liquid xenon scintillation detector to search for $\mu^+ \rightarrow e^+\gamma$ with the highest sensitivity in MEG II experiment. PhD thesis, University of Tokyo (2022). https://www.icepp.s.u-tokyo.ac.jp/download/doctor/phD2022_kobayashi.pdf

34. T. Libeiro et al., Novel X-ray scanning technique for in-situ alignment of photo-detectors in the MEG II calorimeter. Nucl. Instrum. Methods A **1048**, 167901 (2023). https://doi.org/10.1016/j.nima.2022.167901

35. J. Adam et al. (MEG Collaboration), Calibration and monitoring of the MEG experiment by a proton beam from a Cockcroft-Walton accelerator. Nucl. Instrum. Methods A **641**, 19–32 (2011). https://doi.org/10.1016/j.nima.2011.03.048

36. D. Zahnow et al., The $S(E)$ factor of ^{7}Li$(p, \gamma)^8$Be and consequences for $S(E)$ extrapolation in ^{7}Li$(p, \gamma_0)^8$Be. Z. Phys. A Hadrons Nucl. **351**, 229–236 (1995). https://doi.org/10.1007/BF01289534

37. R. Onda, Suppression of γ-ray backgrounds for the highest sensitivity of $\mu \rightarrow e\gamma$ search in MEG II experiment. PhD thesis, University of Tokyo (2021). https://www.icepp.s.u-tokyo.ac.jp/download/doctor/phD2021_onda.pdf

38. A. Oya et al., Development of high-rate capable and ultra-low mass resistive plate chamber with diamond-like carbon. J. Phys. Conf. Ser. (2022). https://doi.org/10.1088/1742-6596/2374/1/012143

39. K. Yamamoto et al., Development of ultra-low mass and high-rate capable RPC based on diamond-like carbon electrodes for MEG II experiment. Nucl. Instrum. Methods A **1054**, 168450 (2023). https://doi.org/10.1016/j.nima.2023.168450

40. L. Galli et al., An FPGA-based trigger system for the search of $\mu^+ \rightarrow e^+\gamma$ decay in the MEG experiment. J. Instrum. **8**, P01008 (2013). https://doi.org/10.1088/1748-0221/8/01/P01008

41. S. Ritt, The DRS chip: cheap waveform digitizing in the GHz range. Nucl. Instrum. Methods A **518**, 470–471 (2004). https://doi.org/10.1016/j.nima.2003.11.059

42. M. Francesconi et al., The WaveDAQ integrated trigger and data acquisition system for the MEG II experiment. Nucl. Instrum. Methods A **1045**, 167542 (2023). https://doi.org/10.1016/j.nima.2022.167542

43. M. Chiappini et al., Towards a new $\mu \rightarrow e\gamma$ search with the MEG II experiment: from design to commissioning. Universe (2021). https://doi.org/10.3390/universe7120466

44. MikroTik webpage. https://mikrotik.com/. Accessed 2023

45. D. Nicolò et al., Real-time particle identification in liquid xenon. IEEE Trans. Nucl. Sci. **68**(11), 2630–2636 (2021). https://doi.org/10.1109/TNS.2021.3099296

46. Slurm Workload Manager. https://slurm.schedmd.com/. Accessed 2023

47. MIDAS: The Maximum Integrated Data Acquisition System. https://daq00.triumf.ca/MidasWiki/. Accessed 2023

48. P.W. Cattaneo et al., The architecture of MEG simulation and analysis software. Eur. Phys. J. Plus **126**(7), 1–12 (2011). https://doi.org/10.1140/epjp/i2011-11060-6

49. S. Agostinelli et al. (Geant4 Collaboration), Geant4-a simulation toolkit. Nucl. Instrum. Methods A **506**, 250–303 (2003). https://doi.org/10.1016/S0168-9002(03)01368-8

50. J. Allison et al., Recent developments in Geant4. Nucl. Instrum. Methods A **835**, 186–225 (2016). https://doi.org/10.1016/j.nima.2016.06.125. See also https://geant4.web.cern.ch/, Release 10.06.p03

51. M. Schneebeli, R. Sawada, S. Ritt, ROME—a universally applicable analysis framework generator, in *Proceedings of the International Conference on Computing in High Energy and Nuclear Physics (CHEP06), Mumbai, India* (2006). See also https://bitbucket.org/muegamma/rome3

52. R. Brun, F. Rademakers, ROOT—an object oriented data analysis framework. Nucl. Instrum. Methods A **389**, 81–86 (1997). https://doi.org/10.1016/S0168-9002(97)00048-X. See also https://root.cern.ch/, Release v6.28.00

53. ONNX: Open Neural Network Exchange. https://onnx.ai/. Accessed 2023

54. ONNX Runtime. https://onnxruntime.ai/. Accessed 2023

55. D. Merkel, Docker: lightweight linux containers for consistent development and deployment. Linux J. **2014**(239), 2 (2014). See also https://www.docker.com/

56. G.M. Kurtzer, V. Sochat, M.W. Bauer, Singularity: scientific containers for mobility of compute. PLoS ONE **12**(5), e0177459 (2017). https://doi.org/10.1371/journal.pone.0177459. See also https://apptainer.org/

57. A.M. Baldini et al. (MEG II Collaboration), The search for $\mu^+ \to e^+\gamma$ with 10^{-14} sensitivity: the upgrade of the MEG experiment. Symmetry **13**(9), 1591 (2021). https://doi.org/10.3390/sym13091591. arXiv:2107.10767